

Copyright

by

Lijia Liu

2021

The Dissertation Committee for Lijia Liu
certifies that this is the approved version of the following dissertation:

Analysis of complex movements

Committee:

Dana H. Ballard, Supervisor

Peter Stone

Scott Niekum

Etienne Vouga

Mary Hayhoe

Analysis of complex movements

by

Lijia Liu

Dissertation

Presented to the Faculty of the Graduate School of

The University of Texas at Austin

in Partial Fulfillment

of the Requirements

for the Degree of

Doctor of Philosophy

The University of Texas at Austin

May 2021

Acknowledgments

A million thanks to my supervisor, Prof. Dana Ballard, for all the patient guidance, encouragement, and advice throughout my study as his student. Thanks to my committee members, Prof. Peter Stone, Prof. Scott Niekum, Prof. Etienne Vouga, and Prof. Mary Hayhoe, for all the precious suggestions and help. Thanks to our lab (Vision, Cognition, and Action VR lab) members for all the constructive thoughts. Finally, I will thank my parents for their generous support.

This research was supported by National Science Foundation grant.

LIJIA LIU

The University of Texas at Austin

May 2021

Analysis of complex movements

Publication No. _____

Lijia Liu, Ph.D.

The University of Texas at Austin, 2021

Supervisor: Dana H. Ballard

In most everyday repetitive movements such as walking, sitting, and reaching, humans exhibit large degrees of regularity. However, at the other end of the movement spectrum, in complex movement tasks, such as retrieving an object from a cluttered environment or choosing balance positions for transporting a large, unwieldy object, humans are inventive problem solvers. Therefore, in the quest to understand the human movement system, it would be essential to know if general movements have regularities across subjects as it would provide an essential scaffold in the development of more detailed dynamic movement models.

This research mainly aims to learn the principles behind large-scale arbitrary movements, particularly regarding variations between different subjects. For example, given a goal-directed task, do the movements appear similar across subjects, or are movements very individualized? The tasks for the research covers developing an interactive virtual reality environment to capture goal-directed whole-body human movements, getting insights into the regularities underlying those motion capture data (kinematics), and finally analyzing the corresponding energy cost by using a forty-eight degree of freedom dynamic human model (dynamics). The results illustrate that humans chose trajectories that are economical in energetic cost while accomplishing goal-directed tasks.

Contents

Acknowledgments	iv
Abstract	v
List of Tables	xi
List of Figures	xii
Chapter 1 Introduction	1
1.1 Motivation	2
1.2 Overview	3
1.3 Principal Contributions	7
1.4 Organization	8
Chapter 2 Background	10
2.1 Neural Control of Movement	10
2.2 Computational Modeling	14
2.3 Movement Analysis Techniques	16
2.4 Motivation for our research setting	19

Chapter 3	Virtual Tracing Experiment	23
3.1	Methods	24
3.1.1	Tracing protocol	25
3.1.2	Subjects	29
3.1.3	Motion capture	29
3.1.4	Data analysis overview	31
3.1.5	Starting posture classification	32
3.1.6	Tracing standard deviation calculation	33
3.1.7	Tracing Posture matching	36
3.2	Results	38
3.2.1	Initial posture choices	39
3.2.2	Posture matching during tracing	40
3.2.3	Marker variations during tracing	47
3.3	Discussion	51
3.4	Limitations of the Study	58
Chapter 4	Computational Modeling: Human Dynamic Model	59
4.1	Method	60
4.1.1	Human Model	63
4.1.2	Data Fitting	64
4.1.3	Pose Fitting	66
4.1.4	Inverse Dynamics	69
4.1.5	Method summary	71
4.2	Results	73
4.2.1	Test 1: Model Performance	73
4.2.2	Test 2: Model Validation	79

4.3	Discussion	86
Chapter 5	Human Dynamic Model System	90
5.1	System Configuration	90
5.1.1	Default Motion Settings	91
5.1.2	Custom Motion Settings	95
5.2	User Interface	96
5.2.1	Display panel	96
5.2.2	Control panel	96
5.2.3	Functional panel	102
5.3	Summary	107
Chapter 6	Energy Cost in Virtual Tracing Tasks	112
6.1	Methods	113
6.1.1	Virtual tracing experiment	113
6.1.2	Human dynamic model	115
6.1.3	Energy cost computation	117
6.2	Results	118
6.2.1	Detailed Energetic cost analysis of tracing path 1	119
6.2.2	Energy cost analysis of tracing individual paths	122
6.3	Discussion	127
Chapter 7	Muscle Co-contraction Detection	130
7.1	Muscle Co-contraction	131
7.2	Gaussian Process	132
7.3	Experiment	135
7.3.1	Overview	135

7.3.2	Data set	136
7.3.3	Results	136
Chapter 8	Future Work	146
8.1	Locomotion in Natural Terrains	147
8.1.1	Background	147
8.1.2	Experiment	148
8.2	Simple Single-Behavior Motion Synthesis	156
8.2.1	Background	156
8.2.2	Experiment	157
8.3	Human movements animation	166
8.4	Improvement of the dynamic model	170
8.5	Dynamics analysis of human movements	172
Bibliography		173

List of Tables

3.1	The proportion of individual subjects in each cluster as a percentage. For example, for tracing path 5, the square curve, 66 % of the subjects chose to face the curve from one side and 34 % from the other. Related to Figure 3.4.	40
3.2	The average standard deviation of the marker positions. Related to Figure 3.9	50
3.3	All the R values for the four markers computed for all nine curves show positive correlations. Related to Figure 3.10 . . .	51

List of Figures

1.1	The overall organization of the research.	3
3.1	the virtual environment setup. (a) shows a full view of a path, denoted by a black curve, and the starting position, denoted by a large white sphere. The small white sphere on the curve at the end of a red segment is the tracing target sphere. (b) depicts the scene when a trial is finished. The green curve is the actual tracing trajectory generated by a subject. (c) illustrates a subject in the act of tracing a curve in the laboratory's motion capture 2 x 2 x 2 meter volume. and (d) shows the lab coordinate system. The scale on the graph is in meters. The the subject's skeleton and the traced path in the 3D space are plotted. The color dots correspond to a subset of the fifty active-pulse LED markers on the suit and the virtual-reality helmet. Related to Figure 2.	26
3.2	The nine 3-dimensional paths in the virtual environment that were used in the experiment. For reference, colors denote common segments and points. For the subjects, the curves were all rendered in black, The scale is in meters. Related to Figure 1.	27

3.3	PhaseSpace suit with 50 active-pulse LED markers. The numbers next to the LED markers are the marker indexes used for recording the motion capture data.	30
3.4	Classifications of starting postures. The view is from the top of 3D space and the black curves are the nine paths used in our experiment. The yellow dot on each curve indicates the starting position of the target sphere. The dots around each curve represent the average starting locations of head markers of the subjects while tracing this curve. The direction of each arrow is the direction from the head marker to the right index finger marker for each subject. Colors denote the different clusters classifications. For example, in Path 5, the square curve, only two starting postures were used. The distribution of the chosen initial postures for each path was shown in Table 3.2.1. For curves 2,4,5 and 7, one posture is overwhelmingly preferred over the others. The 3-dimension view of all nine curves were shown in 3.2	41
3.5	Tracing data analysis for path5. (a) the skeleton clouds of 90 trials (18 subjects each with 5 repeats) when subjects' right index fingers reaching the two corners of the square path. (b) highly stereotyped postures generated by 90 trials. The spheres with different colors represent different markers. The central location and the size of a sphere indicate the mean position and the standard deviations of the corresponding marker, respectively. Related to Figure 3.1 and Figure 3.3.	43

3.6	Posture matching results of square tracing at frame 300. At the outset, for each frame, the mean posture at that frame is computed by averaging the postures at that frame. Next, the relative postures for frame 300 are compared to relative postures other frames selected at 20 frame intervals. The colored dot represents the mean of euclidean distances between checking relative postures at frame 300 and relative postures at other frames. The blue bar indicates the corresponding standard deviation. The colors of dots indicate the relative height from the laboratory floor with blue being the lowest and red the highest. In this example, the relative postures at frame 300 are the best match. The fact that all the other matches have higher distance measures indicates that the chosen match point is dissimilar to all the all the other points on the traced curve.	45
-----	--	----

3.7	Posture matching results for nine curves. The horizontal axis represents the checking frames, which were taken once every 20 frames. The vertical axis represents the frames of relative postures that were best matching with the postures at checking frames. Two red points and two yellow points indicate the matching results of the four fixed points in the virtual 3D. The two colors signify that these points were constrained to be at the same height. Naturally many subsets of blue points may have the same height, but this property was not checked. The net result is that almost every relative posture at each frame for each curve is unique. Given at least 50 samples per path and 9 paths, a total of more than 22,000 comparisons were made. This calculation makes the result that almost of the 450 perfect matches are seen, even given that in many of the match pairings the tracing finger is at the same vertical height, remarkable.	46
3.8	The match column compares matches of postures at their original location to the mean posture at that location. The non-match column compares matches of postures to matches to the other mean postures on the curves. All nine curves are used in this comparison. This difference is obviously hugely significant, implying that the methodology is highly reproducible as postures that are at distal sites on the traced curve are very dissimilar. The t-test of this data shows that the difference is significant at the 0.0001 level.	48

3.9	Comparison of the standard deviation of marker positions. At each frame, the mean position of a marker was first computed, then we calculated the Euclidean distances between each of the positions of the marker and its mean position, finally, the standard deviation of the positions of the marker was computed. The corresponding average standard deviations averaged over all the frames of each curve are shown in Table 3.2.3.	49
3.10	The standard deviations in repeated traces for four randomly chosen subjects are compared to the average. To do this,for each ten frame interval, the standard deviation of points is computed. Using this data the average standard deviation of this data is computed. Next, the individual variances are correlated with this average. For colors signify four random subjects. The high R values indicate that subjects' variances, which indicates their cocontractions, are co-varying. All the R values for the four markers computed for all nine curves show positive correlations. (See also Table 3.2.3)	52
4.1	The HDM user interface showing a frame from the tracing data analysis. The system supports control and visualizations of model parameters and relevant data so that users can simulate and analyze physically-based movements conveniently. The programmed parameters of the model consist of physical world parameters, joints constraints, and the model's body-marker relative positions. More details have been described in Chapter 5.	61

4.2	Model capability illustration. A punch sequence reproduced using inverse dynamics and the recorded motion capture data from a human subject.	62
4.3	The 48 degrees of freedom model A. Hinge joints connect the toes and the heels. Universal joints are used at the wrists, elbows, knees and ankles. Four ball-and-socket joints connect five body segments along the spine from the head to the waist. Ball-and-socket joints are also used at the collar-bone, shoulder, and hip. B. A summary of the joints used in the model. c. = chiral: there are two of each of these joints (left and right). All joints limit the range of motion to angles plausible for human movement. Our model assumes that joint DOFs summarize the effects of component muscles.	64
4.4	Three types of joints which were used in the dynamic model system.	65
4.5	Marker arrangement on the motion capture suit. The suit contains 50 markers, as shown by the LEDs in total, but only 41 are used in the dynamic model, e.g., Markers that are used are present in the figure. Markers can easily be assigned to specific model segments. For example, the markers of RBHD, RFHD, LFHD and LBHD are assigned to the Head segment, while the markers of RBWT, RFWT, LFWT and LBWT belong to the Pelvis segment.	67

4.6	Joint angle trajectory reconstruction. The solid lines represents the ground truth, while the dash lines indicates the recovered angles. Simulating joints as spring smooths the ground truth but makes the recovered data lag behind a little bit. (a) and (b) shows the trajectories of selected joints along the x-axis and the selected body segments along the y-axis.	76
4.7	Body position trajectories reconstruction It shows the trajectories of selected body segments along the y-axis. This figure can be considered as a top view of the 3D motion and the projection of 3D trajectories of body segments on the ground.	77
4.8	Model noise sensitivity [61]. The error of joint angles and internal torques with Gaussian noises. The process was repeated 20 times for each noise level with 9 different standard deviations that were (0.1, 0.5, 1, 2, 4, 8, 16, 32, 64) in mm. Error bars show the standard error of the mean. (a) The accuracy of the PhaseSpace motion capture device is approximately 5mm over its 3 x 6-meter workspace, resulting in an average angular error of 1 degree. (b) The same estimates for torque error are between 5 and 10 Nm, typically approximately 1%. These small errors are well within the requirements for our experiments. (c) Reconstructed poses. According to Gaussian perturbed walking data (0.1mm, 8mm, and 64mm noise levels), first use inverse dynamics to compute joint torques at each frame and then use forward dynamics to reproduce the walking motions. Although the model follows the reference motion poorly at very high levels of noise, the movement still looks, qualitatively, like walking. .	78

4.9	Comparing ground forces between the model and the Wii force plate [61]. (Top) Two Wii force plates serve as an accurate calibration reference. A subject stood on the two plates and then changed stances, balancing first on the left foot and next on the right. (Bottom) The comparison between the measurement systems is surprisingly good, during the stance phases, showing only a 5% difference between the <i>measured</i> ground forces and the <i>computed</i> forces.	80
4.10	Reaching in a virtual reality environment [61]. A) A subject reaches to touch virtual targets seen in a HMD. The subject's reach is unconstrained. B) The subject reaches the different numbered targets on separate trials. C) The average integrated torque over ten trials per reach shows that the method reliably discriminates between movement costs for the further and higher locations.	82
4.11	Comparison of efforts while walking with/without arm swing. (a) In a preliminary test of our design, the energetic cost of normal walking is compared to the case where the arms are constrained from swinging. We hypothesize that if subjects are instructed to walk without moving their arms, they will accomplish this by using muscle co-contraction and that this effect can be realized in the human dynamic model with stationary markers that keep the arms vertical. (b) The increased cost measured by the human dynamic model is 6.1 %, extremely close to the 6 % result obtained by Ortega [79].	84
4.12	Apply the PCA algorithm to six different walking sequences. .	85

4.13	Movement control using dynamic synergies Markers in green are attached, while markers in red are detached. Thus, as shown, the left postures are pretty close to the right one.	87
4.14	Comparison of joint angles along the selected degree of freedom Solid lines show joint angles recovered based on the full marker set. Dashed lines show joint angles recovered based on reduced marker set.	88
5.1	Big picture of the human dynamic model system.	92
5.2	The markers settings of motion capture data and the body settings of our Human dynamic model	93
5.3	The mappings and an example of a mapping file. In the mapping file, the index of a row represents the index of a marker. The value on each row indicates the index of the assigned body segment. For example, the first-row index is 12 means the marker of which the index is 0 should be assigned to the body segment with index 12, which means marker "LBWT" is attached to the body segment named "WAIST_BODY".	94
5.4	The custom mocap data and the corresponding mappings. (a) In the CSV file, the columns indicate marker positions in order. Every four columns represent one marker position (x, y, z) followed by a credibility value C. According to the motion capture system, if C is between 4 and 10, the recorded positions have high credibility. One row illustrates all the markers' positions at one frame.	97

5.5	User Interface of Human Dynamic Model System. It consists of a display panel, a control panel, and a functional panel. In the figure, the display panel shows the initial state of the whole system. The human dynamic model was initially located in the middle of the simulated world and connected with all markers. Green points represent the attached markers, and green lines illustrate their connections with associated body segments. . .	98
5.6	User Interface of Human Dynamic Model System – Graph display panel and functional panel. Users are able to choose to plot desired information, and the result will be shown on the display board on the left.	99
5.7	An illustration of the control panel	103
5.8	The Joint sub-panel and the Dimension sub-panel	108
5.9	The shapes and dimensions of body segments.	111
6.1	The nine 3-dimensional paths in the virtual environment that were used in the experiment. They are ordered by their complexity. For reference, colors denote common segments and points. For the subjects, the paths were all rendered in black. The scale is in meters.	114
6.2	Model capability illustration. Four points in a tracing sequence reproduced with physics-engine-based inverse dynamics using recorded motion capture data from a human subject.	116

6.3	The power of tracing path 1 at each frame. Nine subjects traced path 1 five times. The plot shows the average joints' power at each frame across subjects. The blue line indicates the mean, and the gray shaded area represents the standard deviation of powers. The small standard deviation means that different subjects had similar power patterns while tracing the same curve, which shows that the curve has points of difficulty in tracing shared by the subjects. Path 1 is the most straightforward, but the observation of correlated effort represents patterns in tracing other curves.	120
6.4	Energetic costs of tracing path 1. Each subject traced path 1 with five repeats. The horizontal labels indicate the related subjects, e.g., "S1" represents the subject1. The total cost is shown in blue, and the portion of the cost due to residual forces are shown in orange. A low cost in residual forces usually signifies that the dynamic model matches that subject's kinematic data.	121
6.5	The energetic cost of tracing nine paths. These results portray the possibility that the costs vary across the best-fit five subjects. The statistics show that each path traced has a unique cost that distinguishes it from the rest.	122

6.6	The difference in the energetic cost for the model perturbation. The figure shows the difference in the energetic cost of tracing each of the nine paths with perturbations in the right-elbow marker. The elbow was moved up 5cm. The results show that the original path is always the least expensive for all the paths and the averages across subject tracers. Moreover, the differences between the energetic costs of original trajectories and perturbed trajectories are highly significant, with a p-value less than 0.001.	124
6.7	The difference in the energetic cost for the path perturbation. Each of the nine paths has two perturbations of 5 cm: left in blue, right in green. This main result shows that the original path is always the least expensive for both averages across subject traces. The difference in the energetic cost for the path perturbation is not very clear but still reliable, with a p-value less than 0.01.	125
6.8	The residual torques The average of the means of the cost changes for nine paths with five repeats across five participants.	127
7.1	Standard Gaussian process with 1D kernel fitting the tracing data of marker 8 along the x-axis.	138
7.2	Standard Gaussian process with 3D kernel fitting the tracing data of marker 8.	139
7.3	Sliding window Gaussian process with 1D kernel fitting tracing data of marker 8 along the x-axis with different sliding lengths.	140

7.4	Sliding window Gaussian process with 3D kernel fitting tracing data of marker 8 with different sliding lengths.	142
7.5	Hyperparameters modeling for sliding window Gaussian process with 1D kernel fitting tracing data of marker 8 along the x-axis with different sliding lengths.	144
7.6	Hyperparameters modeling for sliding window Gaussian process with 3D kernel fitting tracing data of marker 8 with different sliding lengths.	145
8.1	An illustration of motion capture data used in the locomotion experiment.	150
8.2	An illustration of mapping markers to appropriate body segments.	151
8.3	An illustration of fitting the human dynamic model to motion capture data.	152
8.4	Simulation of the human dynamic model walking on rough terrains. The brown boxes were dynamically generated according to the real motions.	153
8.5	Simulation of a subject walking on rough terrains over three different paths. JAC is the subject's name, followed by the number 1,2, 3, which indicate different walking paths.	155
8.6	An illustration of the keyframing method.	156

8.7	An implementation of a 2D five-link biped robot in a 3D environment. (c) fits the five-link robot (red model) to the human dynamic model (blue model). The blue model is the previous version of our human dynamic model. The red dots are the desired markers. Their trajectories will be used as the inputs of the PCA learning machine.	160
8.8	The overview of missing body positions estimation algorithm.	162
8.9	A reconstruction experiment using the PCA learning machine.	163
8.10	The performance test of the PCA learning machine.	164
8.11	Arbitrary walking sequence synthesis. The blue model is a previous version of our human dynamic model.	165
8.12	Tracing synthesis. The blue line represents the three-quarter of path 1, and the red line represents the last quarter of path3. The dynamic human model was smoothly tracing the new curve given the synthesized motion capture data.	168
8.13	walking in a maze. The maze is designed as follows: 1) green grid is the initial position, 2) red grid is the destination, 3) yellow grid is the place that the planned path must be through, 4) the grey cubes are the obstacles. The green line in the air shows the planned optimal route.	169
8.14	Scheme of the optimization algorithm The X0 represents the system's initial parameters, e.g., X0 could be the markers' positions relative to body segments. The X' and Q' describe the intermediate results during the process. The Xopt represents the optimized parameters.	171

Chapter 1

Introduction

This dissertation presents research into capturing and analyzing whole-body human movements, simulating, and analyzing those movements' energy costs. A real-time interactive virtual reality environment was developed to control the experimental protocol and record the movement data. After capturing enough data, we process the motion data using some open-source dynamic libraries and then design several novel methods to get sights into their regularities. Sequentially, we simulate the virtual tracing movements on an existing forty-eight degree of freedom dynamic human and analyze their corresponding dynamic properties. This dissertation aims to test the hypotheses that regularities in the kinematics of a movement may indicate regularities in its energetic cost. More specifically, given a common goal, humans present common movement patterns in the trajectory of the bodies' limbs, and one possible explanation for this generality could be that humans choose trajectories that are economical in energetic cost.

1.1 Motivation

In difficult movement tasks, such as retrieving an object from a cluttered environment or choosing balance positions for transporting a large, unwieldy object, humans are inventive problem solvers, but at the other end of the movement spectrum in most everyday repetitive movements such as walking, sitting and reaching humans exhibit large degrees of regularity [9, 94, 29, 30, 75, 25]. In the quest to understand the human movement system, it would be essential to know if general movements have regularities across subjects as it would provide an essential scaffold in the development of more detailed dynamic movement models.

There are at least two broad perspectives that suggest such use of regularity principles. One is the Bayesian perspective. Its adherents argue that this repeatability arises because such movements are committed to memory with precedence based on the probability of use [111, 42, 49]. Such familiar movements even incorporate settings that anticipate perturbations. This repeatability has led to movements being subject to extensive analysis. However, the focus has been on the exogenous constraints of the external task, rather than the much more complex endogenous constraints of the internal movement system that come into play more during large-scale movements.

The other perspective comes from advances in models that can compute the joint torques in human-scale skeletal models. Early models attempted to model dynamics as an inverse problem that attempted to estimate the torques by modeling regularizing the dynamics equations as under-constrained systems proved cumbersome and prohibitively expensive. The newer models linearize the dynamic equations and use feed-forward methods that are much better

conditioned [22, 18, 26].

These methods show that the kinematics of a movement is directly related to its dynamics, thus raising the possibility that regularities in the energetic cost of a movement may be indicative of regularities in the kinematics.

1.2 Overview

The program of the research is organized around three sequential sub-projects (Fig. 1.1).

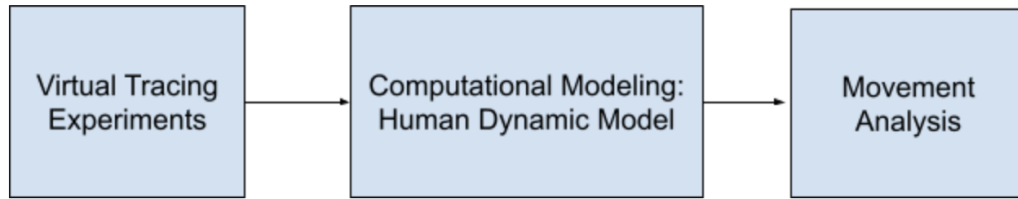


Figure 1.1: The overall organization of the research.

In the beginning, we are interested in the *principles* behind large-scale arbitrary movements, particularly concerning variations between different subjects. For example, given a goal-directed task, do the movements appear similar across subjects, or are movements very individualized? To solve this problem, we developed a full-body virtual tracing task to elicit natural movements under common goals shared by all subjects. During a trial, participants traced a series of paths in a virtual environment. They wore a virtual-reality helmet to see the virtual curves and a motion capture suit to record their body movements simultaneously. One participant completed five blocks of the task plus a practice tracing. Each block includes nine trials of different paths that

were large enough so that participants need to plan and execute sequences of full-body movements, including walking, crouching, and so on, to complete a trial. Each trial typically takes about 30 seconds to complete. In all, 270 minutes of whole-body human tracing motion capture data were gathered. We then developed specialized aggregation methods for data analysis that extracted similarities of posture sequences in the face of kinematic variations. Additionally, we analyzed the fine structure of the variations used by subjects during the tracing task. The exciting and unsuspected result was that both the movement’s posture sequences and kinematic variations showed striking commonalities across subjects but in aggregation [62].

Thus such correspondences require advanced methods for understanding and testing large-scale movement principles. Nonetheless, given the recent development of methods for extracting muscle torques from human dynamics models, a prominent and straightforward inference drawn from our observed similarities in posture sequences is that similar movements may be selected to achieve low energetic costs. To prove this hypothesis, a dynamic computational model capable of simulating, analyzing, and synthesizing humanoid movements was created: a human dynamic model¹. It was built on top of an open-source physical engine, Open Dynamic Engine, which is fast, robust, intuitive, and inexpensive. The model consists of twenty-one body components connected by twenty joints, including forty-eight degrees of freedom. One creative idea is that the joint connections are not considered as holonomic constraints but as stiff springs instead, which hold two body parts together just like muscles. The model allows computing instantaneous power from the product of net joint torque and joint angular velocity. The mechanical work performed at each joint

¹The HDM model: https://github.com/EmbodiedCognition/HDM_UI

was determined by numerically integrating the instantaneous powers over the entire tracing task. In this way, the energy cost of human motions can be computed given motion capture data. The model was originally defined by Dr. Cooper and now has been further improved and validated [61]. A demo of utilizing its user interface has been uploaded online ².

Once the computational modeling part was completed, we utilized the model for computing the energetic cost of movements gathered from the virtual tracing experiments. To prove that humans prefer posture sequences that cost minimum energy, we referenced a classical method of analyzing human movement energetic cost. For example, in locomotion, while studying if humans' walking step frequency [19, 115, 12, 38, 68, 25, 101] is corresponding with the minimum metabolic cost, researchers will first allow participants to walk at their most comfortable frequency and then adding constraints gradually. As a result, the energetic cost consistently exhibits a U-shaped dependence on step frequency while walking at a constant speed [114, 68] and the minimum of the U-shape curve is consistent with the self-selected or preferred walking frequency. In our virtual-reality tracing tasks, subjects traced large-scale paths that required a series of whole-body movement sequences. They could freely choose their starting postures and were given no instructions on how to comport themselves during the tracing process. In other words, participants were tracing curves at their preferred posture sequences. Therefore, we first computed the energetic cost of the gathered participants' movements, and then we add constraints to those original postures, such as restrict arm trajectories, perturb motion capture data, or relocate the virtual path, etc. The cost of original virtual tracing movements and perturbed movements were computed and

²HDM UI Demo <https://youtu.be/ASs4Wo5PQcM>

compared using the human dynamic model. The energetic cost consistently exhibits a U-shape while tracing using different postures sequences, with the minimum of the U-shape curve consistent with the original posture traces, which our subjects self-selected.

In addition, the results of kinematics analysis of motion trajectories in the virtual tracing experiment reveal that when the average local markers' standard deviation for all the traces increases, the standard deviation of the individual traces increases in a correlated way. This correlation may be a consequence of constraining the degrees of freedom of the task with muscle co-contraction. Muscle co-contraction occurs when two muscle groups surround a joint contract simultaneously to stabilize one's limbs. Previous studies showed that muscle co-contraction is closely related to movement status [76, 77, 88, 67, 33], such as movement speed, the accuracy, and variability of repeated motions, etc. As the kernel's hyperparameters of a Gaussian process embody the variance and correlations of the training data, we believed that value changes of hyperparameters could be a way to imply the muscle co-contraction. We then further analyzed the movement variations as a correlation of muscle co-contraction using a sliding window Gaussian process algorithm. We trained a local 3D kernel using the movement data within a window, slid the window a few frames forward, and repeated this process until the end. The estimated hyperparameters' values at each frame were the average of the corresponding values across all the windows that covered this frame. As expected, the results showed that apparent changes of hyperparameters' values around the frames were related to corners of tracing curves. However, further experiments with electromyography would be needed to settle this definitively.

1.3 Principal Contributions

This research involves multiple disciplines and has provided a novel method for complex human movement analysis. This work aims to study the regularities of human movements from the perspectives both in kinematics and dynamics. We accomplish this goal by conducting a virtual-reality experiment and utilizing a dynamic human model [18, 61] to solve multiple problems associated with human motion capture, human movements simulation, and large-scale data analysis.

The main contribution of this research is derived from the extraordinary elaboration of the human movement system. Although cortical motor areas have been extensively studied, their primary response properties are still poorly understood, and it remains controversial whether neural activity relates to muscles or abstract movement features [14]. We provide a new perspective of how movements may be processed in the brain by showing that humans chose trajectories with minimum energy cost while accomplishing goal-directed tasks. Furthermore, while most of the current neural control studies are analytical, our research uses a computational methodology. More specifically:

1. An interactive virtual-reality experiment for gathering goal-directed human whole-body motion capture data has been developed.
2. Novel methods to study the kinematics and dynamics of human movements have been designed and implemented.
 - 2.1. A method for human whole-body postures comparison.
 - 2.2. A method for extraction variance in human movements.
 - 2.3. A method for analyzing energy cost of human movements.

- 2.4. A method for analyzing the relationship between the kinematics results and dynamics results.
3. The dynamic human model has been improved based on our research purpose. In addition, we further developed its user interface so that it becomes user-friendly and can be used as a standard analyzing tool for human movement.
4. The measurement of the energy cost and joint torques exerted by the dynamic humanoid model during a particular movement sequence can be beneficial for clinical diagnosis and rehabilitation.
5. A potential novel way for detecting muscle co-contraction has been provided.

These novel contributions are beneficial for clinical studies, biomechanics, and psychophysics.

1.4 Organization

This dissertation is organized as follows:

Chapter 2 generally discusses the background of some research areas relevant to this dissertation, including the basic concepts in the neural control of human movement, technique tools of computational modeling, and the straightforward and frequently used techniques for analyzing the energetic cost of human movement.

Chapter 3 covers our work of developing a virtual tracing experiment to elicit humans' natural whole-body movements under common goals. This

chapter illustrates the virtual reality protocol, describes the method of motion data analytic in detail, and discusses the possible interpretation of the experiment results comprehensively. It also includes the limitations of this study.

Chapter 4 and Chapter 5 demonstrate the computational modeling: human dynamic system. Chapter 4 describes a method of building a dynamic human model on top of an open-source physical engine and several tests to assess the model's performance. It focuses on the model's topology and its validation. Chapter 5 illustrates the big picture of the dynamic system, the configuration, and the user interface. It focuses on how to use the system.

Chapter 6 presents a way to employ a forty-eight degree of freedom dynamic human model to analyze the energy cost of movements gathered from the tracing experiment described in chapter 3.

Chapter 7 introduces a related study to apply a sliding window Gaussian process method on training data to detect potential muscle co-contraction. This experiment took advantage of the motion capture data collected from our virtual tracing experiment and exhibits expected results.

Finally, chapter 8 proposes several possible directions for future work. This chapter focuses on illustrating the studies of walking on terrain and simple single-behavior motions synthesis. The experiments of these two studies and their preliminary results have been explained in detail, respectively. Another three possible directions are briefly discussed as well.

Chapter 2

Background

2.1 Neural Control of Movement

The human movement system is extraordinarily elaborate. Over six hundred muscles have approximately three hundred degrees of freedom controlled synergistically using a collection of cooperating brain subsystems, each with specialized functions. To deal with this complexity, the movement system integrates a number of specialized subsystems that cooperate. While there are many open questions concerning the internal details of these subsystems, their functionality in the outline is well-known. Reflexes in the spinal cord implement upright posture and balance control and other movement aspects through error control [74, 104, 24]. The cerebellum uses an internal dynamic model to predict the consequences of a movement, both to handle unexpected deviations and to reduce delays [23]. The basal ganglia monitors breakpoints in extended movement sequences [51, 43]. The cortex has the task of choosing the movements given sensory descriptions of the task at hand [3]. Among this group,

the motor cortices have the unique responsibility of planning and choosing movements that anticipate distal situations gleaned from vision. Although the other subsystems have specialized functions, they are predominantly geared to producing movement control in real-time.

Although the motor cortices are involved in representing movements, some issues are surrounding their organization. Foremost is the job of converting the description of the desired movement, which will be in allocentric coordinates into egocentric posture coordinates. The original micro-stimulation experiments elicited localized body movements correlated with the organization of the topography of M1. However, stimulations with an increased magnitude of elicited whole-body movements could be interpreted as task-specific [32]. Thus low-level stimulation reveals the basic posture coordinates of the homunculus, but higher-level simulations reveal that these posture changes reflect different goals. Given these data, a more refined issue arises from the content of the motor cortex's specific representations. The control of a movement with the musculoskeletal system requires posture kinematics, torques, and stiffness settings. Of these possibilities, logic suggests that the specification of the associated torques is the province of the spinal cord. One reason is that the low spike rates in M1 are inconsistent with the high bandwidth control of torques needed for real-time control. Another is that while the posture change may be invariant to many situations, the unpredictable variations in load dictated by the versatility of the body's task-oriented loading make the specification of torques an unlikely candidate for long-term cortical memory.

An additional argument can be made from models of the dynamics of the musculoskeletal system itself. Given the kinematic specification, it is possible to compute the requisite joint torques [57, 22, 18], but the result is delicate and

in using the result has to be stabilized by other systems such as spinal cord reflexes and input from the vestibular system [18]. Thus the focus of the motor cortices is likely to be on specifying the desired posture changes. The method for doing this is still an open question, but recent research suggests that the computation requires on the order of seconds, excluding a role in real-time control [92]. In summary, the most likely representation used by movement memories in the cortex is in terms of kinematic posture changes and possibly stiffness settings. These observations motivate our choice of posture kinematics as our central data structure.

Most everyday repetitive movements such as walking, sitting, and reaching humans exhibit large degrees of regularity [9, 94, 29, 30, 75, 25]. A Bayesian perspective would argue for organizing a movement memory to give precedence based on the probability of use [111, 42]. The organization of familiar movements extensively has been studied, and many results suggest that they are highly stereotyped. In particular, walking has been extensively studied [8]. For example, in ascending and descending stairs, humans use their torso as a counterweight for stability [35, 93]. Reaching has been much studied also, but from the perspective of whole-body movements, the setting is typically very constrained [46, 45, 40].

Even if the movement memory is in terms of kinematics, it can only be a movement plan. Unexpected perturbations from the environment regarding unstable footing or unexpected loads will call for dynamic adjustments in the spinal cord circuitry. Thus it is likely that between participants, movement plans might exhibit a significant degree of variation.

Body movements are challenging to study owing to their variation. Bernstein’s famous well-known phrase characterizing repeated movements in

terms of “repetition without repetition” emphasizes that repeated movements are never the same [7]. However, repeated movement variations are never entirely random. Informed by task goals, subjects can shape the variations in different parts of the body by co-contracting muscles to achieve desired dynamics in different sections of a trajectory [55]. Thus in looking for regularities in movements, one has to deal with both that the trajectories will vary owing to muscle co-contraction and that the amount of co-contraction itself can be modulated throughout the movements.

We were interested in their extent of variation, particularly in a situation of whole-body movements governed by a task, but one that would allow different participants freedom in choosing movements to solve it. By choosing their posture sequences, would posture changes appear similar across participants as in common everyday movements, or would the movements be very individualized? To address this problem, we chose an extended task that requires whole-body movement sequences. Participants traced a large-scale curve in virtual reality that required that they make several steps. Meanwhile, their posture was recorded using a 50-marker motion capture suit. The central question was whether or not there would be any similarity in the tracing postures.

We designed a simple posture matching method and analyzed the variance of participant movements at video frame rates to qualitatively measure the similarity of human motions. The surprising result was that the posture sequences used by different individuals were nearly identical, suggestive of a common organizing principle. Therefore, the commonality of the result spurred the search for explanations for its generality. One of the principles could be that humans choose trajectories that are economical in energetic cost.

2.2 Computational Modeling

The complexity of human motion was first dramatically captured via the Muybridge high-speed photographs [112], which spawned many different analysis techniques in different disciplines. Visualization first used keyframing techniques, but later sophisticated models were used in advanced rendering for computer graphics [116]. The early cognitive analyses of human behavior [4] focused on human motion in problem-solving, using an essentially logical approach. In robotics, sights have been obtained by building physical systems directly [41] that straddle the boundary between humans and robotics that have shed light on human design. However, these efforts are characteristically specialized. In another development, machine learning techniques have been introduced for use in analyzing animal-like motion[89].

Most recent advances in the speed of computing and novel formulations of the dynamic equations of motion have engendered a new approach to understanding human movement fundamentals. As a result, large-scale human movement models can be built to understand how humans generate goal-oriented behaviors in real-time. However, modeling all the complexity of the human musculoskeletal system can be daunting, with over 600 muscles controlling a complex skeletal system with over 300 degrees of freedom. Moreover, to control this complexity, in addition to its vast cortical memory system, the forebrain coordinates specialized subsystems such as the Basal Ganglia and Thalamus in realizing human real-time movement coordination. The upshot is that progress tends to be specialized [11], and there are many open problems [63].

In the face of these complex challenges, a major alternate modeling

route is to forego the neural level of detail and muscle features and then model more abstract versions of the human system that still use multiple degrees of freedom but summarize muscle effects through joint torques. The computation of the dynamics of such multi-jointed systems recently has also experienced significant advances. The foremost of these, use a kinematic plan to integrate the dynamic equations directly. Thus there is a need for an exclusively human movement-based model that could be used to inform laboratory experiments[10], clinical studies, e.g. [52] also verifies experiments that have only qualitative results[54, 84]. Several different dynamic libraries exist, such as MuJoCo¹, Bullet², Havok³, Open Dynamic Engine(ODE)⁴, and PhysX⁵. An evaluation by [26] found them roughly comparable in capability, and our HDM system is built on top of the physics engine ODE, which is the most commonly used dynamic library in the robotic area.

The human dynamic model (HDM)⁶ has a singular focus on human movement modeling and uses a unique approach to integrating the dynamic equations. A direct dynamics integration method extracts torques from human subjects in real-time [44, 18, 17] using a unifying spring constraint formalism. It has two significant innovations added to handle the closed-loop kinematic chains of bipedal movements and the contact constraints they introduce, which have proven difficult to model. One is to allow the kinematic makers of a motion capture system to be modeled as enormous point masses. The result is to stabilize the integration of the underlying dynamic equations. The other

¹MuJoCo <http://www.mujoco.org/>

²Bullet <https://pybullet.org/>

³Havok <https://www.havok.com/>

⁴OpenDE: <http://www.ode.org/>

⁵PhysX: <https://developer.nvidia.com/gameworks-physics-overview>

⁶The HDM mode: https://github.com/EmbodiedCognition/HDM_UI

is to allow the reduction of contact constraints into stiff springs, which has the result of allowing the incorporation of external forces and points of contact.

The focus of chapters 4 and 5 is to describe the human dynamic model simulator as a practical laboratory instrument as well as describe demonstrations that lend support to the kinematic plan approach to movement memory. These goals are illustrated and evaluated in several different demonstrations to illustrate the versatility of the method.

2.3 Movement Analysis Techniques

A general principle of human movement is that our nervous system should exhibit trajectories that are economical in energetic cost [110, 99]. It has been established for decades and has been well studied in simple movements. For example, in locomotion, there are a number of experiments showing that humans' walking speed [81], step frequency/length [19, 115, 12, 38, 68, 25, 101], step width [66, 2] are all corresponding with the minimum metabolic cost. In particular, energetic cost exhibits a U-shaped dependence on step frequency while walking at a constant speed [114, 68], and the minimum of the U-shape is consistent with the self-selected or preferred walking frequency. Furthermore, new evidence [90, 87, 113] shows the system can adapt preferred gaits to minimize energetic cost in response to varying loads.

In the past, a common way to address the minimum energetic cost principle was to conduct experiments comparing walking and running with many other strange and unpractised gaits [64, 39]. Nowadays, there are three commonly used methods to study energy optimization.

The most straightforward and frequently used method is to measure the

metabolic cost, e.g., subjects breath through a mouthpiece to measure oxygen consumption rates (VO_2). For example, subjects were required to walk under different circumstances, and the results showed that the metabolic cost was minimum while subjects walked at the condition which was "comfortable" for them [81, 19, 115, 12, 90, 87, 113]. The advantage of this method is that movements can be related directly to energetic cost, but the measuring apparatus is typically very constraining.

A common way to measure muscle co-activation and stiffness is to use Electromyography (EMG). Huang et al. [40] showed that that subjects' metabolic cost is reduced during the learning process of arm reaching tasks, and their muscle activities and co-activation would parallel changes in metabolic power. However, EMG measures just a correlate that needs additional modeling to turn it into an energetic cost.

The third method, dynamic modeling, is to build a closed-form analytical mechanics-based model and determine if the predicted minimum mechanical cost correlates with people's kinematic preferences. For example, [38, 68, 25, 66] use an inverted pendulum model to predict the optimal step length and compare it with the subjects' natural step length while walking.

All these methods pose obstacles for calculating the energetic cost of whole-body tracing movements collected from the VR experiment [62]. These methods are time-consuming, and the required configuration restricts the variety of experiments. For example, the VO_2 process does not work for our virtual-reality tracing tasks as subjects need to wear the VR helmet on their head, leaving little space for a mouthpiece. Besides, the EMG method measures muscle co-contraction, which is correlated with energetic cost, rather than calculating the cost. Another possible way is to build a humanoid dy-

dynamic model. The method is the best way to imitate human movements, and it is widely used in biomedical engineering due to its compliance with real-world physical rules. However, it has several critical limitations: 1) it is too difficult to model and control a large system as the equations of motions in nested, rotating reference coordinates will be extremely complex, such as a whole human body. 2) it is challenging to represent the kinematic close loops of skeleton chains, such as postures that need both feet are on the ground. Due to the complexity and disadvantages of the dynamic modeling method for large complex systems, most of the studies took advantage of two-dimensional models to study human part-body motions in the sagittal plane.

There are some methods of building a dynamic 2D bipedal robot by modeling the whole body with a skeleton of rigid segments connected with joints. However, those methods over-simplify human bodies so that they can only study simple single-behavior human movements. The simplest bipedal robot uses three links to represent the torso and two legs in the sagittal plane [56, 13]. Five-link biped robots extend the model using two links to represent each leg [72, 73, 71, 50], while seven-link biped robots further extend it by adding feet to it [70, 5]. Furthermore, those methods have many assumptions while studying human locomotion. For example, most researchers assume that instantaneous exchange of the biped support legs occurs when the swing leg contacts with the ground. In this way, the biped locomotion with single foot support can be considered as a successive open loop of kinematic chain from the support point to the free ends, as robot manipulators. Recently, 3D modeling of biped robots [34, 47] has been developed. However, they are still not sophisticated enough compared with a real human body.

In the face of these complex challenges, we developed a 48 degree of

freedom human dynamic model (HDM) that is able to simulate and compute the energetic cost of human movements. While doing the virtual tracing experiment, subjects freely chose their starting posture and were given no instructions on how to perform themselves. Therefore, participants were tracing curves at their preferred posture sequences. In other words, they traced curves under the conditions which were “comfortable” for them. Therefore, according to the previous experiments [81, 19, 115, 12, 90, 87, 113], we can expect that the energetic costs of movements with those trajectories should be a minimum or at least locally minimum. To support our conclusion, the cost of original virtual tracing movements and perturbed movements were computed and compared using the human dynamic model. As expected, the energetic cost consistently exhibits a U-shape while tracing using different postures sequences, with the minimum of the U-shape curve consistent with the original posture traces, which our subjects self-selected. In this way, we are able to demonstrate that the energetic cost of original trajectories is a local minimum. The focus of the chapter 6 is describing how we conducted this experiment.

2.4 Motivation for our research setting

The adherents of the Bayesian perspective argue that this repeatability arises because such movements are committed to memory with precedence based on the probability of use [111, 42, 49]. Thus, the critical question is: for the larger movements, do the component posture changes also appear similar to common everyday movements, or are they very individualized across different subjects?

We sought a task that would test the extent of variation, especially in whole-body movements governed by a common task, but allowed different sub-

jects freedom to choose movements to solve it. The task studied had subjects tracing large-scale three-dimensional curves in virtual reality that required a series of whole-body movement sequences. Subjects could freely choose their starting posture and were given no instructions on how to comport themselves during the tracing process. Their postures were continuously recorded using the fifty sensors motion-capture system. The central question was whether or not there would be any similarity in the postures used during tracing. To study the regularity of repetitive movements, we developed specialized aggregation methods for data analysis that extracted similarities of posture sequences in the face of kinematic variations [62].

Creating an experimental setting requires a way of measuring the kinematics of a movement. Models of human movement typically divide anatomical parts into discrete segments with their inertia and are interconnected by mostly rotary joints. Thus a movement can be described as the time course of the coordinates of the joints. Our experimental setting uses an equivalent set of fifty three-dimensional coordinates of a motion capture suit. The time course of these coordinates provides an equivalent representation of a movement’s kinematics. To refer to the kinematics at a specific time, we use the term *posture*. Classically, posture is used for particular poses such as sitting or standing, but we use it for all body orientations tested. The posture formalism allows for a remarkably straightforward method of testing the similarity between two postures: compute the Euclidean distance between every matching pair of markers and add them up. Although this method will not work for cases where two postures are very contorted concerning each other, it is sufficient for the situations measured in our experiment.

The main result was that although the tracing data exhibit posture vari-

ations, both in repeated of a single subject and in trials by different subjects, the average postures show marked regularities in several aspects of the data that was subject to analysis. A t-test between a proximal relative posture and distal relative posture showed that the difference is significant at the 0.0001 level. Also, the variances in the subjects' postures were correlated. If the variance of a trace calculated from a subject at a point on the curve was relatively large, the average variance of all the repeated trials from all subjects would be relatively large also. Given all these kinematic similarities, we were motivated to do the subsequent study that showed the body torques also exhibited corresponding commonalities, which resulted in similar energetic costs.

Energetic costs have been studied extensively, and it is well known that under many conditions, humans choose minimum cost trajectories for reaching [21] and walking [114], but our study has several unique features:

1. The movements in our data set were freely chosen, involving multiple steps.
2. We had shown that the postures of our subjects were essentially identical across subjects and repeats by the same subject.
3. We used a human dynamic model to calculate the cost of the movements.

This dynamic system is built on top of the differential equation solver ODE and has significant innovations added to handle the closed-loop kinematic chains of bipedal movements. Such chains and the contact constraints they introduce have proven difficult to model. Our methodology integrates two key innovations. The first is to allow the kinematic makers of a motion capture system to be modeled as enormous point masses. The result is to stabilize

the integration of the underlying dynamic equations. The second is to allow the reduction of contact constraints into stiff springs, which has the result of allowing the incorporation of external forces and points of contact. The overall result is that the system can reliably follow any kinematic plan.

Chapter 3

Virtual Tracing Experiment¹

Although everyday motor coordination can be taken for granted, to achieve it, the human movement system must control approximately six hundred muscles acting through about three hundred joints. This overall complexity has tended to limit the formal study of movement to relatively constrained or repetitive situations like walking, cycling, and reaching, which can be analyzed with approximate tractable models that have much lower degrees of freedom. Such movements show marked regularities across subjects that can be interpreted in terms of relating the dynamics of the movement to its goals. However, arbitrary large-scale movements have been much less studied. For example, do the regularities in familiar movements extend to arbitrary situations, or do they vary significantly among different individuals?

One difficulty in addressing this question is that there have been no obvious ways to compare different whole-body human postures in 3 dimension

¹The work described in this chapter was published in iScience by Liu et al [62]. Leif Johnson, Oran Zohar, and I developed the experiment protocol. The human movement data were collected and analyzed by me, with much help from Dana Ballard.

coordinates. This chapter describes the method we developed to solve this problem. First, we developed a virtual tracing experiment to gather the motion capture data of natural human tracing postures. Participants traced extended closed curves with their right index finger to complete the tracing tasks at a controlled speed in a three-dimensional virtual environment. Then we analyzed posture variability when individuals traced predetermined paths on a large scale that required them to make whole-body movements, including steps.

The principal result is that although they were not instructed as to the details of their movement, subjects exhibited remarkably similar posture sequences throughout the movements and common modulations in these sequences. Since there is a close relationship between the body’s kinematics and its dynamical forces, the extraordinary similarities in posture control suggest that this result may be interpreted in terms of similar energetic cost principles. The results of this chapter show that this perspective turns out to be the case and leads to a general understanding of large-scale movement control as trying to optimize movements’ energetic cost, which will be described in detail in the next chapter.

3.1 Methods

The whole-body tracing experiment was designed to elicit natural movements under common goals. Subjects wore a virtual-reality helmet, Oculus Rift², to see a virtual three-dimensional interior room with a dojo backdrop via stereo video. They were required to trace a series of paths positioned at fixed locations in the virtual environment. The movements of their bodies

²Oculus Rift <https://www.oculus.com/rift/>

and variables relevant to the tasks were simultaneously recorded using the PhaseSpace motion capture system³. The WorldViz Vizard software package⁴ both controlled the experimental protocol and the recording of the motion capture data.

3.1.1 Tracing protocol

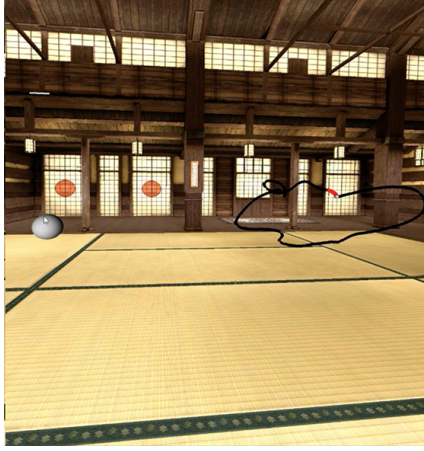
At the beginning of the trial, the subject had the suit markers checked to see that they were in appropriate positions and adjusted the Oculus Head-mounted display, which rendered the virtual world.

To allow for choice in initial tracing postures, a subject initially stood at a position marked by a large white sphere one meter away from the virtual three-dimensional closed curve suspended in space (see Figure 3.1 (a)). From this position, they could freely observe the path and the location of a target sphere on the curve. Subjects were instructed to use their dominant hand.

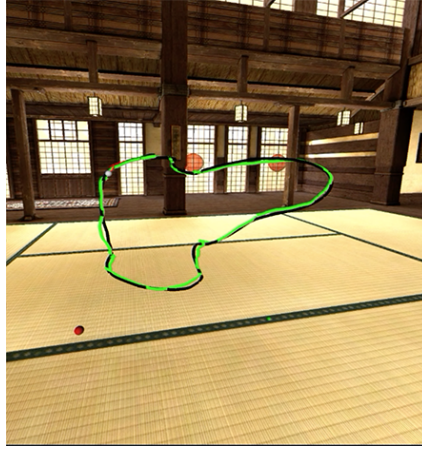
To start the tracing phase, software played a bell sound, and then a large white target sphere was rendered on the path at a specific starting position. The subject was instructed to stand next to this sphere. Once the subject's index finger, represented by a green sphere, intersected the target sphere moved off along the curve and the tracing portion of the trial began. The target sphere would traverse the path and the subject traced the path by keeping their index finger as close as possible to the target sphere. During the trial, the subject received both visual and auditory feedback indicating target proximity. When the target sphere was intersected with by their index finger, it changed its color from white to blue, otherwise, it remained white. The software played

³PhaseSpace <http://www.phasespace.com/>

⁴WorldViz Vizard <http://worldviz.com/products/vizard>



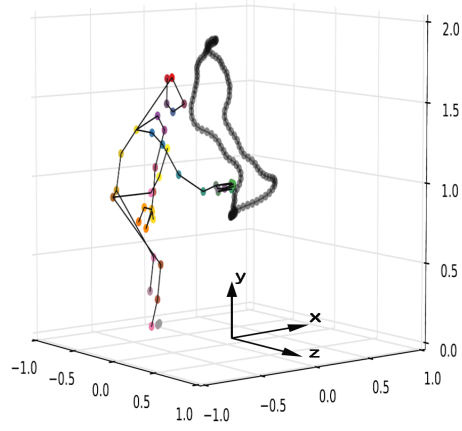
(a) Before tracing



(b) After tracing



(c) A subject doing the tracing task



(d) The skeleton plot of the subject

Figure 3.1: the virtual environment setup. (a) shows a full view of a path, denoted by a black curve, and the starting position, denoted by a large white sphere. The small white sphere on the curve at the end of a red segment is the tracing target sphere. (b) depicts the scene when a trial is finished. The green curve is the actual tracing trajectory generated by a subject. (c) illustrates a subject in the act of tracing a curve in the laboratory's motion capture 2 x 2 x 2 meter volume. and (d) shows the lab coordinate system. The scale on the graph is in meters. The the subject's skeleton and the traced path in the 3D space are plotted. The color dots correspond to a subset of the fifty active-pulse LED markers on the suit and the virtual-reality helmet. Related to Figure 2.

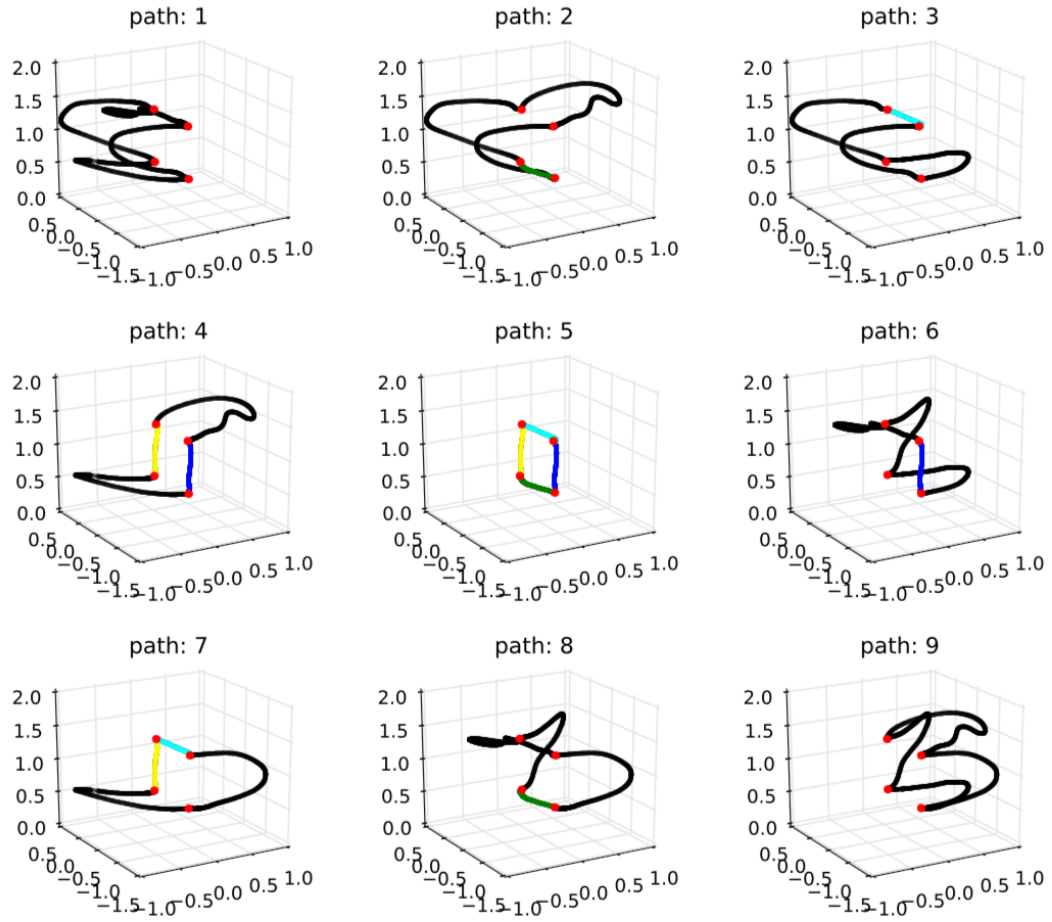


Figure 3.2: The nine 3-dimensional paths in the virtual environment that were used in the experiment. For reference, colors denote common segments and points. For the subjects, the curves were all rendered in black, The scale is in meters. Related to Figure 1.

a sound of “click” when the target sphere changed color. The trial ended when the target sphere returned to its original starting position. At that moment, the actual tracing trajectory generated by the subject was shown so they could evaluate their performance. Immediately afterward they returned to the starting position to start the next trial (see Figure 3.1 (b)).

The experiment was organized in a series of blocks, each of which consisted of nine curves, presented individually in a predefined but randomly generated order. A demo of the tracing task is posted online⁵.

Path Design The curves to be traced were chosen to go through a common region of space, shown in Figure 3.2. The paths were spread out in a volume of space approximately $2 \times 2 \times 2$ meters, large enough for that subjects to plan and execute sequences of full-body movements, including walking, crouching, and tracing, to complete the task.

Each curve went through four fixed points in the virtual 3D space chosen to constrain the curves to occupy. These points were located at $(-1.2, 1.50, -0.31)$, $(-0.60, 1.50, -0.31)$, $(-0.60, 0.75, -0.31)$, $(-1.2, 0.75, -0.31)$ meters respectively, with the reference frame shown in Figure 3.1(d). This design assured that the tracing finger went through at least two sets of two points in space at the same height during each curve trace, providing a special set of references wherein the postures could be compared.

Target Speed The tracing white sphere’s speed was 0.25 meters/sec, which was selected during practice trials to be a compromise between a desire to make the task comfortable to perform and at the same time sufficiently challenging

⁵A tracing task demo: <https://youtu.be/nnXZaj8Zpss>

to be interesting.

3.1.2 Subjects

Eighteen healthy and right-handed subjects were recruited from a pool of undergraduate and graduate students from The University of Texas at Austin. All subjects completed five blocks (5 traces per path x 9 paths for 45 trials total) of the task plus a practice tracing. Each trial normally took about 30 seconds to complete, thus a single subject spent about 45-60 minutes on completing the experiment.

3.1.3 Motion capture

Movements were recorded using a 16-camera PhaseSpace motion capture system, which measured the 3-dimensional locations of active-pulse LED markers with 100Hz and approximately 1-millimeter absolute positional errors. The motion-capture suit was equipped with 50 markers, which are consistently attached to specific body parts (see Figure 3.2). The locations of the attached markers over time result in an array $P \in R^{T \times 3M}$, where T represents the time frames, and M represents the number of markers. A complete data set for each trace comprises all the information between the start and end of each tracing portion (i.e., the moments of contact with the target sphere and the target sphere back to its original position in the trial). It includes both the 3-dimensional locations of subjects' LED makers and the target sphere, resulting in approximately 800-1200 video-rate frames of motion capture data per trial (see Figure 3.1 (c and d)).



Figure 3.3: PhaseSpace suit with 50 active-pulse LED markers. The numbers next to the LED markers are the marker indexes used for recording the motion capture data.

Data post-processing For some frames, the motion capture system is unable to determine the 3-dimensional location of some markers. Thus raw motion capture data usually contains some segments of signal loss (dropouts). Dropouts are relatively infrequent in practice but can occur over significant temporal intervals, making linear interpolation a poor choice for restoring the raw motion capture data. In this experiment, a trajectory-based singular value threshold method was implemented to reconstruct missing marker data with a minimal impact on its statistical structure.

In addition to the data interpolation process, if a participant did not trace the curve successfully, e.g., their index fingers were too far behind the white sphere tracing points at a specific frame, we would consider the tracing task at this frame failed, and the corresponding data would be discarded.

3.1.4 Data analysis overview

The centerpiece of the analysis depends critically on the definition of a posture. At each frame, posture is defined as a vector of the positions of each of M markers ($M = 50$ in our experiment). The posture p at a frame is a 3m-dimensional column vector presenting the maker positions of the i *th* participant, thus

$$p = [m_1, m_2, \dots, m_M] \quad (3.1)$$

where $m_i = (x_i, y_i, z_i)$ represents the position of the i *th* marker at a frame and $i = 1, 2, \dots, M$.

The analysis is naturally organized into three separate stages. Initially, we analyze the subjects' choice of staring postures, which group naturally into small sets. The studies of tracing use exemplars chosen from the same group.

Once the starting postures are determined, the next step is to analyze the tracing process. To measure the similarity of posture sequences across subjects, we randomly choose one representative trace from all five repeated traces of each subject.

Finally, when measuring correlations in subjects' posture sequence variability, we use all of the five repeated trials for each individual. Markers are correlated with each other by virtue of being on the same motion capture suit, but the analysis of posture differences uses marker data from different trials that are obviously independent.

3.1.5 Starting posture classification

At the beginning of each trial, the participants could see the initial location of the target sphere on the curve but were not given any instructions to approach each curve and choose a starting posture. The initial expectation was that they all might choose a common starting posture but instead, a small number of such postures were preferred. These choices were important as the traces were very sensitive to the choice of starting postures. Using the example of the square curve (path 5), if starting from one side, the resulting trace will be very different from the one that would result from starting facing the other side. However, the traces from a given choice would all be similar.

The different starting points make their resultant sets of traces incomparable with each other and as a result we developed a method of identifying the clusters of subjects who had chosen similar starts. Principle Component Analysis was used to get the compressed features of all postures at first frame, and then Affinity Propagation clustering was used to classify them into differ-

ent categories. The details of the process are summarized as follows:

1. Define the initial postures at frame 0 of n participants as $P_0 = [p_1, p_2, \dots, p_R]$, where R is the number of postures at frame 0.
2. Apply principal component analysis to all the initial postures that are defined by the matrix P_0 .
3. Keep the leading r principal eigenvectors in order to construct a $3m \times r$ matrix A_r , where m is the total number of markers. In this way, the initial postures are projected from a high-dimensional space (3m-dimension) into a low-dimensional space (r-dimension) and defined as A_r .
4. Apply Affinity Propagation on the matrix A_r in order to classify the initial postures into different categories.

Principle Component Analysis and Affinity Propagation clustering were achieved by using Python machine *scikit-learn* learning package ⁶.

3.1.6 Tracing standard deviation calculation

It will be helpful to start with an easy hypothetical case of n samples of just one component of one marker. For this case:

$$\bar{x} = \frac{1}{n} \sum (x_i)$$

and

⁶scikit-learn <http://scikit-learn.org>

$$\sigma_x = \sqrt{\frac{1}{n} \sum (x_i - \bar{x})^2}$$

Where x_i is a value, $i = 1...n$, and \bar{x} is the mean of $\{x_i\}$.

To test the uniqueness of the posture with respect to other postures at this point one could sample the same marker at another point in time from the trace and ask if that point is significantly improbable given the \bar{x}, σ_x just computed. Depending on the outcome of this test one could report a confidence level that the two locations are similar or different. However one can do much better than this by including all the three of the coordinates, and much better still by including all fifty markers. As will be shown, at the marker level, the distinctiveness of locations are extremely significant, but the calculations are straightforward generalizations of the scalar case.

First, let's include the other coordinates. Since a marker position, m_i , which is a vector of three values, x_i is changed to m_i , the difference between x_i and \bar{x} is changed to the Euclidean distance between m_i and \bar{m} . Therefore, we calculated the standard deviation of marker positions as:

$$\begin{aligned} \sigma_m &= \sqrt{\frac{1}{n} \sum (m - \bar{m})^2} \\ &= \sqrt{\frac{1}{n} \sum [(x_i - \bar{x})^2 + (y_i - \bar{y})^2 + (z_i - \bar{z})^2]} \\ &= \sqrt{\sigma_x^2 + \sigma_y^2 + \sigma_z^2} \end{aligned} \tag{3.2}$$

and the mean as

$$\overline{m} = (\overline{x}, \overline{y}, \overline{z})$$

Now let's handle the markers. To completely specify a marker, requires three indices, one to specify the individual marker, one to specify the trial, and one to specify the time frame of the trace. Thus we use $m(i, j, k)$ where $i = 1, \dots, M$, $j = 1, \dots, R$, and $k = 1, \dots, T$. In analyzing the repeats of a single subject, R is the number of repeats. In analyzing the case of one trace per subject, R indicates the number of subjects. T is the number of frames. To be economical, we will suppress these the time index when a particular frame is understood.

To proceed, given some postures at a certain frame while tracing a curve, let: the *average marker* $\overline{m}(i)$ represent the average position of the i th marker;

$$\overline{m}(i) = \frac{1}{R} \sum_{j=1}^R \Delta m(i, j).$$

and a set of average markers constitute an *average posture*. The average marker is used to compute a *relative marker using*

$$\Delta m(i, j) = m(i, j) - \overline{m}(i), \quad (3.3)$$

which defines the relative value of the of the i th marker in the j th trace. A set of relative markers constitutes a *relative posture*.

Assume a curve was traced R times, then the standard deviation in position of the relative marker, Δm at a certain frame k , $\sigma_{\Delta m}$, can be calculated

as:

$$\sigma_{\Delta m}(i) = \sqrt{\frac{1}{R} \sum_{j=1}^R \Delta m(i, j)^2} \quad (3.4)$$

and the relative marker mean as

$$\overline{\Delta m}(i) = \frac{1}{R} \sum_{j=1}^R \Delta m(i, j). \quad (3.5)$$

3.1.7 Tracing Posture matching

Since the approach was conducted in world coordinates, we first translated each posture before matching such that its right index finger was overlapped with that of the mean posture. In this way, the distortion generated by matched postures with location differences was minimized. A final detail is that we chose one out of every twenty frames along the curve as a specific frame and examined all the postures at each specific frame by calculating the mean and the standard deviation of the Euclidean distance.

The final component of the analysis is to develop a method for comparing postures from different stages in the tracing. The *posture matching* described in the following was specifically developed to verify the similarity of posture sequences (for subjects who started from the same cluster of initial tracing posture). This scheme matched a posture at a certain frame against mean postures along the path, and then checked if the posture was the best matching with the mean posture at the same frame. Specifically, we put the postures at each specific frame in a single data set and computed the mean postures of each data set. For checking a posture at a specific frame, we computed the Euclidean distance between this posture and each of the mean

postures of all specific frames in order to see whether or not the Euclidean distance between this posture and the mean posture of the same specific frame are minimum.

It is important to note that this methodology does not depend on the sums or differences being interpretable as a posture. The metrics just have to be good enough for our similarity comparisons, which are relative. The intent is to show that the distribution of mean posture matches, using the metric, is quite contained at a point and very different when compared to distal points on the traced curve.

Assume a path with N frames was traced R times, then the mean posture at a particular frame k_a can be calculated as:

$$\overline{\Delta m}(i, k_a) = \frac{1}{R} \sum_{j=1}^R \Delta m(i, j, k_a) \quad (3.6)$$

From Eq. 3.6, the match value Q_a at k_a can be calculated as

$$Q_a = \sqrt{\sum_{i=1}^M ||\overline{\Delta m}(i, k_a)||^2} \quad (3.7)$$

Now for the match at a separate time frame k_b . The data at frame k_a needs to be compared to the average at this different time. Thus the data from k_a uses the average at k_b :

$$\Delta m(i, j, k_b) = m(i, j, k_a) - \bar{m}(i, j, k_b)$$

So that the match value at k_b can be calculated as

$$Q_b = \sqrt{\frac{1}{M} \sum_{j=1}^R \|\Delta m(i, k_b)\|^2} \quad (3.8)$$

When we compare the two frames k_a and k_b they are always a multiple of ten frames apart. With this constraint Q_a turns out to be very significantly different from Q_b .

3.2 Results

The main result is that although the locations tracing data exhibits posture variations, both in repeated of a single subject and in trials by different subjects, the average postures show marked regularities in six aspects of the data that was subject to analysis:

1. The initial poses chosen by subjects grouped into a small set of preferred postures (See section 3.2.1 and Figure 3.4);
2. Stances in the specific points of tracing a square curve showed very small standard ellipsoids of all markers measured (See section 3.2.2 and Figure 3.5);
3. Analysis of data from throughout the traced curve showed that the average posture at every point on the curve was unique with respect of the averages at other points (See section 3.2.2, Figure 3.6 and Figure 3.7) ;
4. A t-test between a proximal relative posture and distal relative posture showed that the difference is significant at the 0.0001 level (See See section 3.2.2 and Figure 3.8).

5. The variance of the markers scales according to their task relevance (See section 3.2.3 and Figure 3.9);
6. The variances in the subjects' postures were correlated. If at a point on the curve the variance of a trace calculated from a subject was relatively large, the average of the variance of all the repeated trials from all subjects would be relatively large also (See section 3.2.3 and Figure 3.10).

3.2.1 Initial posture choices

Although the subjects could have chosen very different starting postures, they preferred one of a small number of specific groups. Small distributions in starting position and orientation can be explained if, at beginning of a trial, subjects roughly planned the sequences of tracing motions by visually tracking the path and its position of the target sphere en route. When they advanced to make contact with the target sphere, they placed their right index finger in a particular location on the path. As there were only so many ways for subjects to choose a comfortable place to start tracing, together with the constraint of the kinematic structure of their skeleton, the foot positions and body facing directions can be expected to show small distributions.

The postures at the first frame on each curve were taken as the participants' initial postures. Figure 3.4 illustrates the results of segmenting the initial postures into small groups. It showed that the paths with more distinct lobes had more clusters of distinct starting postures. Furthermore, it is obvious that the initial postures classification is mainly due to the standing locations, which roughly means participants' postures can be considered as exhibiting some similarity if they are standing in the same area and their fingers

are attaching to the same point on the curve.

classification proportion				
	posture 1	posture 2	posture 3	posture 4
path1	43	29	20	8
path2	69	21	10	-
path3	31	26	21	22
path4	70	20	10	-
path5	66	34	-	-
path6	46	27	15	12
path7	73	27	-	-
path8	43	24	20	13
path9	32	28	24	16

Table 3.1: The proportion of individual subjects in each cluster as a percentage. For example, for tracing path 5, the square curve, 66 % of the subjects chose to face the curve from one side and 34 % from the other. Related to Figure 3.4.

3.2.2 Posture matching during tracing

Once tracing has started, the postures of subjects can be compared at any point along the curve. Using one trace per participant, we calculated the three dimensional standard deviation ellipsoid for each marker location. For example, tracing data for path 5 can be seen in Fig. 3.5 (a), which illustrates all skeletons when subjects' index fingers contacted two corners while tracing square path. Two common postures appeared corresponding to the two initial postures on different sides of the square curve (path 5) shown in Figure 3.4. The corresponding mean position of each marker and the standard deviation of marker positions are shown in Figure 3.5 (b). The ellipsoids' different colors represent different markers on the PhaseSpace suit. This comparison clearly indicates that subjects used similar postures at corners during tracing square

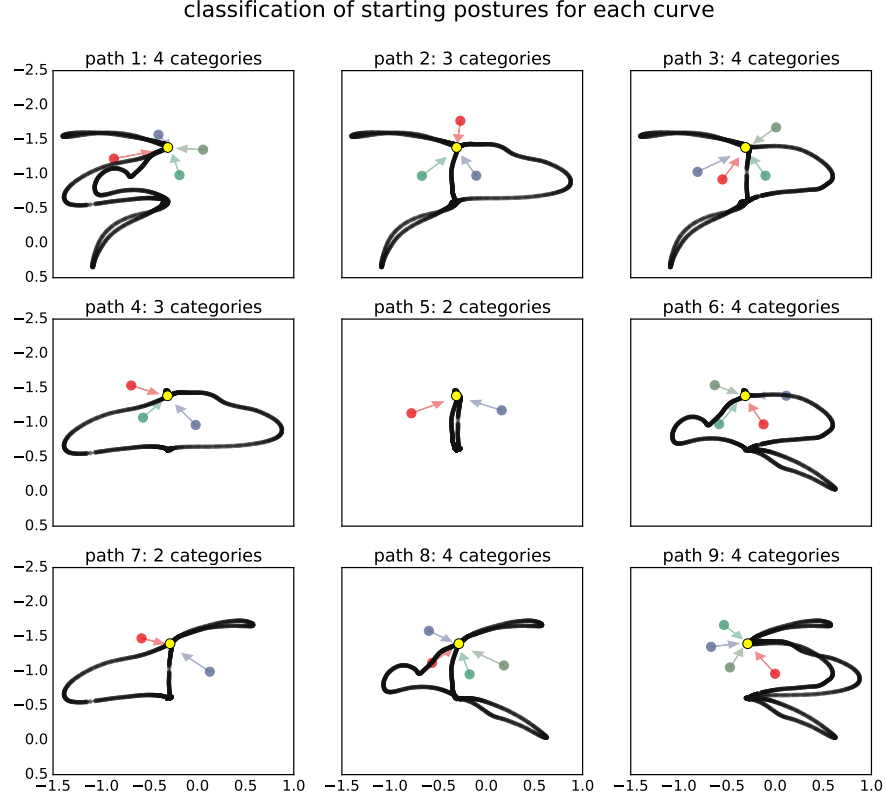


Figure 3.4: Classifications of starting postures. The view is from the top of 3D space and the black curves are the nine paths used in our experiment. The yellow dot on each curve indicates the starting position of the target sphere. The dots around each curve represent the average starting locations of head markers of the subjects while tracing this curve. The direction of each arrow is the direction from the head marker to the right index finger marker for each subject. Colors denote the different clusters classifications. For example, in Path 5, the square curve, only two starting postures were used. The distribution of the chosen initial postures for each path was shown in Table 3.2.1. For curves 2,4,5 and 7, one posture is overwhelmingly preferred over the others. The 3-dimension view of all nine curves were shown in 3.2

path, a result that generalizes across positions and curves, as will be shown.

In order to more rigorously compare postures at all points along a path, the more sophisticated posture matching method of comparison described in the tracing posture matching section (see Transparent Methods) was used. First, the mean posture of overall participants at each frame along the curve is computed by averaging the data set using one trace from each subject. Thus each frame has an associated mean posture. Next, each posture at a *checking frame* is matched against the mean postures for all the frames along the curve.

For instance, taking frame 300 as the *checking frame*, each of the postures at frame 300 was matched to all the mean postures in turn, and then the mean and the standard deviation of all matches at each frame were calculated. The results of such comparison are shown in Figure 3.6. The red dash line illustrates the locus mean of the match and the vertical bar in blue demonstrates the standard deviation. The match at frame 300 uses Equation 7 and all other matches use Equation 8 (see Transparent Methods).

As shown, the best match occurs at the frame 300, which means the best match occurs at the frame where the postures are taken from and its match is more inexact at other frames. It might be argued that the matches are different owing to the effect of the height of the curves above ground level. Different heights can make a difference, but there are large regions at the same heights with different matches. Figure 3.6 shows this by color coding the dots according to the heights of the curve points at the corresponding frames, with blue representing the lowest height and red the highest. It is readily seen that a large swath of points on the curve between frames 200 and 500 have very similar heights but their match costs are quite different. This format shows off the result that although the matches may have considerable extents, their

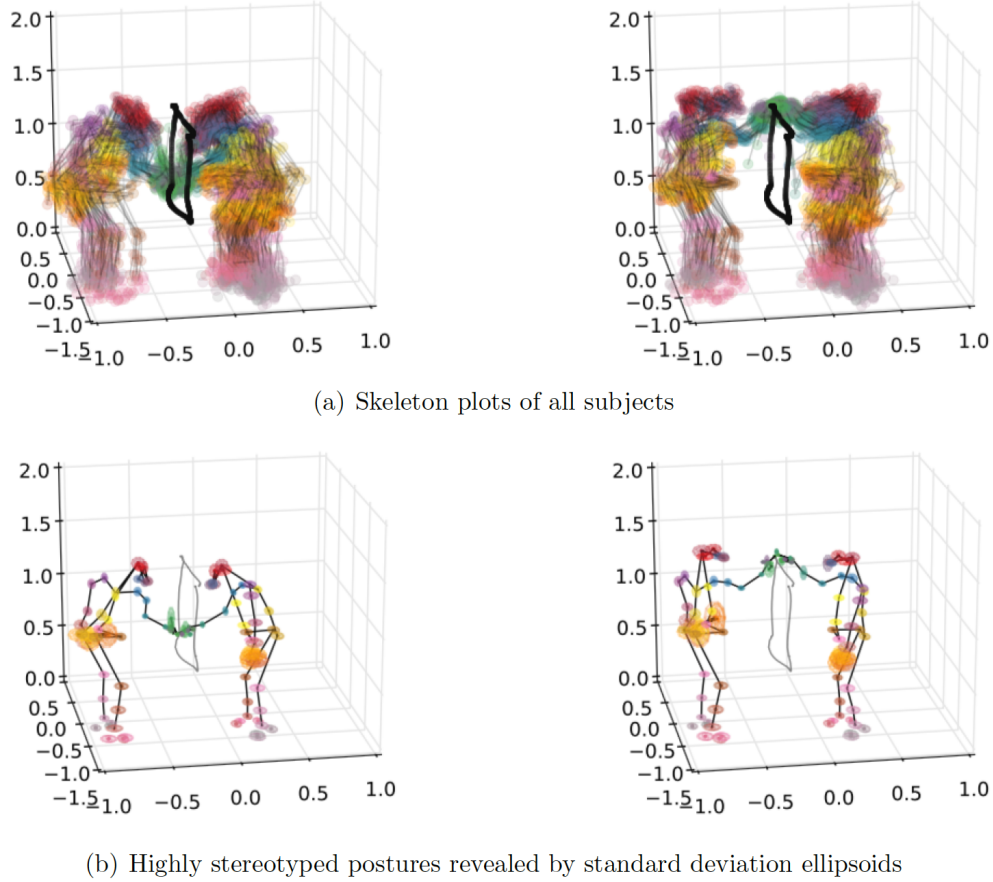


Figure 3.5: Tracing data analysis for path5. (a) the skeleton clouds of 90 trials (18 subjects each with 5 repeats) when subjects' right index fingers reaching the two corners of the square path. (b) highly stereotyped postures generated by 90 trials. The spheres with different colors represent different markers. The central location and the size of a sphere indicate the mean position and the standard deviations of the corresponding marker, respectively. Related to Figure 3.1 and Figure 3.3.

means are almost always very distinct.

This method can be extended for each point on every curve. Figure 3.7 summarizes the postures at each checking frame were the best matching with the mean posture at the same frame. For instance, as for path 2, the postures at frame 250 were best matched with the mean posture at frame 250. The plotted dots almost formed a line with the slope of 1, which is desired. Furthermore, the results for all nine curves show that the postures at each point are almost all unique.

The few outliers were generated because participants moved back to the initial positions at the end of tracing, which results in some similar postures at the very beginning and the very end of tracing. For example, the outlier of path 8 in Figure 3.7 implies the postures at frame 20 are best matching with the mean posture at frame 1020. The study focused the results of the posture sequences during the tracing, which excluded the first 50 frames and last 50 frames. In this region, regardless of the subjects, the best match occurs at the appropriate location along the curve.

As mentioned above, one obvious reason to expect postures to be different is that the curves have many different heights that the tracing finger has to follow. However, there are many points along the curve with identical heights, including Special cases are the the four fixed points on each curve that were specifically chosen to have the same heights. The heights of the first two fixed points are 1.5m and the heights of the remaining ones are 0.75m. These two pairs are highlighted in red and yellow on Figure 3.7, and indicates distinct matches, even when the tracing figure heights are identical.

One final issue concerns the reproducibility of the method. How robust is the margin separating matches at correct positions and matches at arbi-

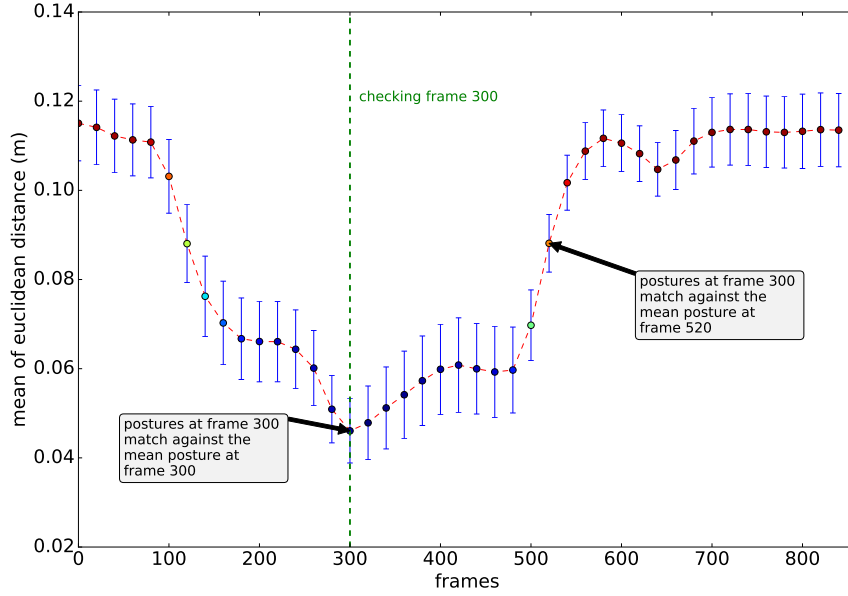


Figure 3.6: Posture matching results of square tracing at frame 300. At the outset, for each frame, the mean posture at that frame is computed by averaging the postures at that frame. Next, the relative postures for frame 300 are compared to relative postures other frames selected at 20 frame intervals. The colored dot represents the mean of euclidean distances between checking relative postures at frame 300 and relative postures at other frames. The blue bar indicates the corresponding standard deviation. The colors of dots indicate the relative height from the laboratory floor with blue being the lowest and red the highest. In this example, the relative postures at frame 300 are the best match. The fact that all the other matches have higher distance measures indicates that the chosen match point is dissimilar to all the all the other points on the traced curve.

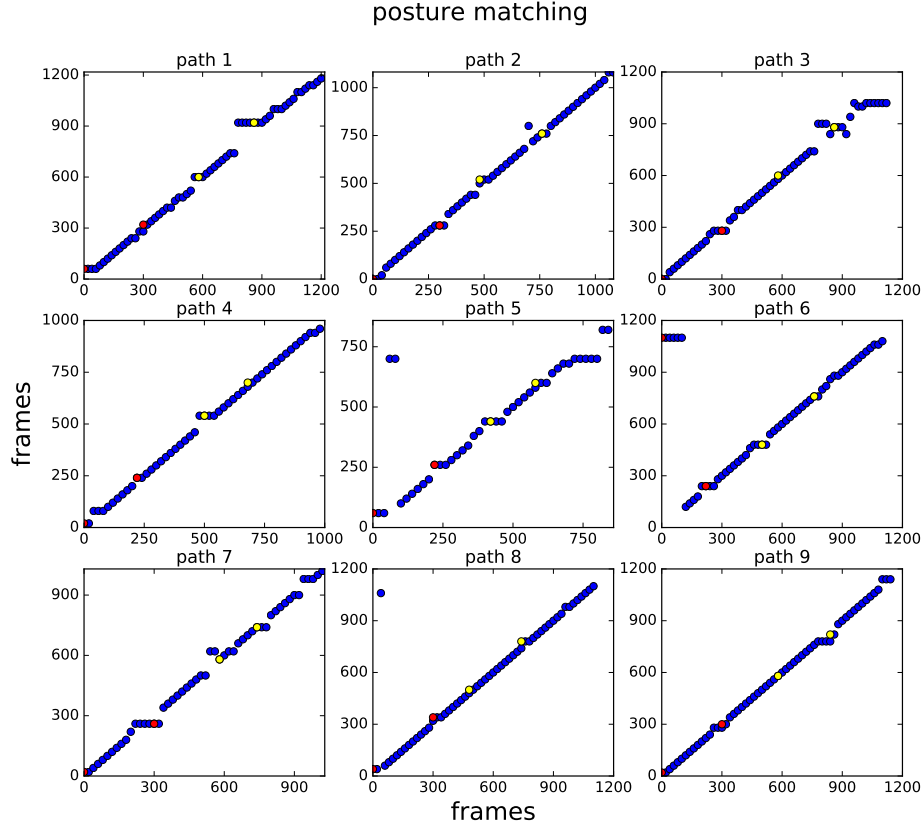


Figure 3.7: Posture matching results for nine curves. The horizontal axis represents the checking frames, which were taken once every 20 frames. The vertical axis represents the frames of relative postures that were best matching with the postures at checking frames. Two red points and two yellow points indicate the matching results of the four fixed points in the virtual 3D. The two colors signify that these points were constrained to be at the same height. Naturally many subsets of blue points may have the same height, but this property was not checked. The net result is that almost every relative posture at each frame for each curve is unique. Given at least 50 samples per path and 9 paths, a total of more than 22,000 comparisons were made. This calculation makes the result that almost of the 450 perfect matches are seen, even given that in many of the match pairings the tracing finger is at the same vertical height, remarkable.

trary mismatched positions? To explore this issue we averaged all matches at correct positions for all nine curves and compared this distributions to the corresponding calculation for incorrect matches. The result is shown in Fig. 3.8, which shows that regardless of the curve, the posture at any point on a curve is easily distinguished from the postures at any other points on the curve. To demonstrate this result we used equal numbers of samples of the Q_a and Q_b calculated using Equation 7 and Equation 8 respectively (see Transparent Methods). The huge number of samples, together with the non-overlapping variances resulted t-test level of significance greater than the 0.0001 level.

3.2.3 Marker variations during tracing

In concert with earlier observations [102, 55], the standard deviation of the task-irrelevant end-effectors was larger than that of task-relevant end-effectors, even when measured across subjects with different skeleton sizes. To show this relationship, we computed marker standard deviations using one trace per subject at four different distances from the tracing locus. Figure 3.9 shows the standard deviation of the task-relevant markers and task-irrelevant markers, across subjects with initial positions from the same cluster. As the most task-relevant end-effector, the right index finger had the smallest standard deviation, while as the most task-irrelevant end effector, the left index finger had the largest. The right shoulder marker and head marker, which are intermediate task-relevant markers, had moderate standard deviations along the entire tracing.

Having shown distinctive patterns in the average of the variance data for all subjects leaves open the question the issue of individual differences.

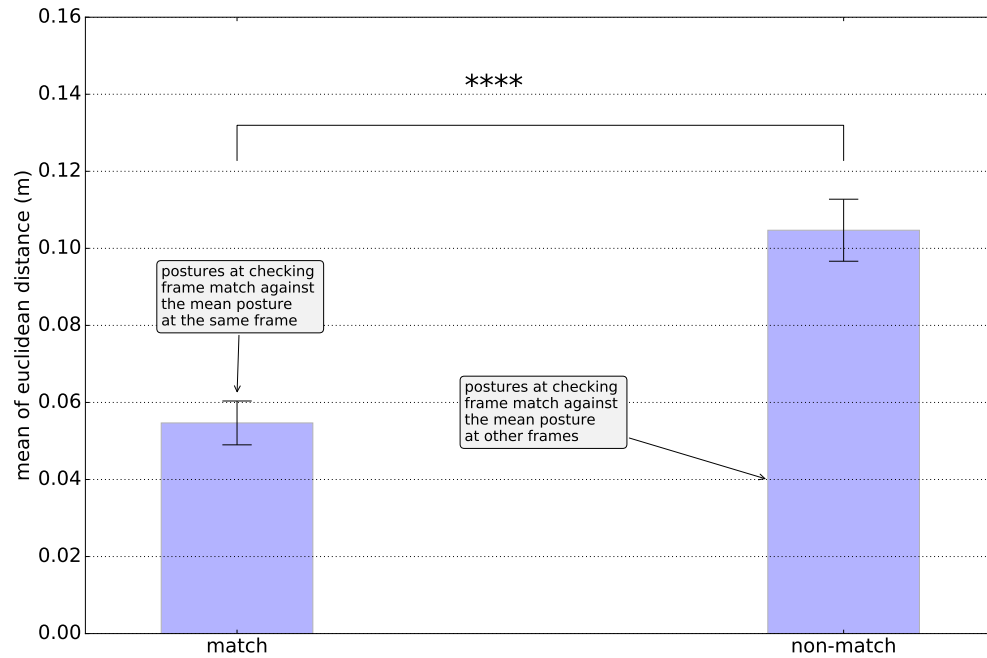


Figure 3.8: The match column compares matches of postures at their original location to the mean posture at that location. The non-match column compares matches of postures to matches to the other mean postures on the curves. All nine curves are used in this comparison. This difference is obviously hugely significant, implying that the methodology is highly reproducible as postures that are at distal sites on the traced curve are very dissimilar. The t-test of this data shows that the difference is significant at the 0.0001 level.

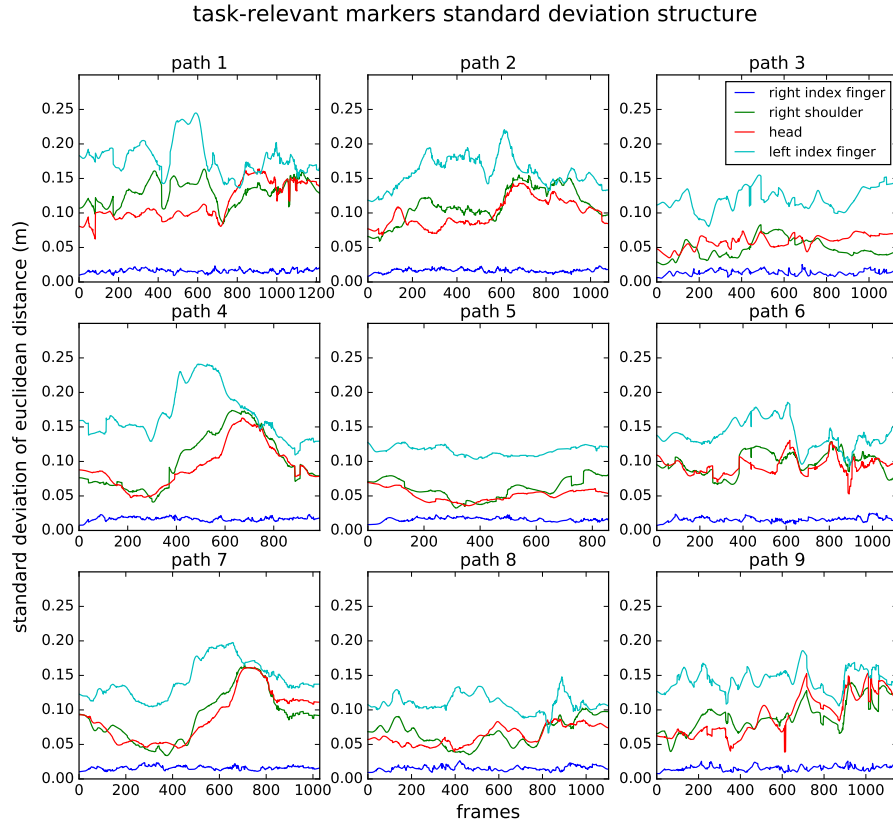


Figure 3.9: Comparison of the standard deviation of marker positions. At each frame, the mean position of a marker was first computed, then we calculated the Euclidean distances between each of the positions of the marker and its mean position, finally, the standard deviation of the positions of the marker was computed. The corresponding average standard deviations averaged over all the frames of each curve are shown in Table 3.2.3.

average standard deviation (cm)				
	right finger	head	right shoulder	left finger
path1	2	12	12	18
path2	2	11	9	16
path3	1	5	6	12
path4	2	10	9	17
path5	2	6	5	12
path6	2	10	9	14
path7	2	9	9	14
path8	2	7	6	11
path9	2	9	9	14

Table 3.2: The average standard deviation of the marker positions. Related to Figure 3.9

Surprisingly it turns out that individual subjects all modulate their variations in the same way. To probe this relationship, we computed the standard deviations at small intervals at each frame of the five repeated trials for each subject using Equation 4 (see Transparent Methods) and sorted the intervals by standard deviation magnitude. Next, we computed the average of the standard deviations for each of the subjects. These calculations produced a series of tracing standard deviations for each subject as well as the standard deviation average cross all subjects. This allowed the correlation of the standard deviation of each subject with the average of that of the group. A representative result is shown for the shoulder marker in Fig. 3.10, which shows the mean and standard deviations of the tracing data sorted for increasing standard deviations. The important conclusion from this figure is that although the local variance in tracing markers varies from point to point, it varies in a correlated way. If the variance is high at a point in tracing for one subject, it will also be relatively high for the average. The inset table in the figure shows the complete set of correlations for the four markers analyzed for each of the nine

curves. The result is each of the 36 measurements is significantly positively correlated, with R values ranging from 0.40 to 0.87. and an average correlation 0.69. The implication is that subjects modulate their variance during tracing transit in the same way.

R values for the four markers				
	right finger	head	right shoulder	left finger
path1	0.87	0.4	0.5	0.53
path2	0.77	0.76	0.77	0.83
path3	0.76	0.57	0.75	0.48
path4	0.74	0.63	0.68	0.67
path5	0.76	0.62	0.49	0.67
path6	0.81	0.71	0.82	0.66
path7	0.7	0.8	0.75	0.64
path8	0.85	0.63	0.52	0.66
path9	0.8	0.64	0.68	0.8

Table 3.3: All the R values for the four markers computed for all nine curves show positive correlations. Related to Figure 3.10

3.3 Discussion

The data analyses showed for large-scale movements of a constrained task, the observed movement kinematics are very similar across subjects, both in terms of mean posture values and their variances. At each point on any of the tested curves, the average posture is easily distinguished from all the other average postures by a metric that quantitatively compares posture differences.

While there are local variations at points on the body, these turn out to be co-modulated also. When the average local standard deviation for all the traces increases, the standard deviation of the individual traces increases in a correlated way. This correlation may be a consequence of constraining

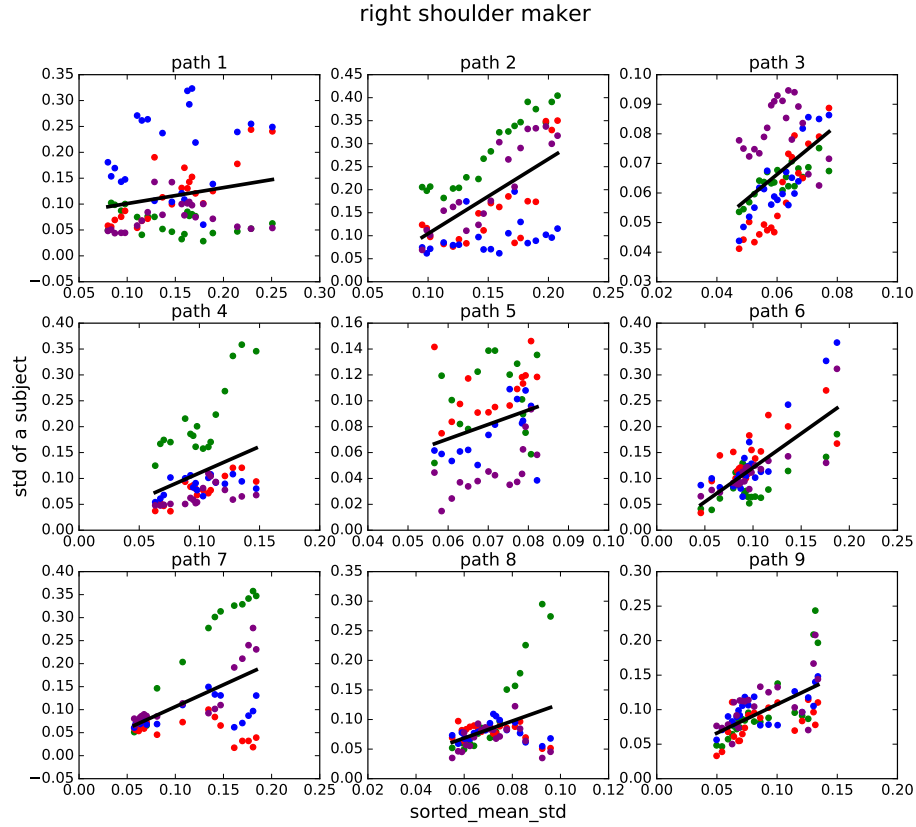


Figure 3.10: The standard deviations in repeated traces for four randomly chosen subjects are compared to the average. To do this, for each ten frame interval, the standard deviation of points is computed. Using this data the average standard deviation of this data is computed. Next, the individual variances are correlated with this average. For colors signify four random subjects. The high R values indicate that subjects' variances, which indicates their cocontractions, are co-varying. All the R values for the four markers computed for all nine curves show positive correlations. (See also Table 3.2.3)

the degrees of freedom of the task with muscle cocontraction, but further experiments with electromyography would be needed to settle this definitively.

One possible criticism of the experiment is that its main result might be expected as extensive data shows that movement profiles are almost bell-shaped and there is a clear preference for certain comfortable postures, but those qualitative considerations fall short of accounting for the exactitude of the matches, given the extent of possible variations in the unconstrained nature of the task. Another factor in response is that the tracing target is continually moving at considerable speed, which obviates the use of quasi-static familiar posture segments.

Another potential criticism focuses on the fact that there are many situations where humans have individual differences in their movements. Handwriting is one [95, 86, 53]. However, this case might be accounted for as this situation makes extensive use of motor learning over a long period. Thus humans can be expected to have differences in their local musculature that has trained in an area where variations have small differences in cost. Another possible point of contention is that humans have differences in gait that readily can be distinguished. However, it is the case that such gait differences are small compared to large variations in the postures at different tracing sites seen in our study. Yet another potential confounding issue is that differences in posture used to express emotion are easily detected [83, 100, 69]. The use of posture to express emotion has been given widespread attention, particularly in the graphics community. However, whether postures expressing different emotions could be confused could also benefit from a quantitative study. It could be the case that in expressing motion, humans choose common postures also.

Given that the kinematics exhibited by tracing subjects is so regular, it is impossible to resist reflecting on why it might be so. In other words, why do they use these particular posture sequences? The question of human motion trajectories has been studied for several decades and tackled from two different perspectives. Researchers have for a long time made the distinction between the planning of a movement [37] and its execution [85, 30], thinking that one had to choose between one or the other. However, the tracing data would suggest that these issues can be separated. The tracing task naturally separates planning and execution into separate phases. Subjects behave differently when choosing their starting posture, where different groups make different choices anticipating the whole traverse. Once they have made this choice, they engage in the act of tracing where they all agree on the postures taken.

Therefore, our preferred hypothesis is that at least once the tracing starts, the posture sequences minimized metabolic energy. Our reasoning is driven by the fact that over the very recent past, a number of laboratories have built elaborate models of the human skeleton and its musculature and shown that the joint torques can be recovered by feedforward integration given the kinematics [26, 18]. Thus given such a model, the kinematics is coextensive with the movement cost. Once the kinematics is given the movement cost is available. It should be emphasized that the assertion common kinematics implies common movement cost, is mainly based on recent algebra of Newtonian computer models as well as earlier work on much simpler systems showed the same result [1]. Parenthetically it should be noted that in anthropomorphic robot models of passive walking the kinematics is correlated with the dynamics [16]. Thus while much work has to be done, the result could be suggesting that the subjects are choosing to follow low-cost trajectories.

Although the ability to integrate the dynamics equations given a model puts torques in register with kinematics, the reality of the ubiquitous use of vision in motor control planning allows for giving kinematics a causal status in motor control. This observation also impacts the possibilities for the brain’s representation of movements. Common movement strategies argue the store of movement segments in the motor cortices for online transmission to the spinal cord (as opposed to real-time control). Studies by [15] show clear evidence of motor planning prior to movements. And the cortex is the only place where allocentric coordinates are converted to posture-centric coordinates.

While the kinematics result reinforces the suggestion of a place of prominence in the motor plan, the representation of kinematics cannot simply a stream of coordinates but has to have an associated grammar that breaks up this stream into ‘sentences,’ that reflect changes in set points mainly due to changes in physical contact with the world. An important concept for addressing these issues is that of the ‘uncontrolled manifold,’ [55], which formulates the control described in terms of task-relevant constraints. The idea of the uncontrolled manifold is also very sympathetic to an evolving view of motor representation in motor cortex. The original micro-stimulation experiments elicited localized body movements correlated with the organization of the topography of motor cortical area M1. However, stimulation with increased stimulus magnitude produced whole body movements that could be interpreted as complete task-specific [32] directed towards large-scale goals such as eating and defense. These task-orientated sequences suggest that the motor cortex’s specific representations may include the longer ‘sentences’ of a movement instead of the local responses that were initially used to define the sensory-motor homunculus. Our results have shown that the tracing finger’s

standard deviation was the smallest as expected, but the standard deviations of other components of the body were also affected by the task demands. In contrast, body segments that were less task-critical had larger standard deviations. In particular, the least task-relevant marker on the unused hand had the largest standard deviation. This result resonates with a number of previous results [102, 55], and suggests that the kinematics alone is not enough to code a movement but that it has to be augmented with additional parameters that shape its planned use.

The next step forward in the tracing task would be to attempt to make the connection between the kinematics and energetic cost. Since classical oxygen consumption methods are impractical and closed form analytically methods do not scale up, the full body forward integration approach is rapidly becoming the method of choice since they could compute the torques of participants directly from the motion capture data. Though the measurements of kinematics are not the same as joint torques, which are created by elaborate sequences of muscle contractions, there is considerable evidence showing that they are directly related. They are linked in computational models that can compute joint torques in a complex multi-joint human model [22]. The implication of this recent computational capability is that one can think of kinematics as a motor plan that can be converted into an equivalent torque plan when the movement is executed. Fortunately, our lab developed a 50 degree of freedom dynamic model [18] that can calculate the torques of each joint given the motion capture data. We can create different movement trajectories, such as adding perturbations to the tracing trajectories of each body part, and see if calculated joint torques minimizing posture sequences for the dynamic human model agree with observed tracing posture sequences.

In summary the overall result shows that movements themselves are highly stereotyped. This stereo-typicality takes a special form. While the movements vary, their mean postures across subjects and variations in repeated trials within an individual subject are highly correlated. Thus, given this methodology, the pattern of movements selected by different subjects was essentially the same, both in the average posture sequences and the variation in those sequences.

An important initial choice is the posture. Subjects could choose any starting posture, yet different subjects limited their choices to a small set, suggesting their tracing plan had a discrete number of solutions.

The tracing loci revealed that the standard deviation of task-relevant motion capture markers was observed to be smaller than that of markers that were not relevant to the task. This pattern is consistent with the uncontrolled manifold theory [55] of control in that the distal degrees of freedom must be programmed to orient the tracing finger's axial variance to be minimal.

Finally, the most important result of the experiment is the degree to which similar tracing postures suggest that there may be a principled objective function used by the subjects. While many exigencies could impact any particular movement choice, posture changes that are saved for the long term are likely to be energy efficient. Future experiments will explore various metrics to see if the role of energy can be established definitively. If this turned out to be the case, this factor would impact almost every brain subsystem involved in motor control.

3.4 Limitations of the Study

There are three limitations of the study. First, the age scope of participants is within a limited range. Since the participants are all University students, their ages are between 18-years-old and 28-years-old. The experimental results should apply to other age ranges, but this needs to be tested. Secondly, the movement of the subject is slightly hampered by the experimental system's need for cables. Currently, we have an accompanying person to manage the system's cables. Lastly, the tracing curve occupies 1m x 1m to 2m x 2m space. We would like to test the experimental protocol in a larger workspace that would allow even larger-scale movements.

Chapter 4

Computational Modeling: Human Dynamic Model¹

Improvements in quantitative measurements of human physical activity are proving extraordinarily useful for studying the underlying musculoskeletal system. Likewise, dynamic models of simulating human movements benefit in clinical to analyze and rehabilitate injuries. In addition, they might provide useful constraints for underlying neural circuits as well. This chapter describes a physics-based movement analysis method for analyzing and simulating bipedal humanoid movements. A forty-eight degree of freedom dynamic model of humans² has been developed to report humanoid movements' energetic components. The dynamic model is fast, robust and capable of simulating humanoid movements with high accuracy and computing the joint

¹The work described in this chapter was published as a preprint paper in bioRxiv by Liu et al [61]. Joseph Cooper created the initial protocol of the dynamic model and did some primary validations. I further developed, organized, and tested the model, with much help from Dana Ballard.

²The HDM mode: https://github.com/EmbodiedCognition/HDM_UI

angles/torques during movements.

4.1 Method

The human dynamic model is built for simulating and analyzing humanoid movement. Fig. 4.1 shows a frame from a study of the cost of movements used in a virtual tracing experiment [60]. The model interface³ allows the control of the human model via a multi-purpose graphical interface for analyzing motion capture data gathered through the tasks that happened in the virtual environment. With this tool, it is possible to dynamically map markers to the model, adjust the model size to fit motion data, test various parameters to visualize different effects, and display the results of kinematic and dynamics analysis. Fig 4.2 shows another example: a punch sequence made initially by a human subject and recreated using inverse dynamics by the human dynamic model.

³HDM UI Demo <https://youtu.be/ASs4Wo5PQcM>

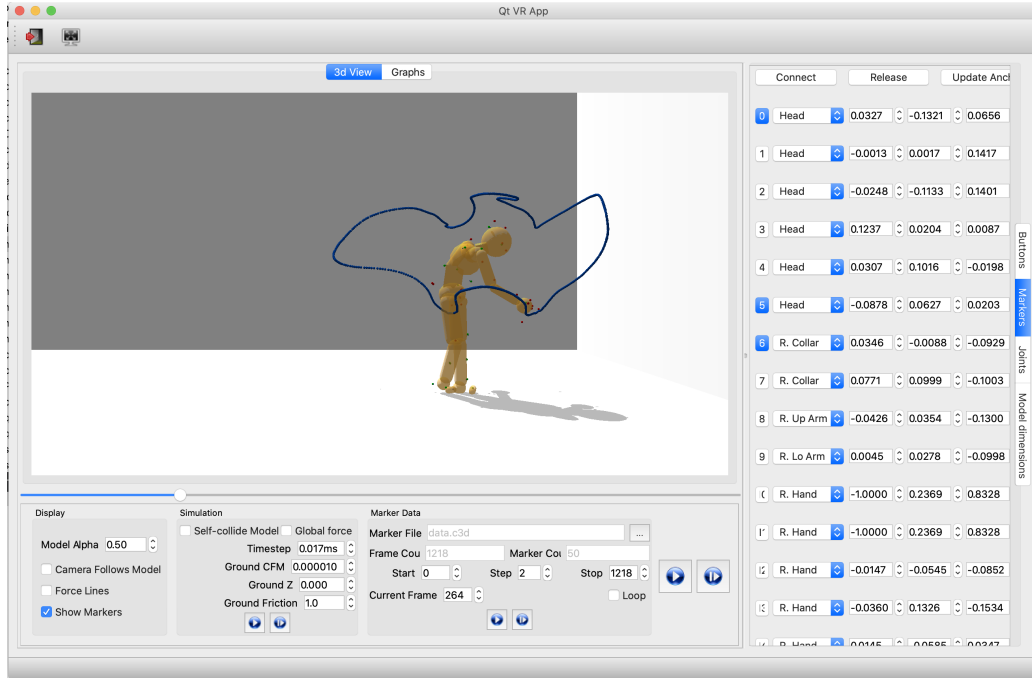


Figure 4.1: The HDM user interface showing a frame from the tracing data analysis. The system supports control and visualizations of model parameters and relevant data so that users can simulate and analyze physically-based movements conveniently. The programmed parameters of the model consist of physical world parameters, joints constraints, and the model’s body-marker relative positions. More details have been described in Chapter 5.

Analysis of human motions utilizing the human dynamic model is implemented in the following five steps:

1. Motion synthesis: it simulates human motion by following the motion capture data [18]
2. Inverse kinematics: it calls the ODE built-in functions to compute the joint angles and joint angular velocities at each frame.

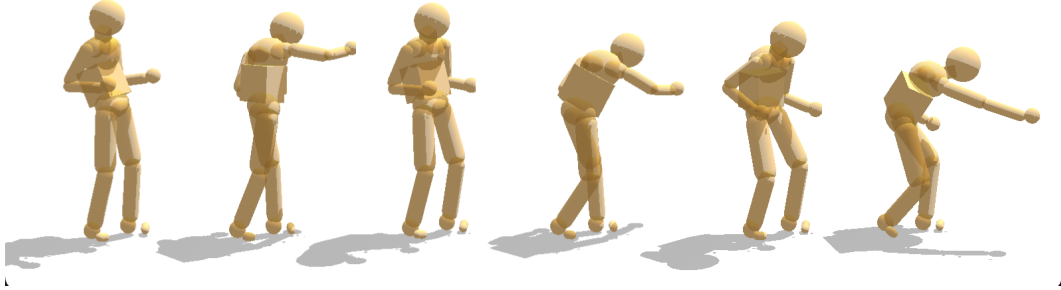


Figure 4.2: Model capability illustration. A punch sequence reproduced using inverse dynamics and the recorded motion capture data from a human subject.

3. Forward kinematics: it simulates human motion based on the computed joint properties. This step is to check the correctness of recovered kinematic properties.
4. Inverse dynamics: it calls the ODE built-in function to compute the required joint torques.
5. Forward dynamics: it simulates human motion based on the computed torques/forces. This step is to check the correctness of recovered dynamic properties.

At each frame, instantaneous power was computed from the product of net joint torque and joint angular velocity. The work performed at each joint were determined by numerically integrating the instantaneous powers over the entire tracing task. In this way, the the energy cost of human motions can be computed given motion capture data. Overall, a novel way to compute the energy cost of human movements has been developed by building a human dynamic model on the top of a physical engine ODE. Its topology was initially

defined by Dr. Cooper [18, 17] and now has been further developed and validated. In the following sections, we focus on describing the primary process of building the human dynamic model in order to make the process easier to understand. More details can be found in the paper [61].

4.1.1 Human Model

The dynamic model capable of representing human movements is built on a physical engine Open Dynamic Engine. Fig. 4.3 shows the model structure consisting of twenty-one separate rigid bodies connected by twenty joints. Each joint connects two body segments with a center of rotation (anchor) that is defined in a local reference coordinate of both body segments. We assigned the body segment dimensions (bone lengths) of the character model some default values according to the average of human skeletons. Still, they should be specified when given specific motion data.

Model degree of freedom details In the Open Dynamic Engine, a joint is a relationship that is enforced between two bodies so that they can only have certain positions and orientations relative to each other. This relationship is called a constraint – the words joint and constraint are often used interchangeably⁴. Fig. 4.4 shows three different constraint types used in our human dynamic model. The hinge joint constrains the hinge’s two bodies to be in the same location and line up along the hinge axle, which was used for connecting the toes and heels in the dynamic model. The universal joint connects two rigid bodies by a cross. It is like a ball and socket joint that constrains an extra degree of rotational freedom. The elbow, wrist, knee, and

⁴ODE joints: http://www.ode.org/ode-latest-userguide.html#sec_3_5_0

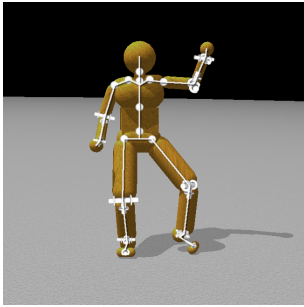
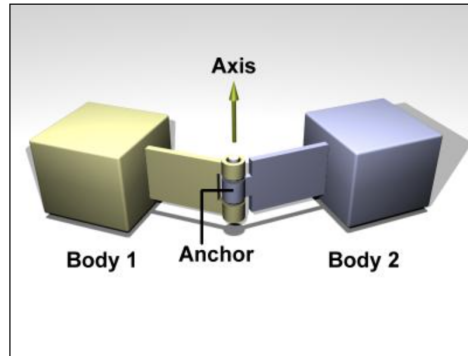
A		B			
	Joint	Part 1	Part 2	DOF/joint	Total DOF
	Cervical	Head	Neck	3	3
	Thoracic	Neck	Upper Torso	3	3
	Lumbar	Upper Torso	Lower Torso	3	3
	Sacral	Lower Torso	Pelvis	3	3
	c.Clavicle	Upper Torso	c.Collar	3	6
	c.Shoulder	c.Collar	c.Upper Arm	3	6
	c.Elbow	c.Upper Arm	c.Lower Arm	2	4
	c.Wrist	c.Lower Arm	c.Hand	2	4
	c.Hip	c.Pelvis	c.Upper.Leg	3	6
	c.Knee	c.Upper Leg	c.Lower Leg	2	4
	c.Ankle	c.Lower Leg	c.Heel	2	4
	c.Tarsal	c.Heel	c.Sesamoid	1	2

Figure 4.3: The 48 degrees of freedom model A. Hinge joints connect the toes and the heels. Universal joints are used at the wrists, elbows, knees and ankles. Four ball-and-socket joints connect five body segments along the spine from the head to the waist. Ball-and-socket joints are also used at the collar-bone, shoulder, and hip. B. A summary of the joints used in the model. c. = chiral: there are two of each of these joints (left and right). All joints limit the range of motion to angles plausible for human movement. Our model assumes that joint DOFs summarize the effects of component muscles.

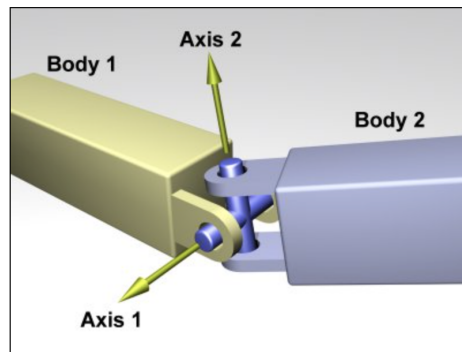
ankle are defined to possess two rotational degrees of freedom, analogous to a universal joint. All the remaining joints are defined as the ball and socket joints with three angular degrees of freedom. Therefore, the dynamic model totally includes forty-eight internal degrees of freedom. Building a humanoid model in this way is to treat joint connections as stiff springs which hold two body parts just like muscles, rather than holonomic rigid constraints.

4.1.2 Data Fitting

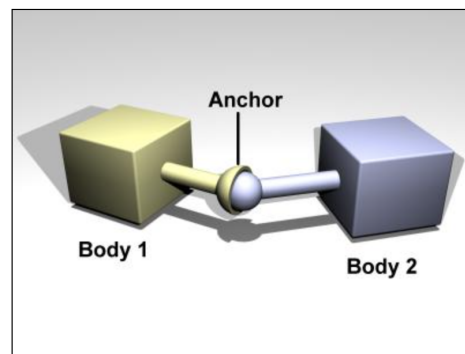
The technique is for fitting a model to the given motion capture data, including 1) assigning the markers used in motion capture to appropriate body segments,



(a) Hinge joint



(b) Universal joint



(c) Ball and socket joint

Figure 4.4: Three types of joints which were used in the dynamic model system.

2) determining the body segment dimensions (size), and the positions where the labeled markers should be attached.

The first step requires the knowledge of the topology of the model of a character model (Fig. 4.3) and the marker settings used in a motion capture system (Fig. 4.5). According to the marker settings, it is not difficult to assign markers manually. As for the same motion capture system, the markers usually on the same locations of motion-capture suits (Fig. 4.5), this process allows to go through for many different models. A method for the second step, determine the model size and the mappings between markers and body segments according to motion capture data, has been described in detail in S2 Appendix section of the paper [61]. This process can be archived by using our graphical user interface (Fig. 4.1). Please see the next chapter for more detail.

Given motion capture data of a subject, the model needs to be fitted to the subject's dimensions. Additionally, the model segments have inertial matrix properties. The initial mass assignment to each segment assumes a uniform density that is the same as the density of water ($1000\frac{kg}{m^3}$) for the volume of each body segment. The mass assignment should be modified to match that of a specific participant roughly.

4.1.3 Pose Fitting

Having addressed the issues in attaching the model to motion capture data, we turn to construct its capability of representing human movements. Recall that the model is built on a physical dynamic engine, and the joints connecting body segments are defined as stiff springs. Therefore the pose fitting process can be very intuitive: attach markers to appropriate body segments with ball

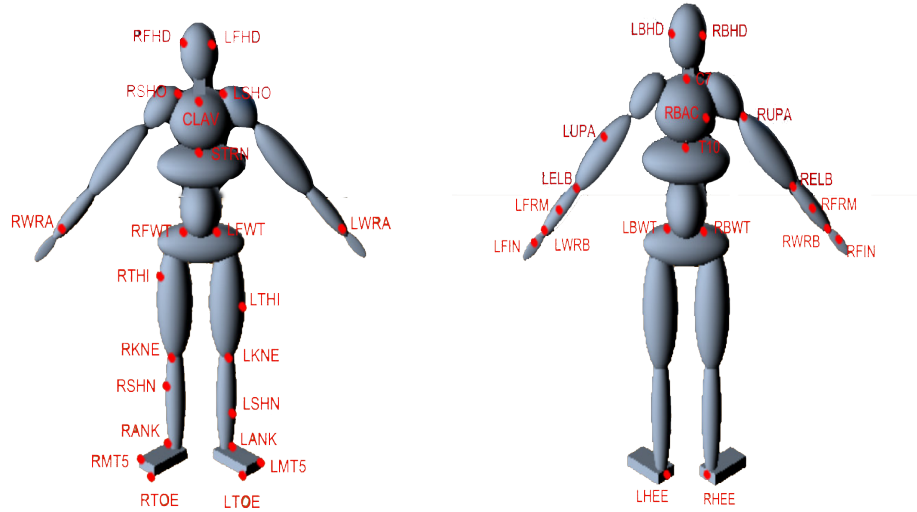


Figure 4.5: Marker arrangement on the motion capture suit. The suit contains 50 markers, as shown by the LEDs in total, but only 41 are used in the dynamic model, e.g., Markers that are used are present in the figure. Markers can easily be assigned to specific model segments. For example, the markers of RBHD, RFHD, LFHD and LBHD are assigned to the Head segment, while the markers of RBWT, RFWT, LFWT and LBWT belong to the Pelvis segment.

joints (springs) and then pull the body along. More specifically:

1. Create joints that connect markers with their associated body segments, named "marker joint". The marker joints are ball-and-socket and considered as springs as well.
2. Model markers as infinite mass points. The purpose is to guarantee that the model can reproduce the original motion exactly. As long as the marker mass is large enough, its associated marker joint can pull the body segment properly regardless of how heavy the body segment is.
3. Constrain each joint with weak, limited torque value. The aim is to

guarantee that the model body is flexible enough to follow the markers.

4. At each frame, markers achieve new positions and pull the body segments to appropriate positions through marker joints. Thus, the position and orientation of all body segments can be calculated simultaneously. In addition, the relative orientations (joint angles) between consecutive two frames will be recorded and used for the inverse dynamics process.

As known, the motion capture system is occasionally unable to locate the 3-dimensional locations of some markers, which is called signal loss. Thus some segments of the raw motion capture data sometimes are absent of some markers. In order to guarantee the model still employ a pose under such situations, range limits and stiffness serve as a prior over possible poses, more specifically:

1. The constraints of the internal degrees of freedom for each joint are set in advance. For example, the angle ranges of elbows and knees are restricted in order not to bend backward.
2. A preferred relative orientation between two connected body segments has been defined in advance. It is one of a joint's properties.

Joint error and the error reduction parameter (ERP) A joint constrains two body segments to have certain positions and orientations relative to each other. However, sometimes joint constraints are not satisfied caused by the following two reasons: 1) the settings the position/orientation of two body segments are conflicted, 2) In the simulation, small errors overspread leading to the body segments drifting away from their desired positions. The

ODE provides a mechanism to reduce joints errors: each joint is able to apply a particular force to adjust its bodies to correct alignment during each simulation step. This force is controlled by the error reduction parameter (ERP)⁵. The ERP has a value arrange from 0 to 1 that specifies what proportion of the joints errors will be fixed at the next simulation step. A good range of ERP values is (0.1, 0.8), and in our experiments, ERP is set to be 0.2 as default.

Soft constraint and constraint force mixing (CFM) There are two types of constraints: 1) hard constraints, with which the conditions will never be violated. 2) soft constraints, with which the conditions can be "softly" violated. For example, the collision constraint of two contacting bodies is hard if the colliding surfaces are made of steel, while the constraint is soft for some softer materials. In the open dynamic engine, the constraint force mixing (CFM)⁶ controls the distinction between hard and soft constraints. The CFM value should be positive, and the higher is the value, the softer is the constraint. In our experiments, the CFM value of marker joints is set to be 1×10^{-5} , and body segment joints use 1×10^{-6} .

4.1.4 Inverse Dynamics

An advantage of our human dynamic model is to calculate the torques and angular velocities applied at each joint or the required energetic cost to accomplish a particular movement. Given a sequence of joints' angles, the built-in functions of ODE can correctly compute the required torques/forces. The process is straightforward:

⁵ODE ERP http://www.ode.org/ode-latest-userguide.html#sec_3_7_0

⁶ODE CFM http://www.ode.org/ode-latest-userguide.html#sec_3_8_0

1. Use the joint angles recorded in the pose fitting process as the reference.
2. Set the target joint angles to be the same as the joint angles on the next frame.
3. Calculate the relative angular velocity of each pair of body segments based on the current joint angles and the target joint angles.
4. Call ODE built-in functions to achieve the computation of torques/forces required to implement the movement.

In our experiment, the initial state can be computed from the first and second frames of the joint angle sequence. To compute each joint's linear and angular velocity, we divided the difference between two consecutive frames by the time step. The time step depends on the motion capture system's settings that record human motions, e.g., if the motion data is sampled in 60 HZ, then the time step should be 0.016s (1/60). Next, continuously compute the torques between two consecutive frames and then apply them back to the model, leading to move the model from the initial state to the end state. In this way, we can reproduce a particular human motion by using the inverse dynamic method.

Residual torques/forces The inverse dynamics is a technique that uses measured kinematics of body segments and external forces (e.g., the ground reaction forces) to calculate net joint torques in a rigid body linked segment model [103, 27]. However, owing to physical measurement errors and incorrect modeling assumptions, discrepancies between the dynamics torques/forces of the model and the kinematics of the real motions require some actions to stabilize the dynamic model. In an inverse dynamics analysis, a common way to

compensate for this problem is by introducing "residual forces and torques," which do not exist in reality. In humans, these additions would be consequential of measurements in the human vestibular system. Such corrective systems have been extensively studied[108, 103, 91]. In our human dynamic, an external joint was created and connected to the model's waist to reproduce orientation deviations found during the pose-fitting pass. It is also called the "Hand of God (HOG)."

The external joint consisting of six degrees of freedom connects the waist and the global frame. Not all of the six degrees of freedom need to be used in practice, especially for in-situ motions: only two of them (pitch and roll) are necessary. The stabilization system completes the model. It can be implemented parallel, with the control used to stabilize the residual necessary to balance and allow the model to move through the interactions between feet and the ground.

4.1.5 Method summary

For each human subject, we construct a dynamic model and force that model to follow the subject's motion capture data, which leads directly to the recovery of joint angles. Our algorithm constrains the dynamic model to track these angles and consequently can estimate the correct joint torques. This concept was initially demonstrated in two dimensions for human walking by [28]. We have extended the method to the significantly more demanding 48 DOFs in three dimensions and arbitrary posture changes. Fig. 4.3 lists the body segments. The dimensions of each segment are fit to those of an individual subject. The principal difficulty is that the constraints in the high DOF 3D model

present many delicate numerical issues for the ODE solver that need to be addressed [18]. Currently, the dynamic model does not attempt to model stiffness components, with the consequence that it can only directly recover the net torques at each DOF.

The body segments are used by the simulation for both collision detection and the calculation of mass properties. Mass and inertial properties are computed from the volume of the body parts using a constant density of $1000 \frac{Kg}{m^3}$. The dimensions and articulation are designed to allow the model to reproduce most movements the human can make. For example, joints at the elbows have two DOFs to reproduce the elbow’s hinge movement and the twisting movement of the radius and ulna bones in the arm. Joint DOFs are also limited to prevent impossible movements such as reverse bending of the elbows or knees.

For data capture, a subject wears the motion capture system developed by PhaseSpace. Each PhaseSpace LED marker is mapped to a corresponding point on the model. The markers are then introduced into the physics simulation as kinematic bodies without collision geometry. As a heuristic, each kinematic marker body is effectively treated as having infinite mass so that when another dynamic body is attached through a joint constraint to a marker, only the dynamic body’s trajectory can be changed by the constraint.

The PhaseSpace motion capture system records 41 3-dimension positions of specific human body locations over time and maps these markers to appropriate locations on the model. When the simulation is stepped forward, a constraint solver attempts to find a body state that satisfies the internal joint constraints, the external marker constraints, and other constraints such as ground forces, joint stiffnesses, and conservation of momentum. Knowing

the kinematics allows the recovery of the dynamics since the joint velocities allow the equations of motion to be inverted. The retrieved forces can be used to generate feed-forward torque profiles for actuating the character.

The overall idea behind the method for calculating joint torques is straightforward and has been implemented in ODE. The mathematics underlying the rigid body simulation software used in our work is explained in the S1 Appendix section of this paper [61].

4.2 Results

This section focuses on describing the model’s capabilities through a series of examples in different settings. Several qualitative and quantitative tests of the human dynamic model were described in this section.

4.2.1 Test 1: Model Performance

The following two tests (noise tolerance, residual torques and forces) were initially conducted by Dr. Cooper [17] and then elaborated in more detail in the paper [61]. In order to maintain the completeness and consistency of this dissertation, we just summarized and showed the critical results here. Therefore, the following section mainly focused on how these two studies assess the performance of our human dynamic model.

Noise tolerance Given that the torque recovery technique is the basis for our experiments, it is essential to establish its accuracy in absolute terms. A straightforward to do this is to use a *particular model* to generate joint angles/torques data and then verify that these generating angles/torques can

be recovered with sufficient accuracy. To test the model accuracy and noise sensitivity, we first use the PhaseSpace motion capture system to gather the walking data and then let the model simulate the walking motion. To simulate possible sensor errors in the PhaseSpace system, we introduce noise into the simulated marker positions and study the accuracy of recovery with increasing noise levels.

Specifically, we used the human dynamic model to synthesize treadmill walking with or without Gaussian noises and then compute its accuracy. The synthesized “ground truth” joint angles/torques were generated in a preliminary pass through the original motion capture data. Then Gaussian noises were gradually increased and the corresponding joint properties were computed. The difference between the joint angles/torques from perturbed marker data and the “ground truth” values were considered errors caused by the noises. The experimental process is similar to the one in [82].

We first assessed the accuracy of motion trajectories without any noises. Fig. 4.6 and Fig. 4.7 showed the comparisons between the ground truth and the trajectories of the joint angles/body positions along a specific dimension. As shown in the two figures, the data is quite close to ground truth. Moreover, the ground truth sometimes exhibits some coarse or sharp changes, such as the “*l_knee*” lines in both figures around frame 170, caused by some unexpected errors in the motion capture recording system. Surprisingly, the recovered trajectories are pretty smooth even if the ground truth data is not perfect. This fact is one of the advantages of the assumption that the joint constraints behave like springs. However, the disadvantage of it causes apparent lag and damping of reconstructed trajectories. As a result, both the joint angles and the body positions lag behind the ground truth by a small amount (0.05 second

or 3 frames). Nevertheless, these results provide confidence that the HDM has the capability of handling noise.

Fig. 4.8 Body position trajectories reconstruction It shows the trajectories of selected body segments along the y-axis. This figure can be considered as a top view of the 3D motion and the projection of 3D trajectories of body segments on the ground.

Residual torques/forces and ground forces Recall that the torque calculation by the human dynamic model is ideal for solving the dynamic equations, but there needs to be a corrective system for unexpected errors in the actual situation. In the human system, there are multiple corrective systems based on vision, proprioception, and the vestibular system. In the classical inverse dynamic method, this problem is solved by introducing the non-realistic "residual forces and torques." The residual forces/torques perform mechanical work that does not exist in reality and may compromise energetic analyses [27]. Therefore, their values are usually considered as an indication of the validity of computational modelings. Therefore, their values are usually considered as an indication of the validity of computational modelings. The smaller the residual values are, the better the modeling is. The following study aimed to assess the effect of residual torque/forces on the results and compare the real ground forces and the one computed with our human dynamic model.

The fully configured system was tested against an objective set of measurements. We compared the computed force using human dynamic model to the ground force from a pair of force plates. A subject standing on the Wii^{TM} force plates varied their stance from one being supported exclusively by leg standing on one plate and then shifted their weight to the other leg to

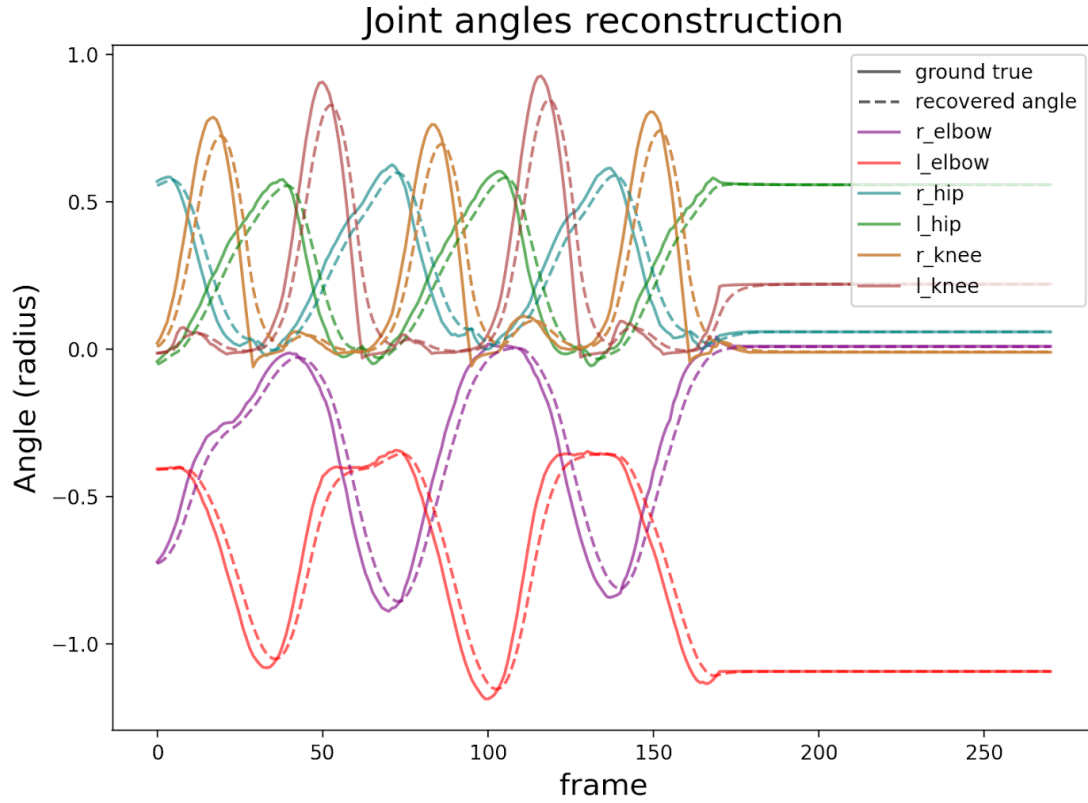


Figure 4.6: Joint angle trajectory reconstruction. The solid lines represents the ground truth, while the dash lines indicates the recovered angles. Simulating joints as spring smooths the ground truth but makes the recovered data lag behind a little bit. (a) and (b) shows the trajectories of selected joints along the x-axis and the selected body segments along the y-axis.

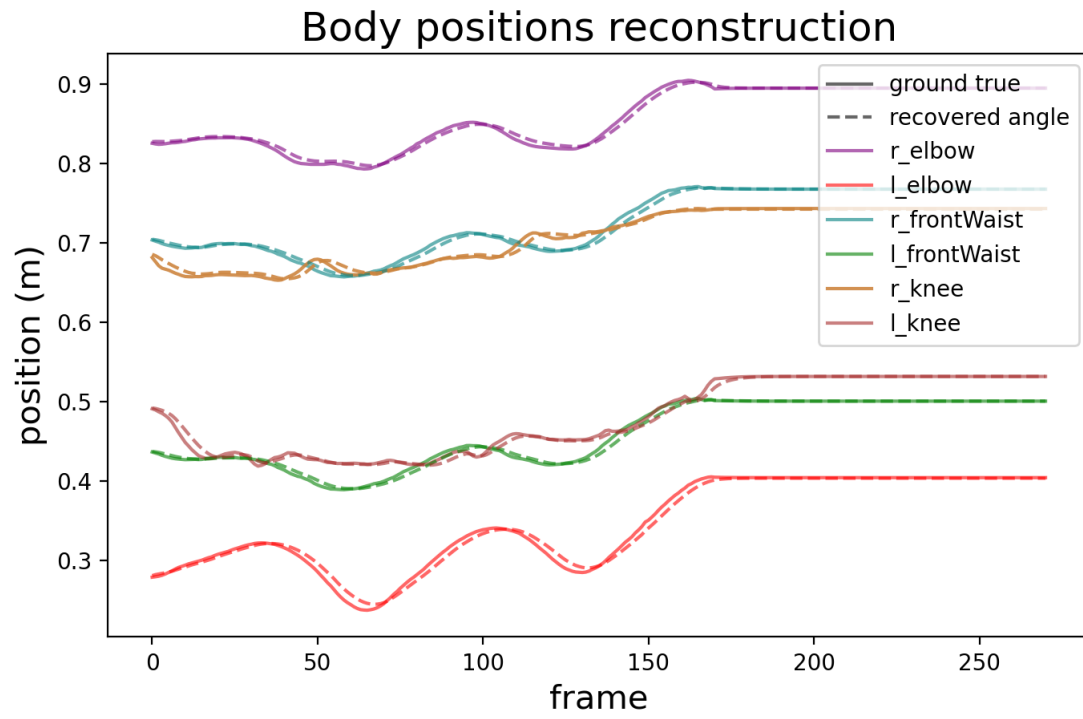


Figure 4.7: Body position trajectories reconstruction It shows the trajectories of selected body segments along the y-axis. This figure can be considered as a top view of the 3D motion and the projection of 3D trajectories of body segments on the ground.

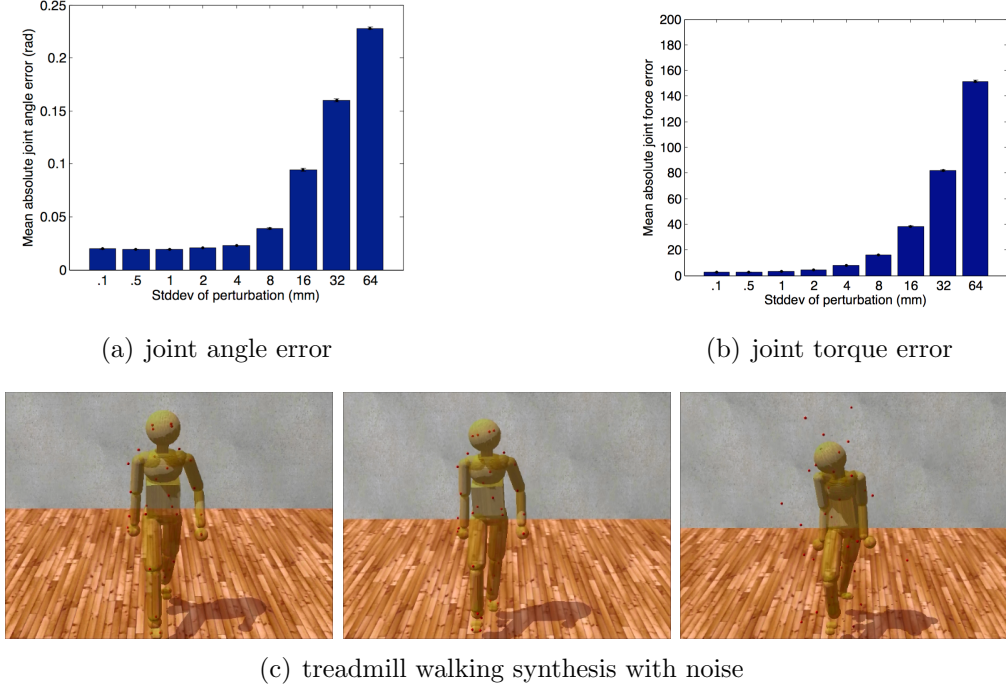


Figure 4.8: Model noise sensitivity [61]. The error of joint angles and internal torques with Gaussian noises. The process was repeated 20 times for each noise level with 9 different standard deviations that were (0.1, 0.5, 1, 2, 4, 8, 16, 32, 64) in mm. Error bars show the standard error of the mean. (a) The accuracy of the PhaseSpace motion capture device is approximately 5mm over its 3 x 6-meter workspace, resulting in an average angular error of 1 degree. (b) The same estimates for torque error are between 5 and 10 Nm, typically approximately 1%. These small errors are well within the requirements for our experiments. (c) Reconstructed poses. According to Gaussian perturbed walking data (0.1mm, 8mm, and 64mm noise levels), first use inverse dynamics to compute joint torques at each frame and then use forward dynamics to reproduce the walking motions. Although the model follows the reference motion poorly at very high levels of noise, the movement still looks, qualitatively, like walking.

be supported by the other plate. Fig. 4.9 illustrated that with 30 Nm residual torque, the human dynamic model was able to reproduce the transition from standing on one foot to the other. The results also showed that the ground forces computed from our method compared to those taken from force plates are surprisingly close.

The residual torques are very modest, being within $\pm 5\%$ of the maximum excursion. The correspondence is a little better as the faux vestibular balance forces are not factored into the comparison. Note also that we cannot expect the correspondence to be exact during the phase between the two stances as there is no attempt in the model in this test to make the dynamics of the changing stance match that of the force plates. To generate independent movements, such as grasping, might need additional accuracy [91], but for estimating a subject’s energetic cost, the accuracy is well within range.

4.2.2 Test 2: Model Validation

The previous demonstrations report on tests of the accuracy of the system in entirely artificial situations. Herein we describe three tests of the whole body model’s ability to fit data obtained from human subjects. The first test uses a subject carrying out successively more difficult reaches in a virtual reality environment to test whether the model’s estimate of movement costs correlate with increasing task difficulty. The second test simulates data from an issue facing movements in an aging population. For example, do aging subjects’ reduced use of arm swing while walking incur a movement cost, and does the HDM’s estimate correspond to laboratory treadmill data? The final test demonstrates an essential property of the model concerning its degrees of

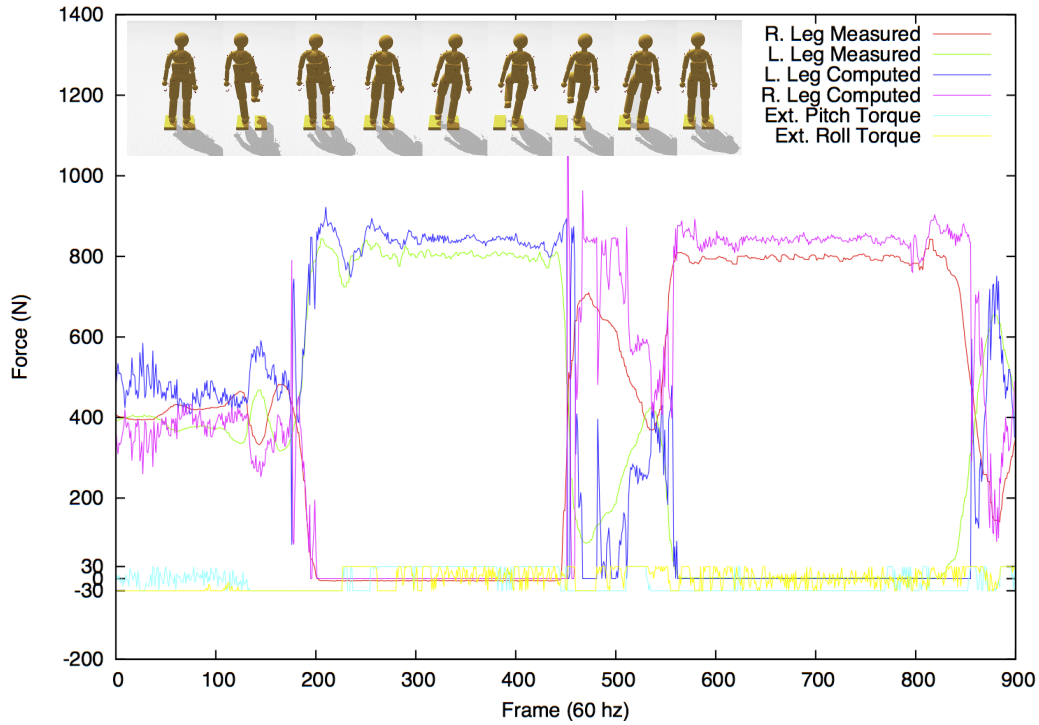


Figure 4.9: Comparing ground forces between the model and the Wii force plate [61]. (Top) Two Wii force plates serve as an accurate calibration reference. A subject stood on the two plates and then changed stances, balancing first on the left foot and next on the right. (Bottom) The comparison between the measurement systems is surprisingly good, during the stance phases, showing only a 5% difference between the *measured* ground forces and the *computed* forces.

freedom. The critical observation is that the virtues of their interconnections constrain the degree of freedom of the model; thus, controlling a posture can be achieved with a significantly reduced set of crucial marker positions. It has implications for movement control programs.

Whole body reaching The movement accuracy test is encouraging, but the importance of the method depends on its usefulness to capture the energetic cost of whole-body movements in a complex experimental setting. One

such venue is a three-dimensional Virtual Reality (VR) environment. The advantage of the VR environment for studying human movements is that the dimensions and the dynamic variations of the parametric quantities describing the setting can be varied with complete experimental control.

In this experiment, we studied where human subjects needed to use whole-body movements cost choosing actions. From a particular start, a human subject touched targets suspended in 3D space. The experimental setup is demonstrated in Fig. 4.10. The subject is wearing the PhaseSpace motion capture suit and the nVisor head-mounted stereo display. From a fixed starting position, a subject is instructed to touch one of the targets and return to the starting position.

Tests were able to establish that, just focusing on integrated net torque and avoiding stiffness, the total cost of a movement recorded by our system reliably discriminates the energetic costs of the movement in the way hypothesized. The hypothesized cost of reaching for and touching each of the targets was ranked based on distance and height relative to the subject. Note that target 2 is the least expensive as the subject does not have to crouch or extend significantly to touch it. Targets 5 through 8 are more costly than targets 1 through 4 as they require that the subject take a step to touch them. These results were expected, but the point was to show that the overall setting and model could produce reliable torque estimates.

This demonstration shows that the model can be used in any setting where the cost of a movement is hypothesized to be a constituent factor. We develop this technique further in the next demonstration.

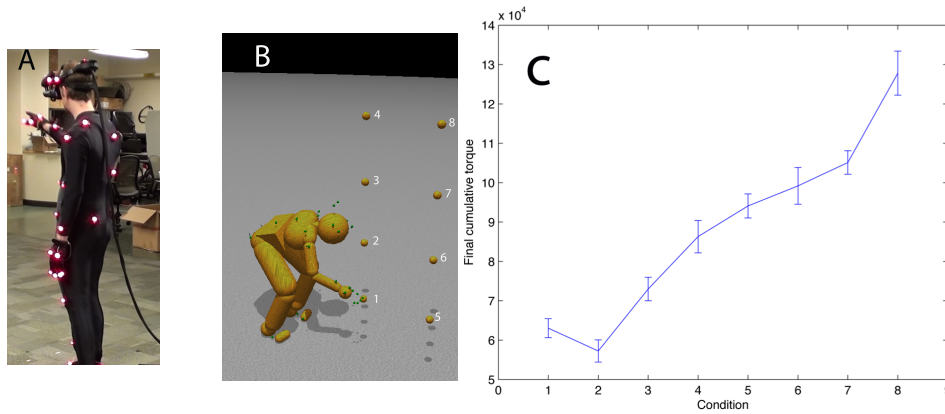


Figure 4.10: Reaching in a virtual reality environment [61]. A) A subject reaches to touch virtual targets seen in a HMD. The subject’s reach is unconstrained. B) The subject reaches the different numbered targets on separate trials. C) The average integrated torque over ten trials per reach shows that the method reliably discriminates between movement costs for the further and higher locations.

Comparing the human dynamic model with a prior experimental

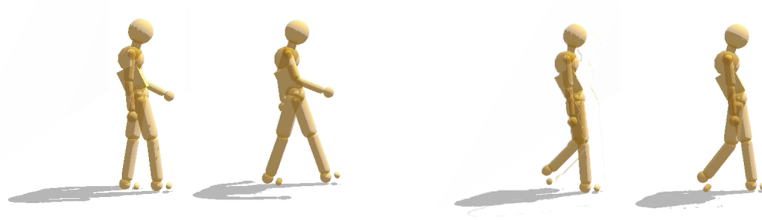
result Once the joint stiffness parameters were adjusted appropriately, can it reproduce the results of a stiffness modulating experiment? The experiment we tried was to replicate that of Ortega et al. [79]. They showed that arresting the arm swing during treadmill walking incurred an increased metabolic cost of 6%. Our hypothesis was that to reproduce this result we could modify our walking data for the model so that the arms were clamped by the sides with stiff stationary markers.

To test this feasibility, we used one of our HDM walking data sets in a test situation. The cost of walking was computed and with a modification designed to model the data in [79]. To simulate their experiment, we modified the model data so the arms could swing with the walking gait for the standard case, but for the restricted case, the arms were constrained by markers that

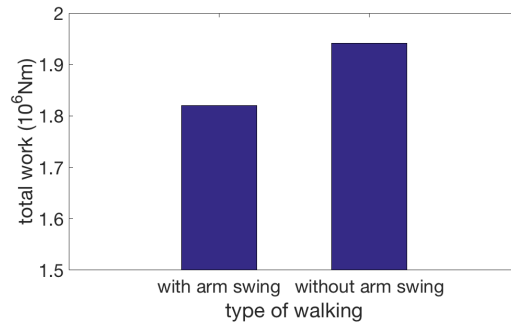
move with the stride but are not allowed to swing. Since the arms under restricted situation were not allowed to balance the leg movements, we expected the energetic cost to be higher. As shown in Figure 4.11, the result was that the constrained walk was about 6 % more expensive than the standard walk, which was essentially the value obtained by the Farley lab [79]. The use of the human dynamic model in imitating this experiment shows off the utility of the model; no elaborate tuning was necessary to obtain the preliminary result other than restraining the arms.

Controlling poses using reduced marker sets Tests of movement accuracy revealed that the dynamics engine was able to tolerate significant noise levels added to the marker positions. Another possibility is to use a subset of the markers to constrain the dynamics and still produce good walking gaits.

Human pose sequences from simple single-behavior motions lie on a very low-dimensional linear subspace [6, 58]. The principal component analysis (PCA) is commonly used to map motions from high-dimensional space to lower-dimensional space. Fig. 4.12 (a) shows percentages of variances explained by the principal components for six different walking sequences. The results indicate that two leading principle components can cover over 95% variance; in other words, two-dimensional space can sufficiently describe a walking motion. Fig. 4.12(b) presents projections of six walking sequences onto their two leading principal axes. The curves have similar shapes, and they differ primarily by translations and scales. Furthermore, research [59] shows that for movements with suitable internal configurations, a reduced marker set consisting of the head, trunk, hands, and feet markers is enough to control the body posture sequences. This property could have been expected from studies of



(a) walking with arm swing (left) and stiff arm (right).



(b) energy cost

Figure 4.11: Comparison of efforts while walking with/without arm swing. (a) In a preliminary test of our design, the energetic cost of normal walking is compared to the case where the arms are constrained from swinging. We hypothesize that if subjects are instructed to walk without moving their arms, they will accomplish this by using muscle co-contraction and that this effect can be realized in the human dynamic model with stationary markers that keep the arms vertical. (b) The increased cost measured by the human dynamic model is 6.1 %, extremely close to the 6 % result obtained by Ortega [79].

muscle synergies, which show that muscle contractions coordinate in movement generation [97, 96].

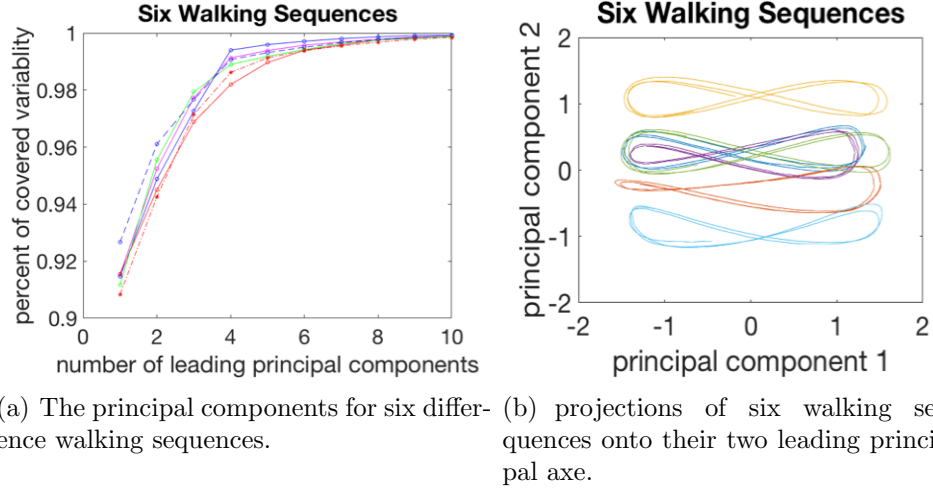


Figure 4.12: Apply the PCA algorithm to six different walking sequences.

As the original feature space of human motions has too many dimensions, e.g., a model with 50 markers means a 150-dimension coordinate system represents one pose, the human dynamic model should be able to retain movement accuracy with a reduced marker set. Fig. 4.13 shows a qualitative comparison between a walking posture generated using the full marker set (on the left) and the one generated using a reduced marker set (on the right). To achieve the reduced marker posture, we started the model in an upright stance with the arms by the side, and then the reduced set markers are moved slowly along trajectories that leave them in the final posture. The straight arms take advantage of the elbow joint angle limitation. Besides, the joints' stiffness and pre-defined constraints automatically force the ODE to produce a pose, which is natural-looking and close to the fully constrained pose. Moderate joint stiffness and body mass inertia make the model capable of dealing with noises and

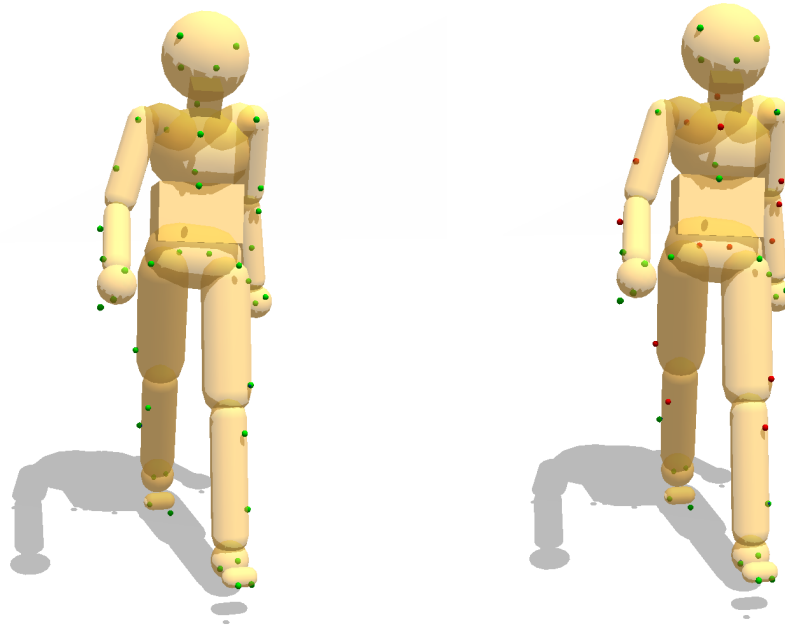
occlusions in the motion capture data. To test this feature of human dynamic model quantitatively, the recovered joints angles while walking according to the reduced marker set were compared with those from the full marker set. Fig. 4.14 illustrates that the recovered joints' angles are quite similar to the original joints' angles.

This result has important general implications. First of all, the finding suggests that the kinematic plan for movements can be compressed into a subset of formative trajectories, leaving the remaining degrees of freedom interpolated using the body's dynamic constraint. Another aspect of this observation is that the reduced set can be used for adjusting movements to individual circumstances, again leaving the detailed interpolation to the dynamics.

4.3 Discussion

The chapter has aimed to describe a novel system for quantitatively modeling whole-body movements. Its 48 degrees of freedom and generalized spring constraints allow models of scale that are robust to disturbances. In addition to being an analytical tool, it can also generate movements from a kinematic plan.

The core of our simulations is taking advantage of considering constraints as implicit springs. The moderate parameters of joints exhibit many advantageous properties. For example, they stabilize the simulated movements and reduce constraint errors. A fundamental question concerned with the human dynamic model system is whether it can recover the trajectories and the cost of a known physical system's complex motion—the experiments described above showing the human dynamic model synthesizing human motions with



(a) A walking posture with full marker set (b) A walking posture with reduced marker set

Figure 4.13: Movement control using dynamic synergies Markers in green are attached, while markers in red are detached. Thus, as shown, the left postures are pretty close to the right one.

high levels of accuracy. One further principle behind our tests is that one way of illustrating the method’s robustness is to combine a kinematic data set from the source with another set of dynamic parameters. In tests, the data gathered with a different motion capture device is combined with the inertial data from another model to make a composite. Our tests used the Carnegie Mellon University’s graphics laboratory’s motion capture database ⁷. This beneficial and extensive database contains whole-body motion data sets for different human subjects performing various natural motions. The database was created

⁷CMU Graphics Lab Motion Capture Database: <http://mocap.cs.cmu.edu/>

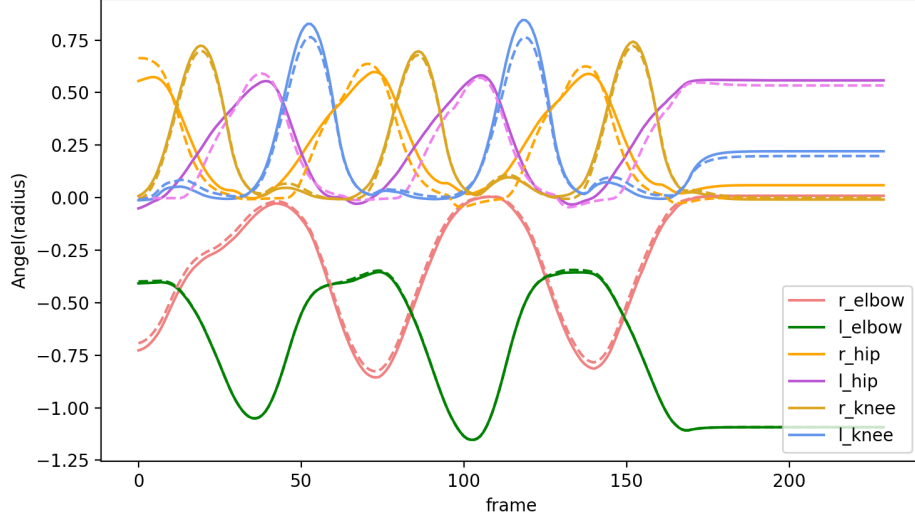


Figure 4.14: Comparison of joint angles along the selected degree of freedom. Solid lines show joint angles recovered based on the full marker set. Dashed lines show joint angles recovered based on reduced marker set.

by motion capture, and the positions of markers on the bodies are one of the primary sources of motion data. We did not know the individual dynamic parameters. However, we could use the HDM to compute joint torques for the hybrid system by adopting the database’s marker conventions. Although the estimate is thus done for a synthetic pairing of kinematic data and dynamic parameters, the point is to show that, even with this combination, the integration is stable and leads to identifiable torques.

A central feature of the system is the production of the movements’ energetic cost to provide the capability to compare different movement scenarios. Achieving this goal can be tricky, owing to the lack of systems that can provide independent cost measures. Energetic cost measurement of hu-

man movements has been studied for decades. The most straightforward and frequently used method is to measure the metabolic cost, e.g., subjects breathe through a mouthpiece to measure oxygen consumption rates. Measuring the changes in muscle coactivation and stiffness using Electromyographic (EMG) is another common way to reflect metabolic changes. However, these methods are time-consuming, and the required configuration restricts the variety of experiments. For example, the VO₂ process does not work for virtual-reality tasks as subjects need to wear the VR helmet on their head, leaving little space for a mouthpiece.

Compared with the above methods, the human dynamic model provides a stable and versatile platform with several uses. One is the use of force plates to measure the stance's change, as shown in our experiment. Another option is to use the human dynamic model system to produce correlations with similar tests with human subjects, such as our research with stiff-arm walking. Once we have vetted the system in many such areas, it can be used as a predictive tool, as in the experiment showing the different costs of reaching targets. We have developed a large-scale three-dimensional tracing experiment in virtual reality shown in chapter 3 to elicit natural whole-body movements under common goals. The subsequent work (shown in the chapter 6) analyzed the energetic cost using the human dynamic model.

Chapter 5

Human Dynamic Model System

As described in the last chapter, our human dynamic model is a robust and inexpensive multi-purpose tool for simulating, analyzing, and synthesizing humanoid movement. However, the procedures of using it are kind of complicated. Users need to deploy the model manually and appropriately, such as assign markers to appropriate body segments, locate markers to relative positions to rigid bodies, etc. Therefore, we further developed the system so as to turn it into a usable and practical application. A demo has been uploaded online¹.

5.1 System Configuration

The structure of the whole system is shown in Fig. 5.1. The first step of synthesizing humanoid movements by using our human dynamic model is to load motion capture data properly. The process includes four steps:

¹HDM UI Demo <https://youtu.be/ASs4Wo5PQcM>

1. Load motion capture data. There are different formats of motion files, such as .c3d, .amc, .csv, etc.
2. Adjust the model body dimensions based on real motion data as the body types of people who made motions are different.
3. Assign markers to appropriate body segments. Pay attention that motion capture data could include different numbers of markers according to different motion capture systems. Even using the same motion capture system, makers' indexes could be different as well.
4. Adjust the relative positions between markers and their corresponding body segments.

Thus, given a motion capture data set, the system's configuration files should include: 1) A motion capture data file. 2) A model body dimensions file. 3) A file mapping markers to body segments. 4) A maker-body relative position file. In order to simplify the process, we classify all motions into two categories: default motions and custom motions.

5.1.1 Default Motion Settings

We define the motions in the Carnegie Mellon University (CMU) Motion Capture Database ² as default motions. This database includes 2605 trials in 6 categories (Human Interaction, Interaction with Environment, Locomotion, Physical Activities & Sports, Situations & Scenarios, Test Motions) and 23 subcategories. It is robust, comprehensive, and free to access.

²<http://mocap.cs.cmu.edu/>

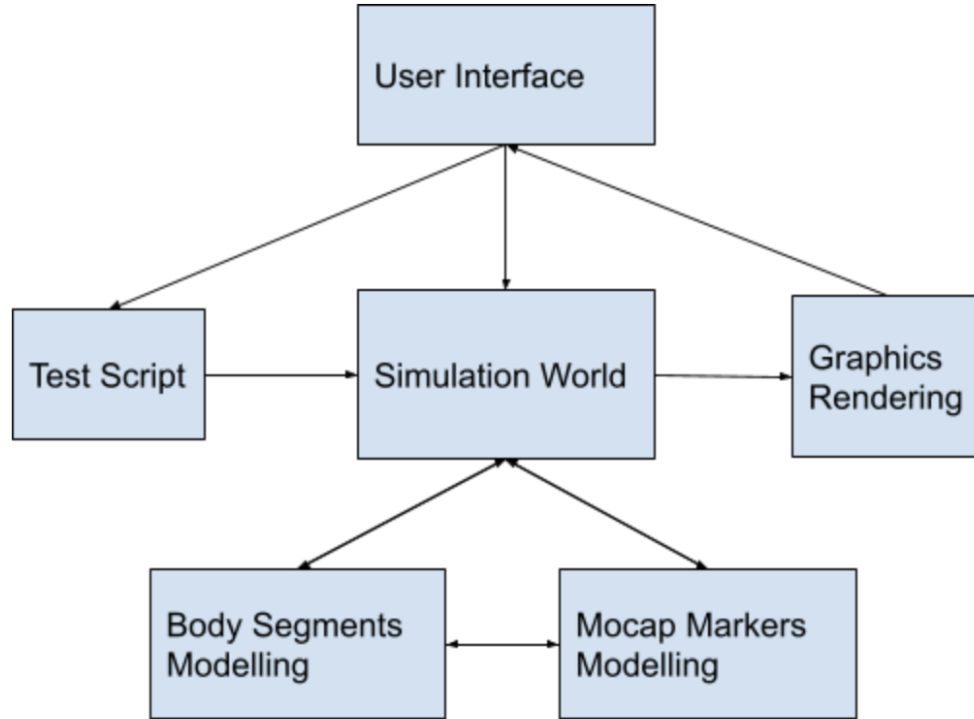


Figure 5.1: Big picture of the human dynamic model system.

To illustrate how to configure the model based on a default motion file, we will take this motion data "02_01_walk.c3d"³ for example. Its markers' indexes and names are shown in Fig. 5.2. Therefore, assign a marker to a body segment is actually to map the marker index to the body segment index. In the implementation, the system required a file named "default_markMap.txt" to record the mappings between markers and body segments. Fig. 5.3 shows

³<http://mocap.cs.cmu.edu/search.php?subjectnumber=2>

the relationship and an example of "default_markMap.txt".

Motion Capture Data -- Markers				Human Dynamic Model -- Body Segments	
Index	Marker Name	Index	Marker Name	Index	Body Name
0	LBWT	21	RKNE	0	HEAD_BODY
1	RBWT	22	LSHO	1	NECK_BODY
2	LFWT	23	C7	2	UP_TORSO_BODY
3	RFWT	24	LKNE	3	R_COLLAR_BODY
4	LFRM	25	RSHN	4	RUP_ARM_BODY
5	RWRA	26	RBHD	5	RLO_ARM_BODY
6	RFRM	27	LBHD	6	R_HAND_BODY
7	LWRB	28	LFHD	7	L_COLLAR_BODY
8	RELB	29	LSHN	8	LUP_ARM_BODY
9	LWRA	30	RFHD	9	LLO_ARM_BODY
10	RTHI	31	RANK	10	L_HAND_BODY
11	LELB	32	RMT5	11	LO_TORSO_BODY
12	T10	33	RTOE	12	WAIST_BODY
13	STRN	34	RSHO	13	RUP_LEG_BODY
14	LFIN	35	LANK	14	RLO_LEG_BODY
15	RFIN	36	LHEE	15	R_HEEL_BODY
16	RWRB	37	CLAV	16	R_TARSAL_BODY
17	LUPA	38	RHEE	17	LUP_LEG_BODY
18	LTHI	39	LTOE	18	LLO_LEG_BODY
19	RUPA	40	LMT5	19	L_HEEL_BODY
20	RBAC			20	L_TARSAL_BODY

(a) Markers indexes and names

(b) Body segments indexes and names

Figure 5.2: The markers settings of motion capture data and the body settings of our Human dynamic model

Motions from the CMU database usually have the same number of markers but different marker indexes. Thus, for using our human dynamic model, users needed to assign markers to body segments manually: extract the marker information from the C3D file and then map them to our model, which was very inconvenient. To make our system more user-friendly, assigning markers to body segments has been automated. Some movements from the CMU motion capture database may have different marker settings, and users need to map them by hand. However, users only need to load the motion

Marker - Body Mappings							
Index	Marker Name	Index	Body Name	Index	Marker Name	Index	Body Name
0	LBWT	12	WAIST_BODY	21	RKNE	13	RUP_LEG_BODY
1	RBWT	12	WAIST_BODY	22	LSHO	8	LUP_ARM_BODY
2	LFWT	12	WAIST_BODY	23	C7	1	NECK_BODY
3	RFWT	12	WAIST_BODY	24	LKNE	18	LLO_LEG_BODY
4	LFRM	10	L_HAND_BODY	25	RSHN	14	RLO_LEG_BODY
5	RWRA	6	R_HAND_BODY	26	RBHD	0	HEAD_BODY
6	RFRM	5	RLO_ARM_BODY	27	LBHD	0	HEAD_BODY
7	LWRB	10	L_HAND_BODY	28	LFHD	0	HEAD_BODY
8	RELB	5	RLO_ARM_BODY	29	LSHN	18	LLO_LEG_BODY
9	LWRA	10	L_HAND_BODY	30	RFHD	0	HEAD_BODY
10	RTHI	13	RUP_LEG_BODY	31	RANK	15	R_HEEL_BODY
11	LELB	9	LLO_ARM_BODY	32	RMT5	16	R_TARSAL_BODY
12	T10	11	LO_TORSO_BODY	33	RTOE	16	R_TARSAL_BODY
13	STRN	11	LO_TORSO_BODY	34	RSHO	4	RUP_ARM_BODY
14	LFIN	10	L_HAND_BODY	35	LANK	19	L_HEEL_BODY
15	RFIN	6	R_HAND_BODY	36	LHEE	19	L_HEEL_BODY
16	RWRB	6	R_HAND_BODY	37	CLAV	2	UP_TORSO_BODY
17	LUPA	8	LUP_ARM_BODY	38	RHEE	15	R_HEEL_BODY
18	LTHI	17	LUP_LEG_BODY	39	LTOE	20	L_TARSAL_BODY
19	RUPA	4	RUP_ARM_BODY	40	LMT5	20	L_TARSAL_BODY
20	RBAC	2	UP_TORSO_BODY				

(a) Marker-body Mappings



(b) Part of a mapping file

Figure 5.3: The mappings and an example of a mapping file. In the mapping file, the index of a row represents the index of a marker. The value on each row indicates the index of the assigned body segment. For example, the first-row index is 12 means the marker of which the index is 0 should be assigned to the body segment with index 12, which means marker "LBWT" is attached to the body segment named "WAIST_BODY".

capture files without concerning the marker assignments for most cases.

We find that our default settings of model body dimensions and marker-body relative positions also work for most cases. However, for specific cases, users might need to adjust their values manually. The method has been described in the method section and the S2 Appendix of the paper [61].

5.1.2 Custom Motion Settings

The system also supports synthesizing users' customized motions. However, users need to define their model setting files by themselves. For example, the motion capture data of the virtual tracing motions were stored in a CSV file that includes 50 markers with no indexes and names (Fig. 5.4 (a)). Currently, the system supports reading motion capture data from CSV files. For other formats of motion files, users need to either convert them to C3D files or code them directly in the system. After loading motion files to the system, users need to manually map the fifty markers to twenty-one body segments based on both the marker settings shown in Fig. 3.3 and the body settings shown in Fig. 5.2 (b). Fig. 5.4 (b) shows the marker-body mapping relationships of the virtual tracing motions. Next, users were required to define the body segments' sizes and the marker-body relative positions based on the loaded motion capture data. We would suggest using default settings as a starting point because of the similarity of human skeletons. Finally, after uploading all the required files to the system through the user interface, the motion will be simulated and shown on the display board.

In addition, users can draw some objects with which the custom motion is interacting in the virtual physical world. Currently, the system only supports

drawing lines by loading external CSV files. For other shapes, users need to code them directly in the system.

5.2 User Interface

The interface includes three components: a display panel, a control panel, and a functional panel, which is shown in Fig. 5.5.

5.2.1 Display panel

The display panel is to show the simulated results. It has two sub-panels: "3D view" and "Graphs".

1. "3D view" is to display the simulated motions (shown in Fig. 5.5). When the simulated world steps forward, the graphics will automatically be rendered, updated, and shown in the 3D view panel.
2. "Graphs" is to illustrate the reconstructed joint angles or torques (shown in Fig. 5.6). It allows users to interact with the graph, such as modifying the titles, frames, and labels, selecting or deleting specific curves, scaling the graph's view, etc.

5.2.2 Control panel

The "control panel" is to control how to simulate the motions (shown in Fig. 5.5). It includes three components: display control, simulation control, and marker data control.

	A	B	C	D	E	F	G	H	I	J	K	L	M
2	-0.238471	1.61128	0.782287	4	-0.270962	1.72545	0.912902		-0.301998	1.667291	0.820637		-0.09053
3	-0.239159	1.612575	0.783483	4	-0.271761	1.725977	0.914705		-0.302714	1.668144	0.822043		-0.091343
4	-0.23961	1.613819	0.78463	4	-0.272317	1.726483	0.916456		-0.303181	1.668982	0.823387		-0.091992
5	-0.239826	1.61501	0.785728	4	-0.272632	1.72697	0.918153		-0.303397	1.669806	0.824669		-0.092477
6	-0.239806	1.616149	0.786778	4	-0.272705	1.727435	0.919796		-0.303363	1.670617	0.82589		-0.092798
7	-0.239549	1.617236	0.787778	4	-0.272536	1.727881	0.921387		-0.303079	1.671413	0.827048		-0.092954
8	-0.239056	1.61827	0.78873	4	-0.272126	1.728306	0.922924		-0.302544	1.672196	0.828146		-0.092947
9	-0.238328	1.619252	0.789633	4	-0.271474	1.728711	0.924408		-0.30176	1.672965	0.829181		-0.092776
10	-0.237363	1.620182	0.790487	4	-0.270581	1.729095	0.925839		-0.300725	1.673719	0.830155		-0.09244
11	-0.236162	1.621059	0.791292	4	-0.269446	1.729459	0.927217		-0.299439	1.67446	0.831067		-0.091941
12	-0.234729	1.62198	0.792128	4	-0.2681	1.72986	0.928599		-0.297874	1.675273	0.831956		-0.091496
13	-0.232941	1.6228	0.792848	4	-0.266484	1.730204	0.929867		-0.295966	1.676058	0.832747		-0.090869
14	-0.230833	1.623547	0.793592	4	-0.264512	1.730518	0.931084		-0.293808	1.676814	0.833474		-0.090028
15	-0.228397	1.624237	0.794229	4	-0.262325	1.730779	0.932189		-0.291413	1.677539	0.834134		-0.088978
16	-0.225742	1.62482	0.794728	4	-0.259885	1.731039	0.93337		-0.288751	1.6782	0.834706		-0.087471
17	-0.222971	1.625311	0.795167	4	-0.257252	1.731264	0.93445		-0.285943	1.678797	0.835223		-0.085837
18	-0.220194	1.62578	0.795505	4	-0.254416	1.731455	0.935374		-0.283034	1.679318	0.835698		-0.083938
19	-0.217564	1.626134	0.795749	4	-0.251516	1.731625	0.936266		-0.280041	1.679753	0.836113		-0.081968
20	-0.215176	1.626375	0.796028	4	-0.248573	1.731722	0.93708		-0.277102	1.680121	0.836496		-0.079802

(a) Part of tracing motion capture data

Marker - Body Mappings							
Index	Marker Name	Index	Body Name	Index	Marker Name	Index	Body Name
0	marker0	0	HEAD_BODY	25	marker25	10	L_HAND_BODY
1	marker1	0	HEAD_BODY	26	marker26	10	L_HAND_BODY
2	marker2	0	HEAD_BODY	27	marker27	10	L_HAND_BODY
3	marker3	0	HEAD_BODY	28	marker28	10	L_HAND_BODY
4	marker4	0	HEAD_BODY	29	marker29	10	L_HAND_BODY
5	marker5	0	HEAD_BODY	30	marker30	11	LO_TORSO_BODY
6	marker6	3	R_COLLAR_BODY	31	marker31	2	UP_TORSO_BODY
7	marker7	3	R_COLLAR_BODY	32	marker32	2	UP_TORSO_BODY
8	marker8	4	RUP_ARM_BODY	33	marker33	11	LO_TORSO_BODY
9	marker9	5	RLO_ARM_BODY	34	marker34	12	WAIST_BODY
10	marker10	6	R_HAND_BODY	35	marker35	12	WAIST_BODY
11	marker11	6	R_HAND_BODY	36	marker36	12	WAIST_BODY
12	marker12	6	R_HAND_BODY	37	marker37	13	RUP_LEG_BODY
13	marker13	6	R_HAND_BODY	38	marker38	14	RLO_LEG_BODY
14	marker14	6	R_HAND_BODY	39	marker39	14	RLO_LEG_BODY
15	marker15	6	R_HAND_BODY	40	marker40	16	R_TARSAL_BODY
16	marker16	6	R_HAND_BODY	41	marker41	15	R_HEEL_BODY
17	marker17	6	R_HAND_BODY	42	marker42	16	R_TARSAL_BODY
18	marker18	7	L_COLLAR_BODY	43	marker43	12	WAIST_BODY
19	marker19	7	L_COLLAR_BODY	44	marker44	17	LUP_LEG_BODY
20	marker20	8	LUP_ARM_BODY	45	marker45	18	LLO_LEG_BODY
21	marker21	9	LLO_ARM_BODY	46	marker46	18	LLO_LEG_BODY
22	marker22	10	L_HAND_BODY	47	marker47	20	L_TARSAL_BODY
23	marker23	10	L_HAND_BODY	48	marker48	19	L_HEEL_BODY
24	marker24	10	L_HAND_BODY	49	marker49	20	L_TARSAL_BODY

(b) Marker-body mapping

Figure 5.4: The custom mocap data and the corresponding mappings. (a) In the CSV file, the columns indicate marker positions in order. Every four columns represent one marker position (x, y, z) followed by a credibility value C. According to the motion capture system, if C is between 4 and 10, the recorded positions have high credibility. One row illustrates all the markers' positions at one frame.

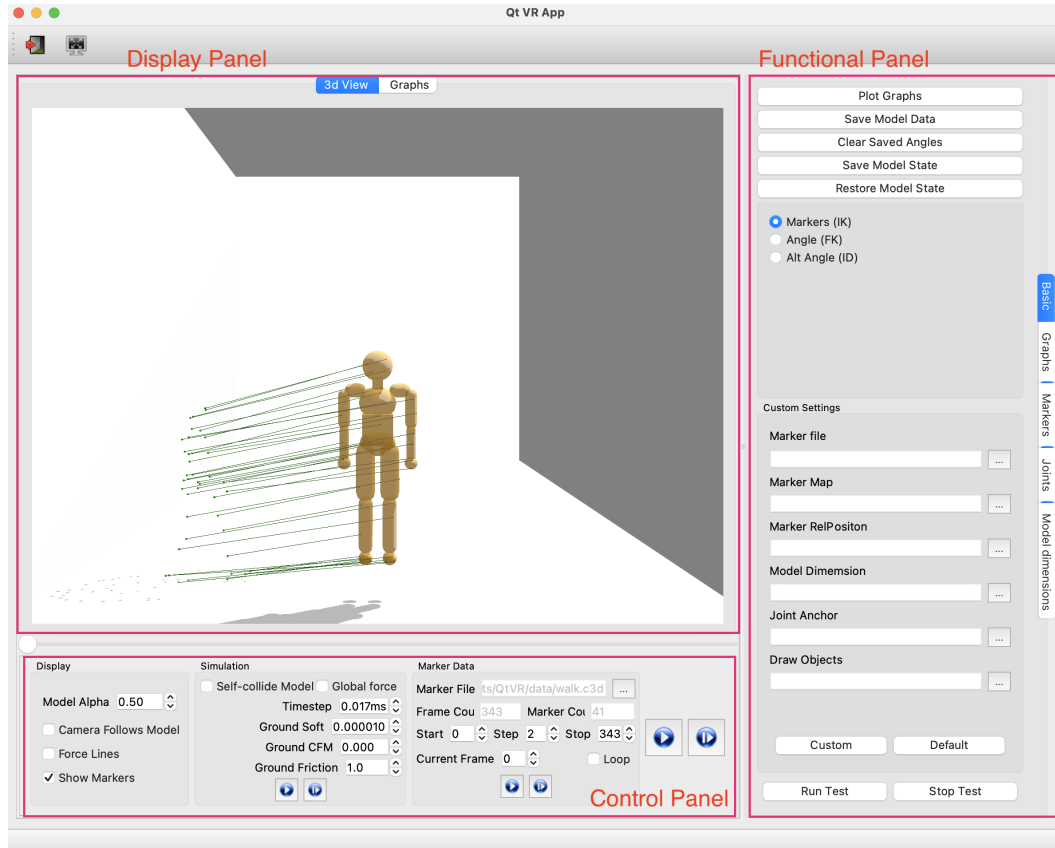


Figure 5.5: User Interface of Human Dynamic Model System. It consists of a display panel, a control panel, and a functional panel. In the figure, the display panel shows the initial state of the whole system. The human dynamic model was initially located in the middle of the simulated world and connected with all markers. Green points represent the attached markers, and green lines illustrate their connections with associated body segments.

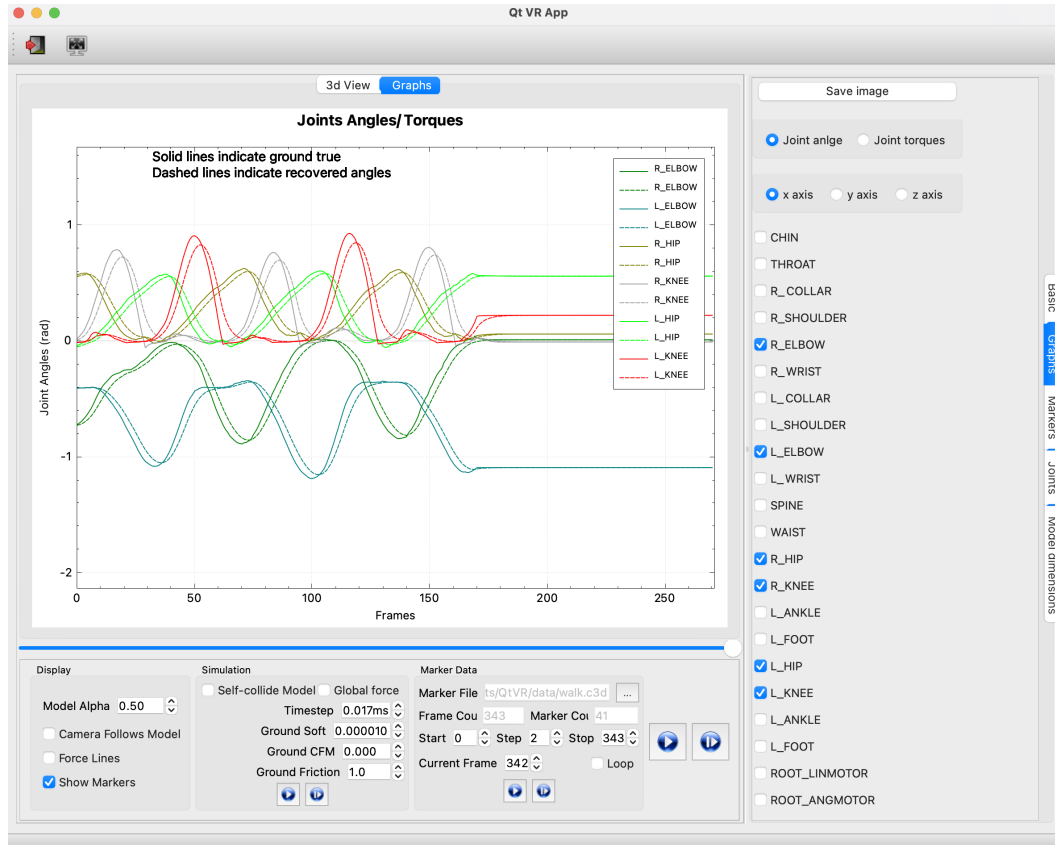


Figure 5.6: User Interface of Human Dynamic Model System – Graph display panel and functional panel. Users are able to choose to plot desired information, and the result will be shown on the display board on the left.

Display control This sub-panel controls the display "3D view" sub-panel. Its changes will be immediately illustrated on the board.

1. "Model Alpha" controls the transparency level of rigid bodies of the model.
2. "Camera follow model" decides whether the camera's center should be fixed or follow the model.
3. "Force Lines" controls whether to show the ground force line or not.
4. "Show Markers" controls whether to show the markers and their connection lines. In Fig. 5.5, those green points represent the attached markers, and those green lines illustrate their connections with associated body segments.

Simulation control This sub-panel is to control and show the simulation settings. It allows adjusting the parameters' values as well.

1. The "Self-collide model" controls whether or not if two rigid bodies from the same joint group should collide with each other. Currently, the whole system is not "self-collide".
2. "Global forces" indicates whether or not the calculated values are in global coordinates. Currently, the whole system is in global frames.
3. "Time step" shows the current time settings. It depends on the motion capture data. For example, if the motion data is sampled in 60 HZ, the time step is 0.017s.

4. "Ground soft" shows the value of the softness parameter for ground material. The higher is the value, and the softer is the surface.
5. "Ground CFM" shows the value of the constraint force mixing parameter (CFM) in ODE for ground surface.
6. "Ground Friction" shows the value of the friction parameter for ground material. The higher is the value, and the more friction is the surface.
7. The "run" button lets the model keep moving.
8. The "one step forward" button moves the model one step forward.

Marker data control This sub-panel is to show the motion capture data settings. It allows loading the default motions files as well.

1. "Marker File" is a file dialog that allows users to load the default motions files.
2. "Frame Count" shows the number of frames for the motion capture data. It gives users an intuitive of how long the motion is.
3. "Marker Count" shows the number of markers of the motion capture system used to record the motions.
4. "Start", "Step", "Stop" shows the simulation starts from which frame and ends at which frame. "Step" indicates how many frames of motion data pass within each step of the simulated world.
5. "Current frame" shows the number of the current frame.

6. "Loop" controls whether the simulation should be ended at the last frame or start over from the beginning.
7. The "run" button lets the markers keep moving.
8. The "one step forward" button moves the markers one step forward.

Recall Fig. 5.1, the modeling of body segments and marker data are separated. The markers trajectories can be displayed independently by pressing the "run" button inside the "Marker Data" sub-panel. Press the "run" button inside the "Simulation" sub-panel will let the model body catch up with the current markers' positions. Users can also press the "one step forward" button to observe how the model makes the pose gradually. The big "run" button at the rightmost will simultaneously run the marker data and the simulation process. Fig. 5.7 demonstrates the process that markers run first, and then the model catches up to the markers with the user's operations in the control panel. The green lines represent the links between markers and body segments.

5.2.3 Functional panel

The functional panel provides users a convenient way to interact with the model or adjust the model settings. In addition, there is a vertical menu that allows users to select different functional sub-panels.

Basic functions This sub-panel provides some basic functions.

1. The "plot" button lets the "graph" board show the curves if the sequence of stored angles/torques is not empty.

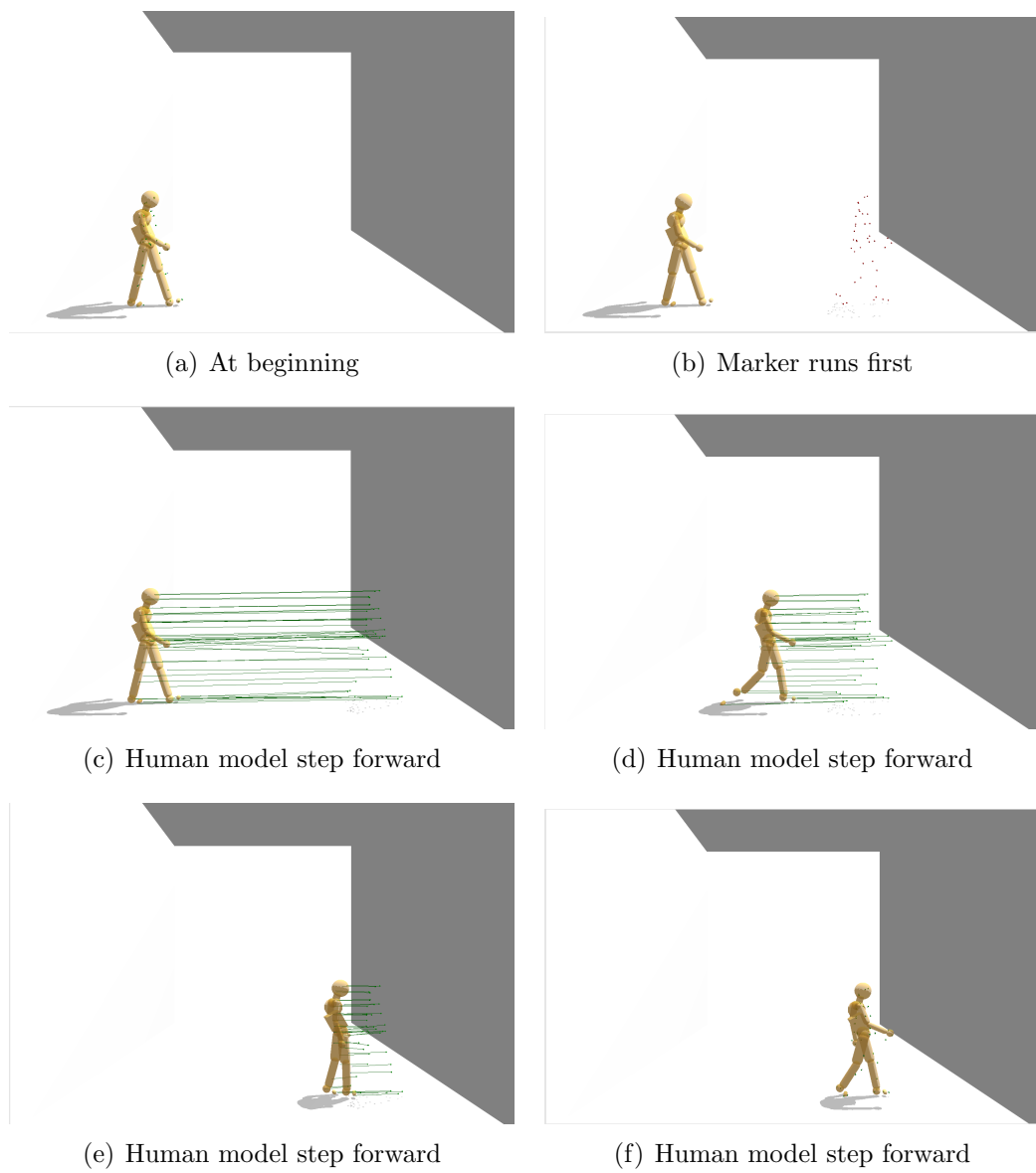


Figure 5.7: An illustration of the control panel

2. The "Save Model Data" button saves the current model body settings to files.
3. The "Clear Saved Angles" button clears all the stored values in the sequence of joint angles.
4. The "Save Model State" saves the current model body state, such as body segment orientations, joint angles, etc., to a file.
5. The "Restore Model State" loads a file of a specific body state to the model.
6. The "Markers" radio button lets the model simulate motions by following markers. The inverse kinematics method was implemented during this round in order to save joint kinematic properties to the related sequences.
7. The "Angle" radio button first detaches all the markers and then lets the model keep moving by using the joint proprieties (joint angles and angular velocities) recorded from the "Marker" round. This forward kinematics process is to check the correctness of the inverse kinematic process.
8. The "Alt Angle" radio button has the same function as the "Angle" radio button, but in this round, the inverse dynamics method will be applied, and the joint torques will be stored in a sequence.
9. The "Run Test" button is designed to integrate the functions of those radio buttons into one button. By pressing this button, the model will first follow the markers to simulate the motions (IK), then simulate the motions only by the computed joint properties (ID), and finally, simulate

the motion just by the calculated joint torques (FD). The last round is to check the correctness of the process of inverse dynamics. If the forward dynamics process successfully uses the computed joint torques, then the inverse dynamics process is correct.

10. The "Stop Test" is to stop the current test.
11. The "Custom Settings" file dialog group allows users to load their custom motion data files and model body settings. Once all the needed files are loaded, press the "Custom" button to show the motion simulation on the display panel. The "Default" button allows users to reset all the settings to default values.

Graph functions The sub-panel works with the "Graph" display sub-panel (Fig. 5.6).

1. The "Save image" allows users to save the image shown on the display board to their local devices.
2. The "joint angle" radio button lets the display show the plots of joints angles.
3. The "joint torque" radio button lets the display shows the plots of joints torques.
4. The "x-axis," "y-axis," and "z-axis" radio buttons allow users to choose the values of which axis to plot.
5. The joint checkbox group allows users to select the desired joints and plot their properties on the display panel. The text next to each checkbox is the joint's name.

Marker functions This sub-panel shown in Fig. 4.1 allows users to modify the marker modeling settings and marker-body mappings manually.

1. The "Connect" button is to attach all the markers to their associated body segments.
2. The "Release" button is to detach all the markers from the dynamic model.
3. The "Update Anchor" button updates the marker-body relative positions based on the current body posture and marker positions.
4. The remaining parts work in this way: (1) The first column represents marker index buttons. Buttons in blue means the corresponding markers are attached to the human dynamic model. Users can attach/detach markers by clicking index buttons. (2) The second column shows body segments where markers are attached. Each spin box is a collective item of all body segment names. Users can use it to change the body-marker attachment relationship. (3) The three-five columns present the marker-body relative positions. Users can modify the values directly using this interface.

Joint functions This sub-panel (shown in Fig. 5.8 (a)) allows users to adjust the joint constraints limitation through the user interface and visualize the effects. The pairs of values for each joint are the range of torques a joint can apply. "Root X" and "Root Y" indicate the translation values of the linear motor of the residual joint along x and y axes, while "Pitch", "Roll" and "Yaw" represent the rotating values of its angular moto along x, y, and z axes.

The "Zero" button is to fill all max values with 0 Nm. The "Light" button is to fill the max values of the first six joints with 0 and all remaining max values with 50 Nm. The "Strong" button is to fill all max values with 9999.

Dimension functions This sub-panel allows users to directly adjust the body segments' size base on the motion capture data through the user interface. The panel shown in Fig. 5.8 (b) includes the names of body segments and their dimensions. If the body's shape is a sphere, its name is followed by "Rad", and the value next to it represents the radius of the sphere. For box shapes, its name appears three times, followed by x, y, z, and the values next to them indicated the edge lengths along x, y, z axes in its local coordinate. For Capsule shapes, its name appears twice, followed by "Rad" and "len", which indicate the radius and the length of the Capsule, respectively. Notice that the "len" does not include the "radius", which means the real size of the Capsule is "len" plus two "radius".

The shapes and dimensions of body segments are shown in Fig. 5.9. For example, the "RLO_ARM_body, Capsule, radius and length" means the shape of the right lower arm is a capsule, and its dimension includes radius and length. Their values should be pre-defined by users. Similarly, users need to assign the radius values for spheres and the length, width, height for boxes.

5.3 Summary

The user interface is a multi-purpose graphical interface that allows users to control the human model to simulate and analyze motion capture data. It immensely simplifies the procedures of utilizing the human dynamic model for

Zero
Light
Strong

RootX 0.00 0.00
RootY 0.00 0.00
Pitch 0.00 0.00
Roll 0.00 0.00
Yaw 0.00 0.00
ChinX 0.00 0.00
ChinY 0.00 50.00
ChinZ 0.00 50.00
NeckX 0.00 50.00
NeckY 0.00 50.00
NeckZ 0.00 50.00
R.CollarX 0.00 50.00
R.CollarY 0.00 50.00
R.CollarZ 0.00 50.00
R.ShoulderX 0.00 50.00
R.ShoulderY 0.00 50.00
R.ShoulderZ 0.00 50.00
R.ElbowX 0.00 50.00
R.ElbowZ 0.00 50.00
R.WristX 0.00 50.00
R.WristY 0.00 50.00
L.CollarX 0.00 50.00

☐ Body Rel
Head Rad 0.260
Neck X 0.090
Neck Y 0.090
Neck Z 0.100
UpTorso Rad 0.270
UpTorso Len 0.320
R.Collar Rad 0.120
R.Collar Len 0.180
R.UpArm Rad 0.100
R.UpArm Len 0.340
R.LoArm Rad 0.080
R.LoArm Len 0.320
R.Hand Rad 0.110
L.Collar Rad 0.120
L.Collar Len 0.180
L.UpArm Rad 0.100
L.UpArm Len 0.340
L.LoArm Rad 0.080
L.LoArm Len 0.320
L.Hand Rad 0.110
LoTorso X 0.260
LoTorso Y 0.210
LoTorso Z 0.260

(a) Joint sub-panel

(b) Dimension sub-panel

Figure 5.8: The Joint sub-panel and the Dimension sub-panel

motion analysis. Through this tool, users can easily load motion capture files, modify the mapping relationships between markers and body segments, adjust the model body size and parameters values and plot the results of kinematic and dynamics analysis. When using the user interface, the following points need to pay attention to:

1. The system supports uploading motion files in C3D and CVS formats. For the CVS motion files, its format of content should refer to the sample shown in Fig. 5.4 (a).
2. For motion files with other formats, such as MAT file, users can easily convert MAT files to CSV files and then load them to the system.
3. When using the motion files from the CMU motion capture database, users do not need to concern the fittings between model body and marker data for most cases.
4. For custom motions, users are required to fit the model to motion capture data properly, e.g., assign markers to appropriate body segments, as the model configuration does affect the results of motion analysis.

Improvement of the dynamic human model The existing forty-eight degree of freedoms dynamic human has been improved in the following ways:

1. The original model can deal with the motion capture data set of C3D⁴ format that is the biomechanics standard file format. However, CSV files are also commonly used for storing motion capture information. Besides, mocap files with other formats, such as MAT files, can be easily

⁴<https://www.c3d.org/>

converted to CSV files. Therefore, we extended the system so that it can work with both C3D files and CSV files.

2. We reorganized the whole system to classify motions into two categories: default motions and custom motions. Users can load different kinds of motions through different sub-panels on the user interface.
3. The original model needs to match the markers and their corresponding body segments manually. The new system can automatically achieve this process as long as using the motions from the CMU motion capture database.
4. The user interface now can directly show the analysis results of joints properties on the display panel. In addition, users can manipulate the graphs using the functional panel. It also supports users directly modifying the image titles/frames labels or scaling the view of the image through the interface based on specific requirements.
5. We rewrite parts of the codes to eliminate code redundancy. As a result, the source code is cleaner and more readable. The system is now user-friendly and can be used as a standard analyzing tool for human movement [61].

Human Dynamic Model -- Body Segments			
Index	Body Name	Shape	Dimension
0	HEAD_BODY	Sphere	radius
1	NECK_BODY	Box	length, width, height
2	UP_TORSO_BODY	Capsule	radius, length
3	R_COLLAR_BODY	Capsule	radius, length
4	RUP_ARM_BODY	Capsule	radius, length
5	RLO_ARM_BODY	Capsule	radius, length
6	R_HAND_BODY	Sphere	radius
7	L_COLLAR_BODY	Capsule	radius, length
8	LUP_ARM_BODY	Capsule	radius, length
9	LLO_ARM_BODY	Capsule	radius, length
10	L_HAND_BODY	Sphere	radius
11	LO_TORSO_BODY	Box	length, width, height
12	WAIST_BODY	Capsule	radius, length
13	RUP_LEG_BODY	Capsule	radius, length
14	RLO_LEG_BODY	Capsule	radius, length
15	R_HEEL_BODY	Sphere	radius
16	R_TARSAL_BODY	Capsule	radius, length
17	LUP_LEG_BODY	Capsule	radius, length
18	LLO_LEG_BODY	Capsule	radius, length
19	L_HEEL_BODY	Sphere	radius
20	L_TARSAL_BODY	Capsule	radius, length

Figure 5.9: The shapes and dimensions of body segments.

Chapter 6

Energy Cost in Virtual Tracing Tasks¹

Humans have elegant bodies that allow gymnastics, piano playing, and tool use, but understanding how they do this in detail is difficult because their musculoskeletal systems are extraordinarily complicated. Nonetheless, although movements can be very individuated, some everyday movements like walking and reaching can be stereotypical, with the movement cost a major factor. Chapter 3 has extended these observations by showing that in an arbitrary set of whole-body movements used to trace large-scale closed curves, near-identical posture changes were chosen across different subjects, both in the average trajectories of the body's limbs and in variations within trajectories. The commonality of that result motivates explanations for this generality. Our thesis was that humans might choose trajectories that are economical in en-

¹The work described in this chapter was published as a preprint paper in bioRxiv by Liu et al [60]. I conducted this experiment, with much help from Dana Ballard and Mary Hayhoe.

ergetic cost. This chapter describes how we test this hypothesis. We situate the tracing data within a fifty degree of freedom dynamic model of the human skeleton that allows the computation of movement cost. Comparing the model movement cost data from nominal tracings against various perturbed tracings shows that the latter are more energetically expensive, inferring that the original traces were chosen based on minimum cost. Moreover, the computational approach used to establish the minimum cost principle suggests a refinement of what is known about cortical movement representations.

6.1 Methods

6.1.1 Virtual tracing experiment

For the original kinematic data capture, we designed a virtual whole-body tracing experiment to elicit natural movements under common goals [62]. It has been described in detail in Chapter 3. Fig 3.1 shows the virtual environment setup. Fig 3.2 shows the nine paths that subjects traced. In this chapter, we reordered the nine curves based on their complexity (curve length) and renamed them, which are shown in Fig. 6.1.

Data post-processing In addition to the data interpolation process described in Chapter 3, if a participant did not trace the path successfully, we would consider this tracing invalid and unusable. Because if a recording of a tracing trial failed, e.g., too many markers were off during a tracing, it will lead to extremely large joint torques, which is unrealistic.

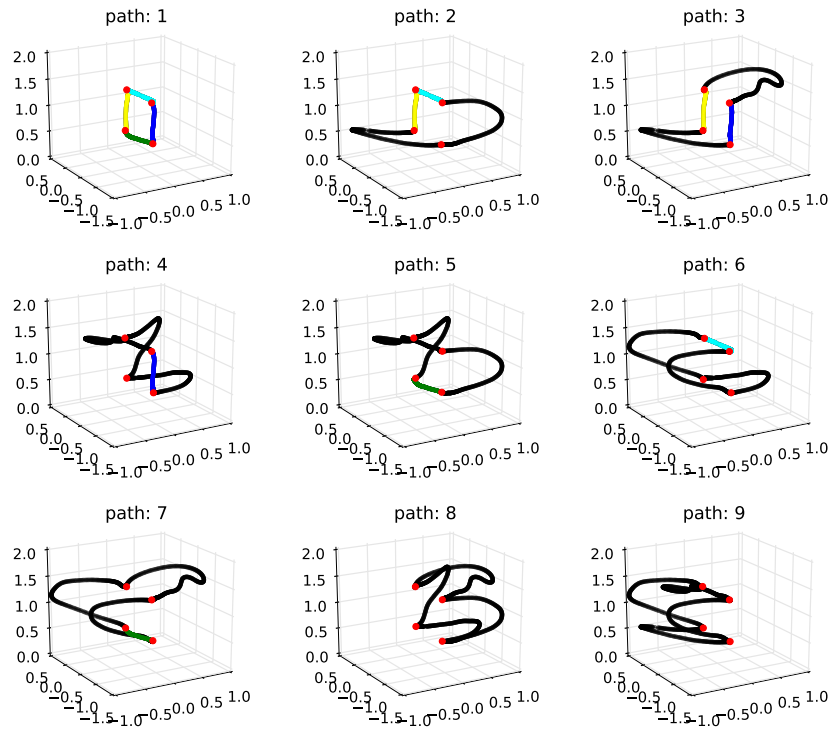


Figure 6.1: The nine 3-dimensional paths in the virtual environment that were used in the experiment. They are ordered by their complexity. For reference, colors denote common segments and points. For the subjects, the paths were all rendered in black. The scale is in meters.

6.1.2 Human dynamic model

To compute the energy cost of subjects tracing paths, we used a human dynamic model describe in Chapter 4 and Chapter 5. Its topology and user interface are shown in Fig. 4.3 and Fig. 5.5. Fig 6.2 shows four stages in a tracing sequence made originally by a participant of the virtual tracing experiment and recreated by applying the inverse dynamics method using this tool. By replaying the virtual tracing experiment’s kinematic data, we can compute the joints’ torques and angles at each frame. As mentioned in Chapter 4, instantaneous power was computed from the product of net joint torque and joint angular velocity at each frame. The work performed at each joint was determined by numerically integrating the instantaneous powers over the entire tracing task. In this way, the energy cost of human motions can be computed given motion capture data.

Residual forces/torques The energetic costs are derived from the inverse dynamics technique described in [61], which combines measured kinematics and external forces to calculate net joint torques in a rigid body linked segment model. A feature of the dynamic method is that it can reduce potential errors, both in the matches of the motion capture suit and the model. Analogous to the human body’s ligament structure to join joints, some leeway is allowed in the model joints in the integration process. Nonetheless, even after these adjustments, some errors remain. In the model, the main source of the residual forces is usually attributable inaccuracies in the matches between the motion capture suit makers and their match with their corresponding points on the model. It is commonly resolved by introducing ‘residual forces,’ which compensate for this problem [27]. This resolution with a dichotomy of forces is

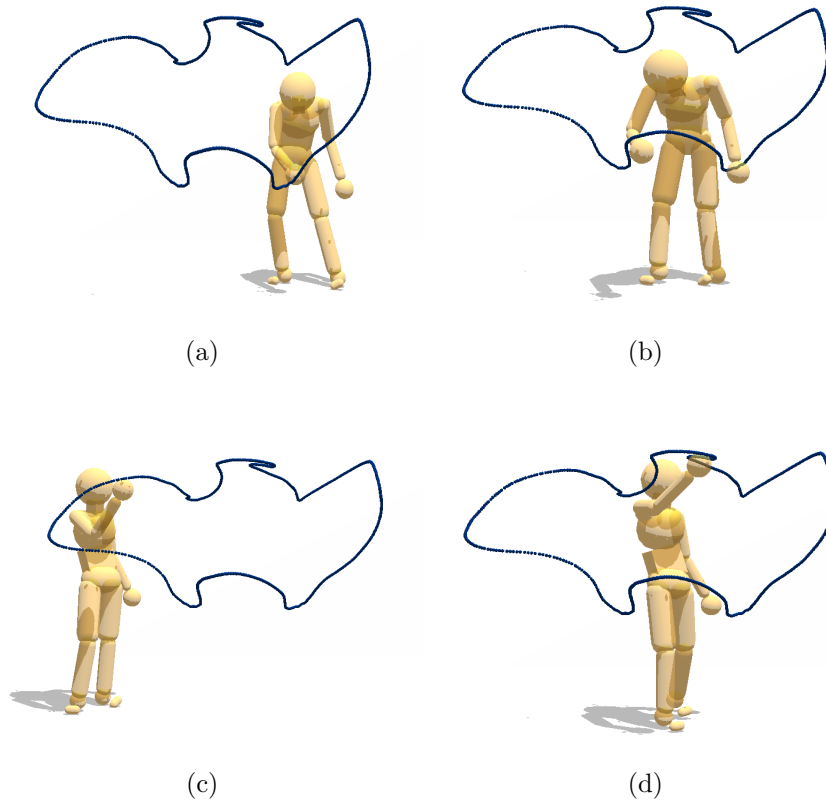


Figure 6.2: Model capability illustration. Four points in a tracing sequence reproduced with physics-engine-based inverse dynamics using recorded motion capture data from a human subject.

analogous to the human system, which combines feedforward lateral pathway forces with medial pathway feedback forces. Therefore, a low cost in residual forces usually implies that the dynamic model is a good match for that subject's kinematic data.

6.1.3 Energy cost computation

The centerpiece of the analysis depends critically on the definition of a posture. At each frame, posture is defined as a vector of the joint torques and angles of each of N joints ($N = 22$ in our dynamic human model). The posture p at a frame is a 6n-dimensional column vector presenting the joints properties of the i th participant, thus:

$$\mathbf{p} = [\mathbf{j}_1, \mathbf{j}_2, \dots, \mathbf{j}_N] \quad (6.1)$$

$$\mathbf{j}_i = (\boldsymbol{\tau}_i, \theta_i) \quad (6.2)$$

where $\boldsymbol{\tau}_i = (\tau_{i_x}, \tau_{i_y}, \tau_{i_z})$ and $\theta_i = (\theta_{i_x}, \theta_{i_y}, \theta_{i_z})$ represents the torques and angles of the i th joint at a frame respectively and $i = 1, 2, \dots, N$. For the joints which have less than three dimensions, e.g. hinge joints, universal Joints, the values at unused dimension were assigned zero.

The power W of i th joint at a frame t is a scalar and equals to the inner product of its torque $\boldsymbol{\tau}_i$ and its angular velocity $\boldsymbol{\omega}_i$, thus:

$$\boldsymbol{\omega}_i(t) = \theta_i(t) - \theta_i(t - 1) \quad (6.3)$$

$$W_i(t) = \boldsymbol{\tau}_i(t) \cdot \boldsymbol{\omega}_i(t) \quad (6.4)$$

Therefore the power of a posture at frame t is presented as:

$$W(t) = \sum_{i=1}^N W_i(t)$$

Assuming it takes a participant T frames to trace a path, then the total energy cost E of the participant tracing a path is:

$$E = \sum_{t=1}^T W(t)$$

The energy cost analysis is naturally organized into three separate stages. Initially, we analyze the subjects' energy cost and residual torques of tracing path 1. Next, we computed the tracing cost of all nine paths. To compare the energy cost of tracing a path across subjects, we computed the average energy cost for all five repeated traces of each subject. Finally, we measured the tracing cost of perturbed participant's trajectories and perturbed paths.

6.2 Results

Using the kinematic data from Chapter 3, we fitted the dynamic model to each of the eighteen subjects and then had the models trace the nine curves shown in Fig. 6.1. The energy cost of tracing paths showed marked regularities in the following aspects of the data that was subject to analysis:

1. The joints' power allocation while tracing path 1 across different subjects showed that although the total costs of the movements varied between subjects, the power use is qualitatively very similar. (See section 6.2.1,

Figure 6.3);

2. The computation of average energy cost while tracing path 1 showed that the magnitude of the required residual forces was relatively small. (See section 6.2.1, Figure 6.4 and Figure ??);
3. The costs of tracing each path by each subject are very similar and approximately monotonic with the length of paths. (See section 6.2.2 and Figure 6.5);
4. Although there are variations in the cost across the repeated traces, using the perturbed model parameters is significantly higher than the original. (See See section 6.2.2, Figure 6.6 and Figure 6.7);
5. The increment of energy cost while using perturbed model parameters distributes more on the joints' cost than on the residual component. (See section 6.2.2 and Figure 6.8);

6.2.1 Detailed Energetic cost analysis of tracing path 1

The mean of power across different participants As an initial analysis, we established the variations in the energetic costs for tracing path 1 exhibited by different subjects. Fig. 6.3 illustrates the mean and the standard deviation of powers across subjects at each frame. The result reveals that subjects put similar effort at the same points along the path. Thus although the total cost of the movements may vary between subjects, the power patterns are qualitatively very similar. Furthermore, the virtual reality tracing experiment in chapter 3 showed that participants used similar postures sequences while tracing the same curves from a kinematic perspective. It is expected that

the instantaneous power of joints at each frame should be similar due to the human body's skeleton constraints. The similarity of power patterns across different subjects reinforces this conclusion from a dynamics perspective.

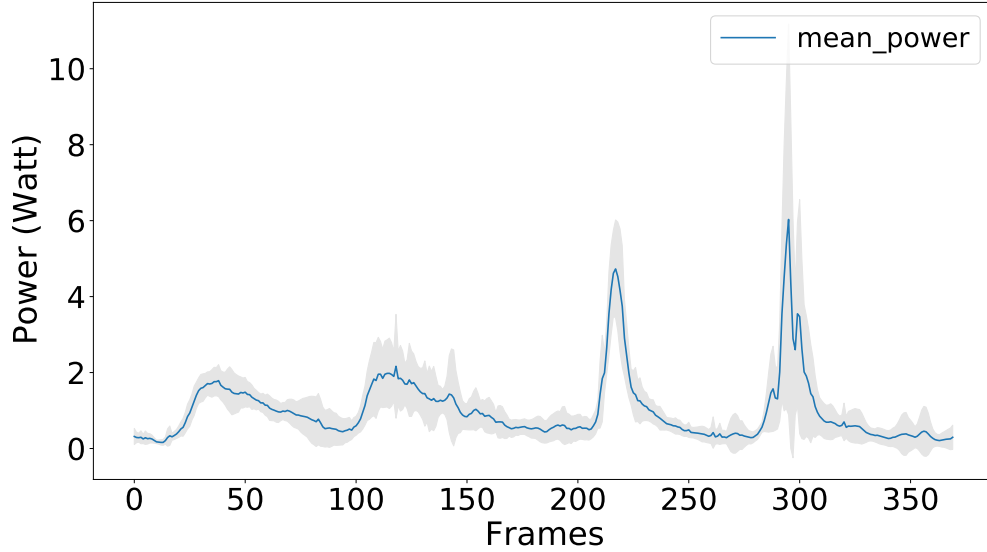


Figure 6.3: The power of tracing path 1 at each frame. Nine subjects traced path 1 five times. The plot shows the average joints' power at each frame across subjects. The blue line indicates the mean, and the gray shaded area represents the standard deviation of powers. The small standard deviation means that different subjects had similar power patterns while tracing the same curve, which shows that the curve has points of difficulty in tracing shared by the subjects. Path 1 is the most straightforward, but the observation of correlated effort represents patterns in tracing other curves.

Average energy cost of five repetitions Although there are qualitative similarities in the difficult points on the curve, the total costs of the traces differ across different subjects. This result is expected due to the variety of subjects' skeletons and weights. Fig. 6.4 represents the energetic cost per subject. The

total energy of tracing a path 1, including the residual components, is shown in blue, and the residual component is shown separately in orange. When reporting the energetic costs of the traces, we always use the total cost shown here in blue.

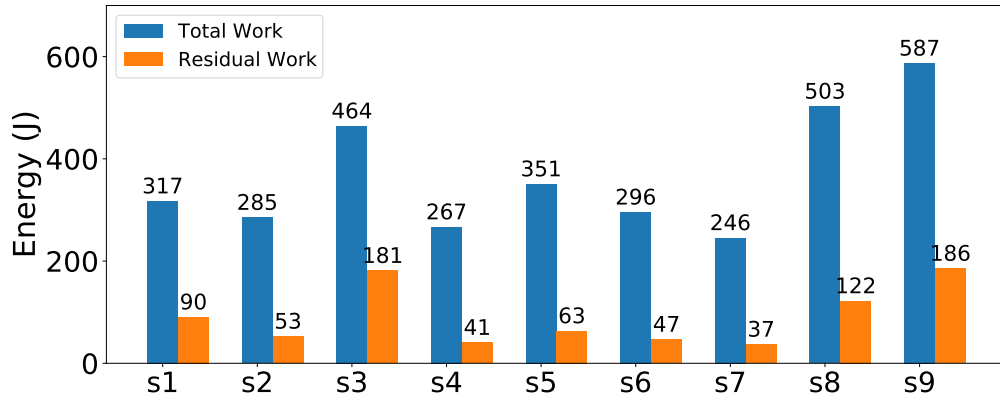


Figure 6.4: Energetic costs of tracing path 1. Each subject traced path 1 with five repeats. The horizontal labels indicate the related subjects, e.g., "S1" represents the subject1. The total cost is shown in blue, and the portion of the cost due to residual forces are shown in orange. A low cost in residual forces usually signifies that the dynamic model matches that subject's kinematic data.

Residual forces As shown in Fig. 6.4, the highest cost of the tracing movement is the component owing to the joint torques that are producing the kinetic trajectories and the additional cost of the residual from the inverse dynamic calculation is small. In the human system, this residual is most prominently due to the vestibular system, but just how the vestibular connects to the muscular system is not modeled by the human dynamic model. Instead, we implemented a provisional system of torques referred to as a coordinate system

positioned and the center of mass to maintain balance in Chapter4.

6.2.2 Energy cost analysis of tracing individual paths

Energy cost of tracing nine paths Although there are similar energetic costs per subject in tracing an identical path, this arrangement does not carry over to the comparison between paths, which has larger differences. We hypothesized that the cost should scale as the length of the path, as shown in Fig. 6.5, which shows the average energetic cost of tracing the nine different paths. The paths differ in tracing cost, but the costs of tracing each path by each subject are very similar and approximately monotonic with the length of the paths.

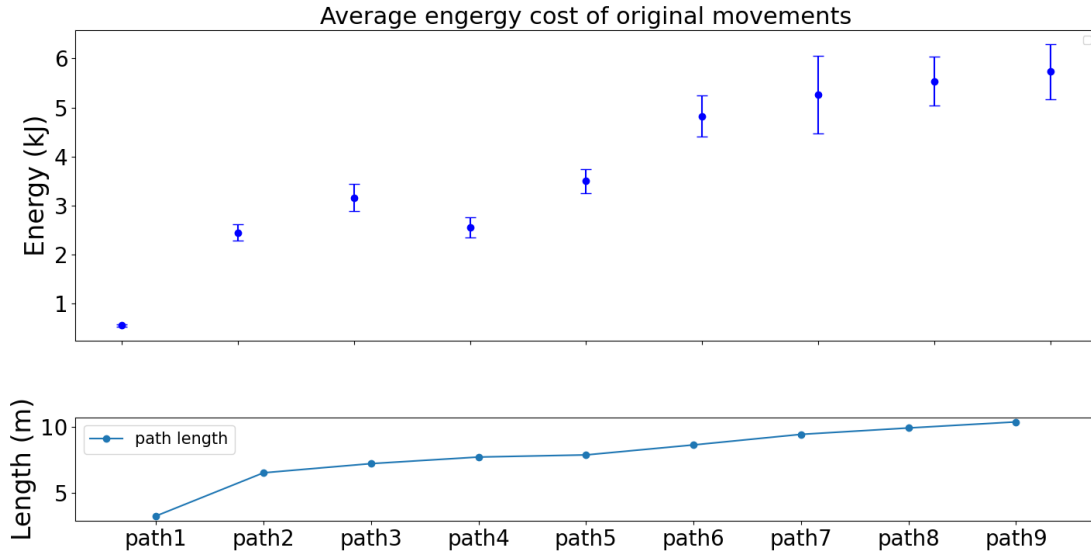


Figure 6.5: The energetic cost of tracing nine paths. These results portray the possibility that the costs vary across the best-fit five subjects. The statistics show that each path traced has a unique cost that distinguishes it from the rest.

Given these regularities, the next step was to evaluate the significance of perturbations in the tracing protocol. The hypothesis is that if the tracing postures are chosen to be of minimum energy, changing the configuration away from the actual tracing situation should incur a cost, which was what happened.

Model perturbation The first perturbation test changed in model marker trajectories, called model perturbation. Specifically, the right-elbow marker was shifted by a small delta, which produced a new constraint that the model needed to satisfy while tracing paths. To implement it, the dynamic model had to trace paths using identical posture sequences except for lifting its right elbow. Although kinematics of the body parts except the right elbow remained for the unperturbed trace – only the kinematics of the right elbow changed, the joints’ constraints bias the dynamic model adapt to follow the new perturbed trace.

For each trace, the right-elbow marker was raised by 5 cm. The rest of the system adapted the way dictated by the dynamic constraints. Fig. 6.6 shows the difference in cost of constrained motions and original motions. It is seen that although there are variations in the cost across the repeated traces, the cost of using the perturbed model is higher than the original. Note that outside of the changes, the rest of the model solves the inverse dynamic model with the unperturbed parameters, and thus the model has substantial degrees of freedom at its proposal. The significant test showed the difference is reliable, with a p-value less than 0.001. Furthermore, the increase of tracing complex paths is larger than that of tracing simple paths.

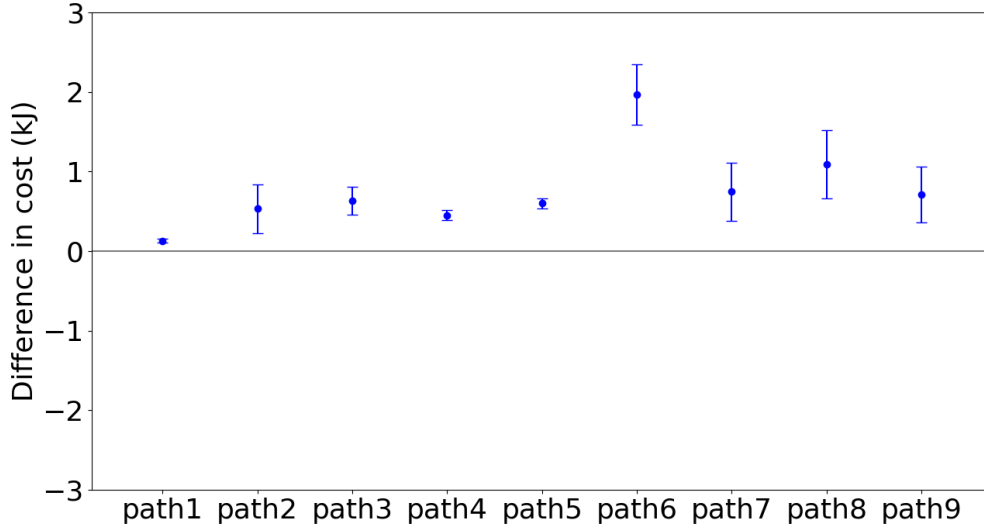


Figure 6.6: The difference in the energetic cost for the model perturbation. The figure shows the difference in the energetic cost of tracing each of the nine paths with perturbations in the right-elbow marker. The elbow was moved up 5cm. The results show that the original path is always the least expensive for all the paths and the averages across subject tracers. Moreover, the differences between the energetic costs of original trajectories and perturbed trajectories are highly significant, with a p-value less than 0.001.

Path perturbation The second perturbation test made adjustments in the traced path, called path perturbation. Some effects of displacement can be intuited. For example, if a subject has to reach over their head during the trace, it can be expected that lowering the traced path would result in cost savings. For this reason, we chose path perturbations in the horizontal plane. Two such perturbations were used: a 5-centimeter leftward displacement and a 5-centimeter rightward displacement. Left and right are referenced to the coordinate system used for the four points used for all nine curves (See Fig 6.1).

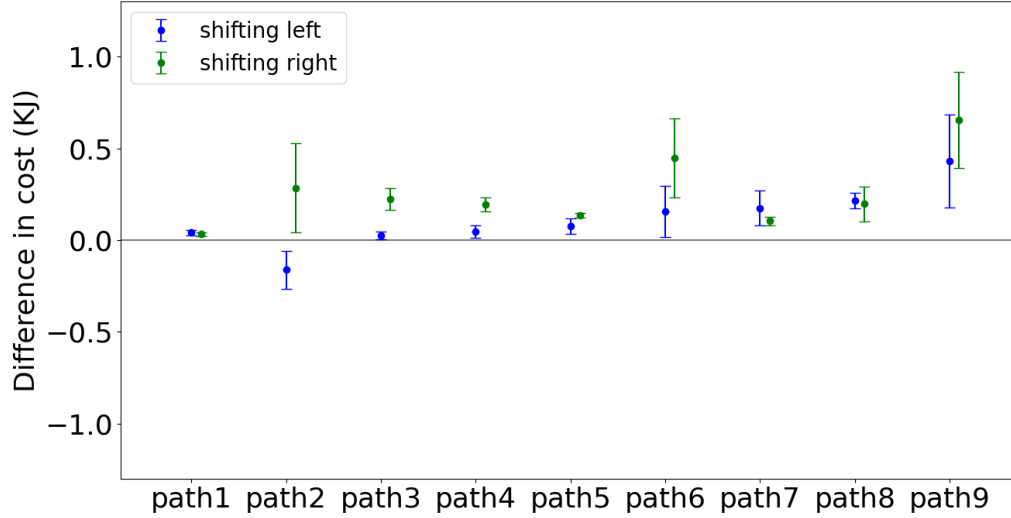


Figure 6.7: The difference in the energetic cost for the path perturbation. Each of the nine paths has two perturbations of 5 cm: left in blue, right in green. This main result shows that the original path is always the least expensive for both averages across subject traces. The difference in the energetic cost for the path perturbation is not very clear but still reliable, with a p-value less than 0.01.

In this way, new constraints were produced as the dynamic model was required to trace the perturbed paths while the starting tracing positions were not changed. In contrast to the model perturbation, the model's trace paths were shifted while the posture sequences remain the same. Again, the dynamic model took advantage of internal joint constraints to adjust original posture sequences to trace the perturbed paths.

Figure 6.7 shows the difference in average energetic costs for tracing displaced paths and original paths across subjects. The blue dots indicate the difference between tracing left-shifted paths and tracing the original path,

while the green dots represent the other case. For most cases, the original paths are seen to be consistent with the lowest cost. Path 2 with 5cm leftward displacement costs less than the original path 2. The reason is that subjects preferred to stand near the left corner, where is the starting tracing position. However, the left part of path 2 is much easier than its right part (See Fig. 6.1). Therefore, when shifting path 2 to the left, subjects became closer to the right part, which led to easier tracing. In contrast, subjects had to move their bodies more in order to trace well when shifting path 2 to the right.

Here again, the overall result is striking. Although there are some overlaps, the original paths are more economical for almost all curves than the displacements. The significant test showed the effects of shifting paths is not very clear but still reliable, with a p-value less than 0.01. The observation that the averages of all the perturbed costs are larger than the average cost of their original progenitors strongly suggests that energy cost is the factor in the choice of tracing postures.

Residual forces Given the dynamics dichotomy, a natural question that arises concerns the magnitude of the extra torques in the perturbation cases. Are the extra costs carried by the dynamic model or the residual? It can be answered by interrogating the simulation, and it turns out that the dynamics model's contribution is dominating. This is shown in Fig 6.8.

Note that if the constraints on the dynamics were highly stiff, then the model would have no course other than tracing an exact copy of the unperturbed trajectory and let the residual torques contribute the needed difference. However, the markers on the body for these experiments were limited to 15~18 of key body segments, leaving the extra degrees of freedom to be determined

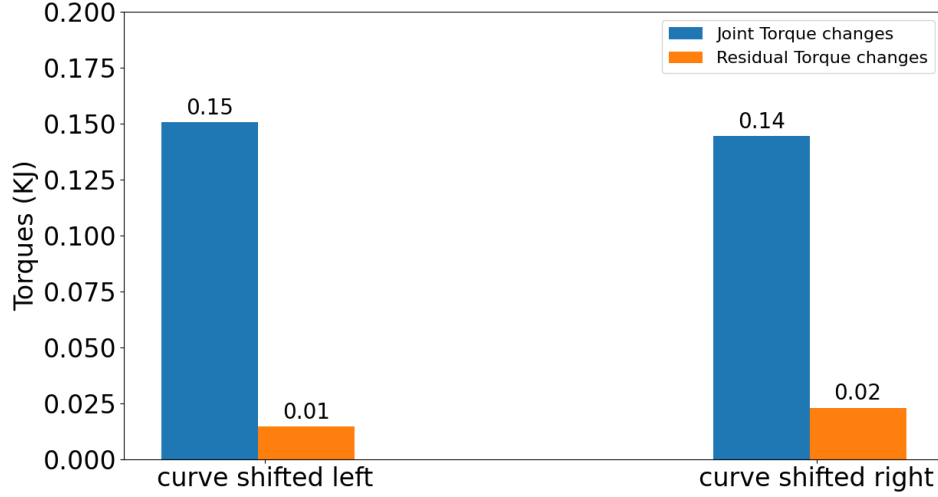


Figure 6.8: The residual torques The average of the means of the cost changes for nine paths with five repeats across five participants.

by the dynamics. Moreover, the torque computation, to model the reality of muscles [36], used spring constraints at each joint degree of freedom. Finally, the right finger was required to contact the displaced paths, and the remaining features of the movement are the same, leaving the dynamics to fill in the rest.

6.3 Discussion

Given that the cost of the movements is a significant fraction of a human's caloric budget [78], one might expect that humans would exhibit common low-cost postures. It turns out to be the case for stereotypical situations such as reaching or walking on a planar surface, but arbitrary whole-body movements have been less studied, so the expectations are open. Thus it was

a surprise to measure arbitrary movements in a large-scale tracing task and find markedly common posture sequences used by all tested subjects [62]. An obvious possibility for similar posture sequences is energetic cost, especially since there were no complex constraints in the movements and no constraints in the time to perform the traces. Our simulation extends the kinematic finding to show that tests of human dynamics provide evidence that movements are chosen on the basis of energetic economic costs. The cost of tracing scales monotonically with the length of a traced path as expected, and the necessary residual forces, as would be expected from the human’s vestibular system and others, were relatively small, given that the subjects had to choose their movements.

The main substantive results are that subjects’ traces of each of nine space paths all have minimal costs with respect to local perturbations. One manipulation introduced perturbations in their kinematic variables – the subjects traced the path but their model with small displacements in kinematic markers. The other experiment used local horizontal displacements of the paths. Verticals were not used as they can be equivocal. The displacements can interact with the different body heights, e.g., a short subject has to reach an uncomfortable height. However, outside of this caveat, all the data can be interpreted as the tracing posture sequences selected based on energetic cost.

The hypothesis that humans use minimum cost movement trajectories is shown by the use of a human dynamic model that leverages a significant innovation in dynamics computation that allows the recovery of torques from kinematic data. The disadvantage of the current method is that we perturbed motions manually, so it is possible that we found only a local minimum in the space of possible movements. However, as tracing a path usually takes more

than 1000 frames, and 50 markers represent a posture at each frame, the perturbation space is significantly vast. Therefore, our future work is to introduce an algorithm with the capability of seeking potential perturbations automatically, such as reinforcement learning, while still reflecting the constraints of possible postures.

Chapter 7

Muscle Co-contraction Detection

The previous chapters describe a research project that includes a virtual-reality experiment to elicit kinematics regularity of whole-body human movements given a common goal and a physical human dynamic model system used for analyzing dynamics regularity during the virtual tracing experiments. As the whole-body motion capture data collected in the virtual experiment is valuable for studying human movement in the motor control or biomechanics area, it is worth conducting some extended studies related to this research project. One of them is the analysis of movement variations as a correlation of muscle stiffness which implies muscle co-contraction. This ability was neglected in the previous chapter by assuming that it was the same in the compared curves.

Co-contraction is notoriously challenging to study, but we show tentative progress here with the study of detecting muscle co-contraction using the sliding window Gaussian process method that detects oscillations in the

local kinematics. Muscle co-contraction occurs when two muscle groups (agonist and antagonist) surround a joint contract simultaneously to stabilize one's limbs. It can be detected and measured using electromyography (EMG) by attaching electrodes to participants' skin while performing tasks. Muscle contraction is believed to play an essential role in joint stabilization and the general mechanism. However, the general mechanism of it is still widely unknown. Furthermore, the EMG method is inconvenient and time-consuming. These facts motivate the creation of an alternative approach to detect muscle contraction in a much easier way. The scientific question here is whether a Gaussian process can determine the state of muscle co-contraction as revealed in a correlation with kernel parameters used to fit tracing data. In this chapter, a sliding window Gaussian process was implemented to detect potential muscle contraction.

7.1 Muscle Co-contraction

Muscle co-contraction helps the nervous system to adapt the mechanical properties of the limbs to satisfy specific task requirements — both in statics and dynamics [33]. Previous reaches studied possible relationships between muscle contraction and movement properties in multi-joint limb movements. For example, [33] studied the contraction of elbow muscles when participants were attempting to point to targets of varied random sizes in a horizontal plane. The results showed that as target size was reduced, muscle contraction activity increased. Besides, trajectories variability decreased and endpoint accuracy improved. Another study [80] showed that arm stiffness increases while muscle con-contraction increases, which leads to fewer trajectories variability. It has

also been studied that muscle co-contraction is related to movement velocity [76, 77, 88, 67], e.g., it is increased with gait speed during walking tasks for older adults, but not for young adults. According to previous research, we hypothesize that a sliding window Gaussian processes fitting on specific coordinates may detect muscle co-contraction, which could be embodied in the changes of parameters' values of Gaussian kernel within each window, as this method could potentially encode changes in velocity and direction for a movement.

7.2 Gaussian Process

A Gaussian processes model is a probability distribution over possible functions that fit a set of points [106]. Formally, a Gaussian process generates data located in a particular domain so that all the finite subsets of the range sample from a multivariate Gaussian distribution [109]. Given training data pairs (x, y) , each observation y is defined as relevant to an underlying function $f(x)$ via a Gaussian noise model:

$$y = f(x) + \mathcal{N}(0, \sigma_n^2) \quad (7.1)$$

where where $\mathcal{N}(0, \sigma_n^2)$ is Gaussian distributed noise. The Gaussian process regression is the search for $f(x)$:

$$f(x) \sim GP(\mu, K) \quad (7.2)$$

$$p(f|X) = \mathcal{N}(f|\mu, K) \quad (7.3)$$

where $\mu = \text{mean}(x)$ and $K_{ij} = k(x_i, x_j)$. μ is the mean function which usually sets to be zero. $k(x_i, x_j)$ is the covariance function, also called the kernel function. We used the squared-exponential covariance function, also known as the radial basis function (RBF):

$$k(x_i, x_j) = \sigma_f^2 \exp\left[-\frac{(x_i - x_j)^2}{2l^2}\right] + \sigma_n^2 \delta \quad (7.4)$$

where σ_f , l and σ_n are hyperparameters. σ_f describes how much vertically the function can span, which refers to the signal variance. If the $x_i \approx x_j$, $k(x_i, x_j)$ approaches its maximum σ_f^2 , meaning $f(x_i)$ is perfectly correlated with $f(x_j)$: $f(x_i) \approx f(x_j)$. In contrast, if the x_i is far from x_j , then $k(x_i, x_j) \approx 0$, meaning $f(x_i)$ is independent of $f(x_j)$: $f(x_i)$ and $f(x_j)$ are completely different. The attributes force the regression function to be smooth, neighbors' values must be similar. The horizontal scale l indicates how quickly the correlation relationship between two points decreases as their distance increases, and σ_n is the noise variance. As mentioned in [106], the model will be under-fitting if σ_f is too large, while it would be over-fitting if the value of σ_f is too small. So the procedure of hyperparameters optimization is needed while using Gaussian process method.

Given a training set (\mathbf{X}, \mathbf{y}) where $\mathbf{X} \in \mathbb{R}^{n \times m}$ and $\mathbf{y} \in \mathbb{R}^m$. n is the number of features of one input x_i and m is the number of training data. In GP modeling, the data can be considered as samples from a multivariate

Gaussian distribution. For the expected value y_* , we can have:

$$\begin{bmatrix} \mathbf{y} \\ \mathbf{y}_* \end{bmatrix} \approx \mathcal{N}\left(\begin{bmatrix} \boldsymbol{\mu} \\ \boldsymbol{\mu}_* \end{bmatrix}, \begin{bmatrix} \mathbf{K} & \mathbf{K}_* \\ \mathbf{K}_*^T & \mathbf{K}_{**} \end{bmatrix}\right) \quad (7.5)$$

$$p(\mathbf{y}_* | \mathbf{X}_*, \mathbf{X}, \mathbf{y}) = \mathcal{N}(\mathbf{y}_* | \boldsymbol{\mu}, \Sigma) \quad (7.6)$$

where $\mathbf{K} = \mathbf{K}(\mathbf{X}, \mathbf{X})$, $\mathbf{K}_* = \mathbf{K}(\mathbf{X}, \mathbf{X}_*)$, $\mathbf{K}_{**} = \mathbf{K}(\mathbf{X}_*, \mathbf{X}_*)$, $\begin{bmatrix} \boldsymbol{\mu} \\ \boldsymbol{\mu}_* \end{bmatrix} = \mathbf{0}$, $\boldsymbol{\mu} = \mathbf{K}_*^T \mathbf{K}^{-1} \mathbf{y}$ and $\Sigma = \mathbf{K}_{**} - \mathbf{K}_*^T \mathbf{K}^{-1} \mathbf{K}_*$.

With Gaussian noise with variance σ_n^2 , the expression becomes:

$$\begin{bmatrix} \mathbf{y} \\ \mathbf{y}_* \end{bmatrix} \approx \mathcal{N}\left(\begin{bmatrix} \boldsymbol{\mu} \\ \boldsymbol{\mu}_* \end{bmatrix}, \begin{bmatrix} \mathbf{K} + \sigma_n^2 \mathbf{I} & \mathbf{K}_* \\ \mathbf{K}_*^T & \mathbf{K}_{**} \end{bmatrix}\right) \quad (7.7)$$

Therefore, the general algorithm for Gaussian process regression can be summarized as follows:

Algorithm 1: Gaussian Process

Input : Training data (\mathbf{X}, \mathbf{y}) , test input \mathbf{X}_* , kernel function \mathbf{K} , \mathbf{K}_* , \mathbf{K}_{**} , and noise level σ_n^2

Output: The mean prediction $\boldsymbol{\mu}_*$, the variance of prediction Σ , and the marginal log likelihood $\log p(\mathbf{y} | \mathbf{X})$

1 $L = \text{Cholesky}(\mathbf{K} + \sigma_n^2 \mathbf{I})$

2 $\boldsymbol{\alpha} = L^T (\mathbf{L} \mathbf{y})$

3 $\boldsymbol{\mu}_* = \mathbf{K}_*^T \boldsymbol{\alpha}$

4 $\boldsymbol{\nu} = \mathbf{L} \mathbf{K}_*$

5 $\Sigma = \mathbf{K}_{**} - \boldsymbol{\nu}^T \boldsymbol{\nu}$

6 $\log p(\mathbf{y} | \mathbf{X}) = -\frac{1}{2} \mathbf{y}^T \boldsymbol{\alpha} - \sum_{i=1}^m \log L_{ii} - \frac{n}{2} \log 2\pi$

As shown in the algorithm 1, the Cholesky decomposition is used to

get the lower triangular matrix \mathbf{L} where $\mathbf{LL}^T = \mathbf{K}$, which is more numerically stable than the matrix inversion. It also provides a simple way to calculate the second term in the marginal log-likelihood. The shortness of using the Cholesky decomposition algorithm is the computational complexity $O(n^3)$. However, it will not be an issue for our small training data set. For the hyperparameters optimization, it is to minimize the marginal log-likelihood function. The sliding window Gaussian process applies the general algorithm to the training data within each window. The hyperparameters are required to be optimized for each Gaussian process kernel so that the kernel is able to force the similarity of two outputs of the regression function to increase as the similarity between two inputs increases. Recall that muscle co-contraction has a close relationship with movement attributes, such as velocity, direction, etc. Thus we believe that the changes of hyperparameters imply the occurrences of muscle co-contraction.

7.3 Experiment

7.3.1 Overview

The motion data to be analyzed consists of three-dimensional coordinates of human kinematics. There are several such curves generated from the human's tracing of a 3D curve. The number of curves depends on the number of markers required by a motion capture system. In the experiment, a single set of kernel parameters to be used to fit each curve. In the data set, it can be expected that the kernel parameters might change for different regions of the trace. Thus, the experiment's goal is to find the best sets of parameters by a sliding window

method, which works as follows: 1) choose a window length and, starting from the initial point for one of the coordinates, determine the kernel parameters using the gradient descent algorithm. 2) advance the start coordinate by a delta (window sliding length) and refit the kernel parameters. 3) As long as the parameters are stable, continue, but if they change, determine a new start point at the stage and start the setting process anew. 4) Continue this process until the entire process has been accounted for. The hypothesis is that the state of muscle co-contraction can be considered as revealed in a correlation with kernel parameters.

7.3.2 Data set

We used the motion capture data collected from the virtual training experiments described in Chapter 3. The motion capture suit with fifty markers (LEDs) is shown in Fig. 3.3. The motion capture data set contains tracing trajectories of path 7 in Fig 3.2. In this experiment, marker 8 was used as it was located on the right elbow joint. We expected to detect muscle co-contraction of the right elbow joint when the right arm was performing the tracing tasks. Ideally, it can be detected during the up-down motion, as mentioned in [48].

7.3.3 Results

Standard Gaussian process The general Gaussian process algorithm (shown in algorithm 1) uses one single kernel to fit the entire time series. Fig. 7.1 and Fig. 7.2 illustrates the results of using the general Gaussian process to fit the training data of marker 8. The solid line represents the mean prediction, and the shaded area indicates the 95% confidence interval from the mean. The co-

efficient R^2 is a criterion to value the prediction of the regression. It is defined as

$$R^2 = 1 - \frac{\sum_{i=1}^m (y_i - \hat{y}_i)^2}{\sum_{i=1}^m (y_i - \bar{y})^2} \quad (7.8)$$

where y is the true outputs data, \hat{y} is the predicted outputs, and \bar{y} is the mean of the true outputs. A model with perfect fitting would get a score of 1, while the score of a constant model, regardless of the input features, would be 0. It will be negative when the model is arbitrarily worse. Comparing two R^2 values, we can conclude that the 1D kernel fitting one coordinate is more accurate than the 3D kernel fitting three coordinates simultaneously. As shown in the two figures, the shaded interval in Fig. 7.1 are able to cover most of the training data, while there are some green outliers that the shady green gap is unable to hide in Fig. 7.2. Even though fitting 3D data is more complicated than fitting 1D data, the global 3D kernel still has a relatively high score, which is 0.89.

Sliding window Gaussian process The results of using one single global kernel are competitive. However, this method can not detect muscle co-contraction as the hyperparameters are constant. Therefore, we then applied the sliding window Gaussian process to the training data. The first step is to decide how many frames the window should slide each time. Fig. 7.3 illustrates the results of using local kernels in 1D cases with different sliding lengths. With a window size of 100 frames, a sliding distance of 1 frame produces the most smooth result. The regression becomes uneven as the sliding

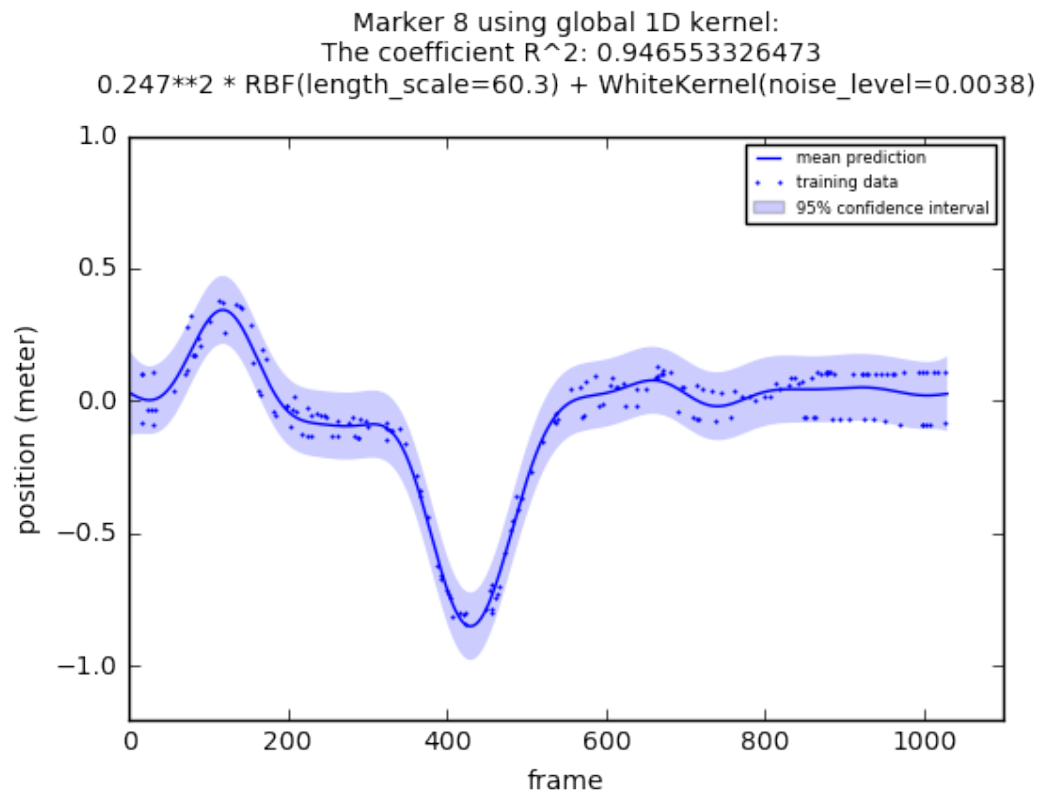


Figure 7.1: Standard Gaussian process with 1D kernel fitting the tracing data of marker 8 along the x-axis.

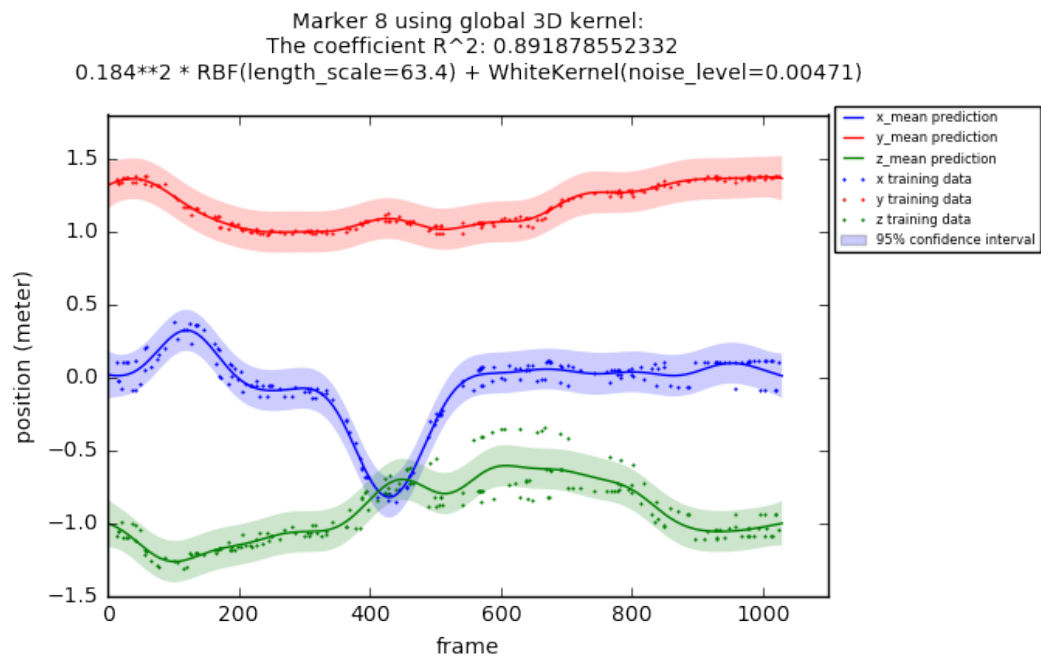


Figure 7.2: Standard Gaussian process with 3D kernel fitting the tracing data of marker 8.

length increases because there are multiple GPs at each frame. The mean prediction and standard deviation are the averages of means and standard deviations predicted by each of these GPs. The plots show no outliers outside the shaded area using the right window size and sliding length. Comparing Fig. 7.3 with Fig. 7.1 shows that the average results across multiple GPs' provide a better prediction at each frame. As the purpose of the experiment is to analyze the change in hyperparameters, it would be preferable to choose a slightly coarse approximation.

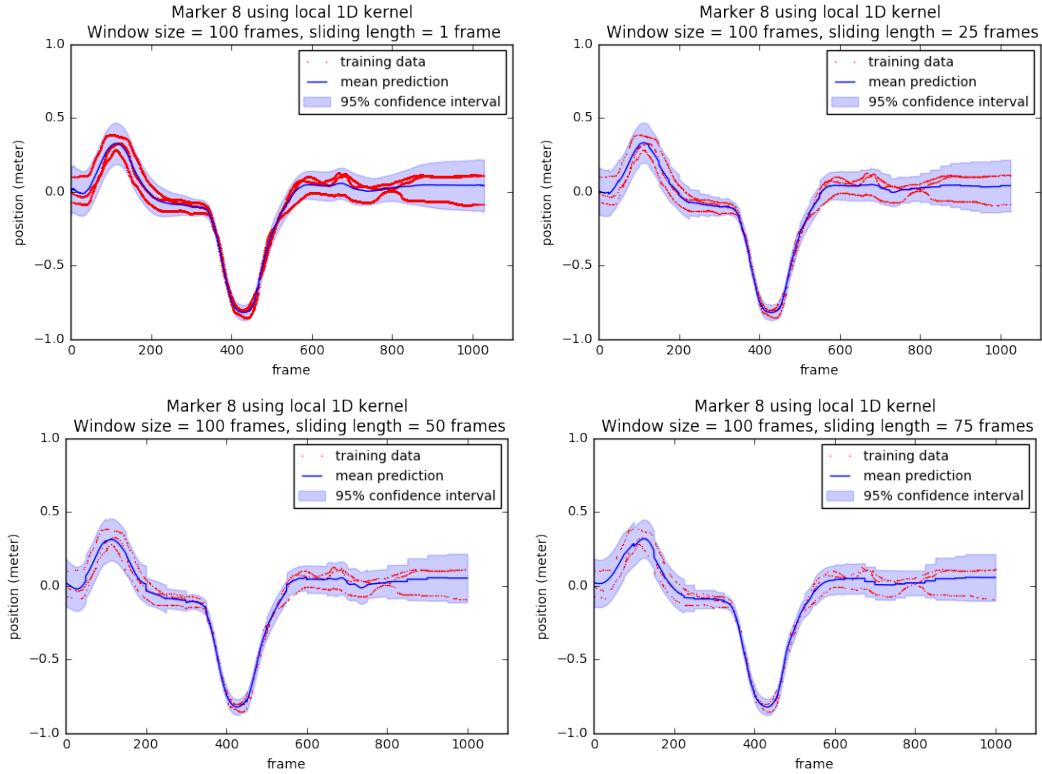


Figure 7.3: Sliding window Gaussian process with 1D kernel fitting tracing data of marker 8 along the x-axis with different sliding lengths.

The sliding window Gaussian process regressions of 3D cases are shown

in Fig. 7.4. Compared to Fig. 7.2, the shaded areas between frame 500 and frame 700 are wider, which fits the training data much better than using a single global kernel in 3D cases. Furthermore, this situation is more reasonable in realistic. In many movements of performing tasks, subjects start with strong muscle co-contraction and high motion accuracy. In the middle-late of the task, trajectory variance begins to show, and muscle co-contraction decreases. During the end part, some subjects will concentrate on the task again while some will not. In our example, the results indicated the participants concentrated on the tracing task at the end, so the muscle co-contraction became strong again, and the standard variance area became narrow. According to these facts, the sliding window Gaussian process has advantages for modeling human motion because it can better model the variance compared to a single global kernel.

Hyperparameter Comparison Fig. 7.5 illustrates the kernel hyperparameters change for different regions of the trace in 1D cases. As seen previously, the result curves are smoother with a smaller window sliding length. Recall that the motion data is about tracing path7 in Fig. 3.2. The four fixed red points on path 7 will be passed during the tracing task at frame 0 (frame 1029), frame 249, frame 582, frame 749. While tracing path 7, subjects start with the straight horizontal cyan line, then trace the straight vertical yellow line, and finally complete two complex black curves.

The results clearly show the changes of hyperparameters around frame 250 and frame 600. As the point at frame 749 smoothly connects the two adjacent curves, the changes around frame 750 are not apparent when the window sliding length is too small or too large. However, the changes still can

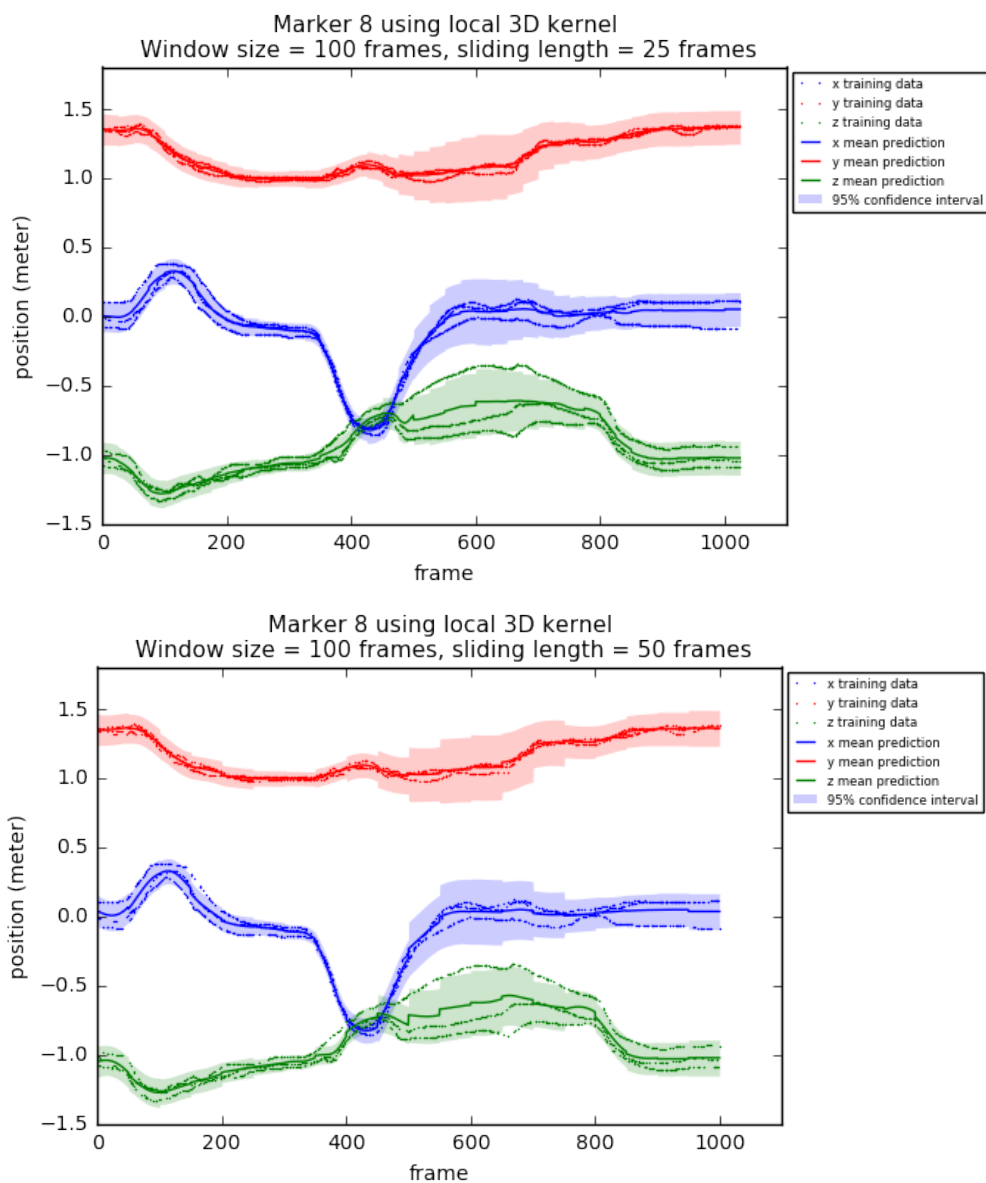


Figure 7.4: Sliding window Gaussian process with 3D kernel fitting tracing data of marker 8 with different sliding lengths.

be seen when using a sliding length of 25 frames and 50 frames. Furthermore, in practice, the variances of tracing trajectories increase with the more complex paths. As the last two black curves from frame 582 to the end are more complex than horizontal or vertical straight lines, the σ_l plots are more coarse from frame 600.

The fitting results in 3D cases are shown in Fig. 7.6. Compared to 1D cases with the same sliding length, 3D kernel's hyperparameters changes better imply movement changes while tracing path 7. From the results of both 1D and 3D cases, we can preliminarily conclude that the σ_l mainly implies the variance of tracing trajectories, and the σ_f implies the state of muscle contraction. To further establish this hypothesis, an experiment with EMG would be needed.

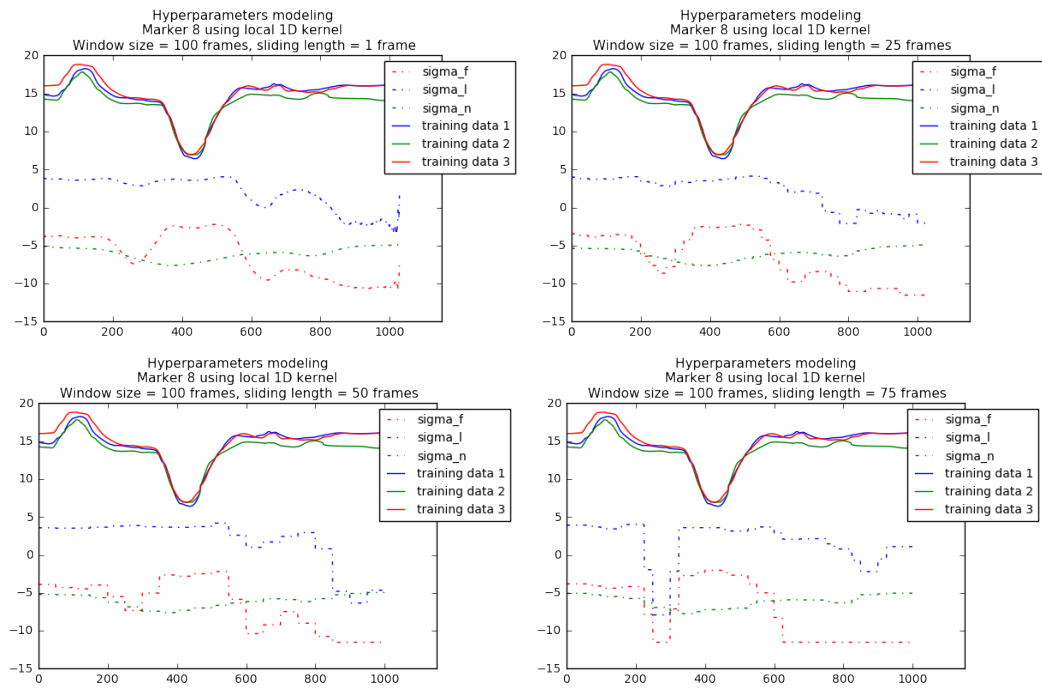


Figure 7.5: Hyperparameters modeling for sliding window Gaussian process with 1D kernel fitting tracing data of marker 8 along the x-axis with different sliding lengths.

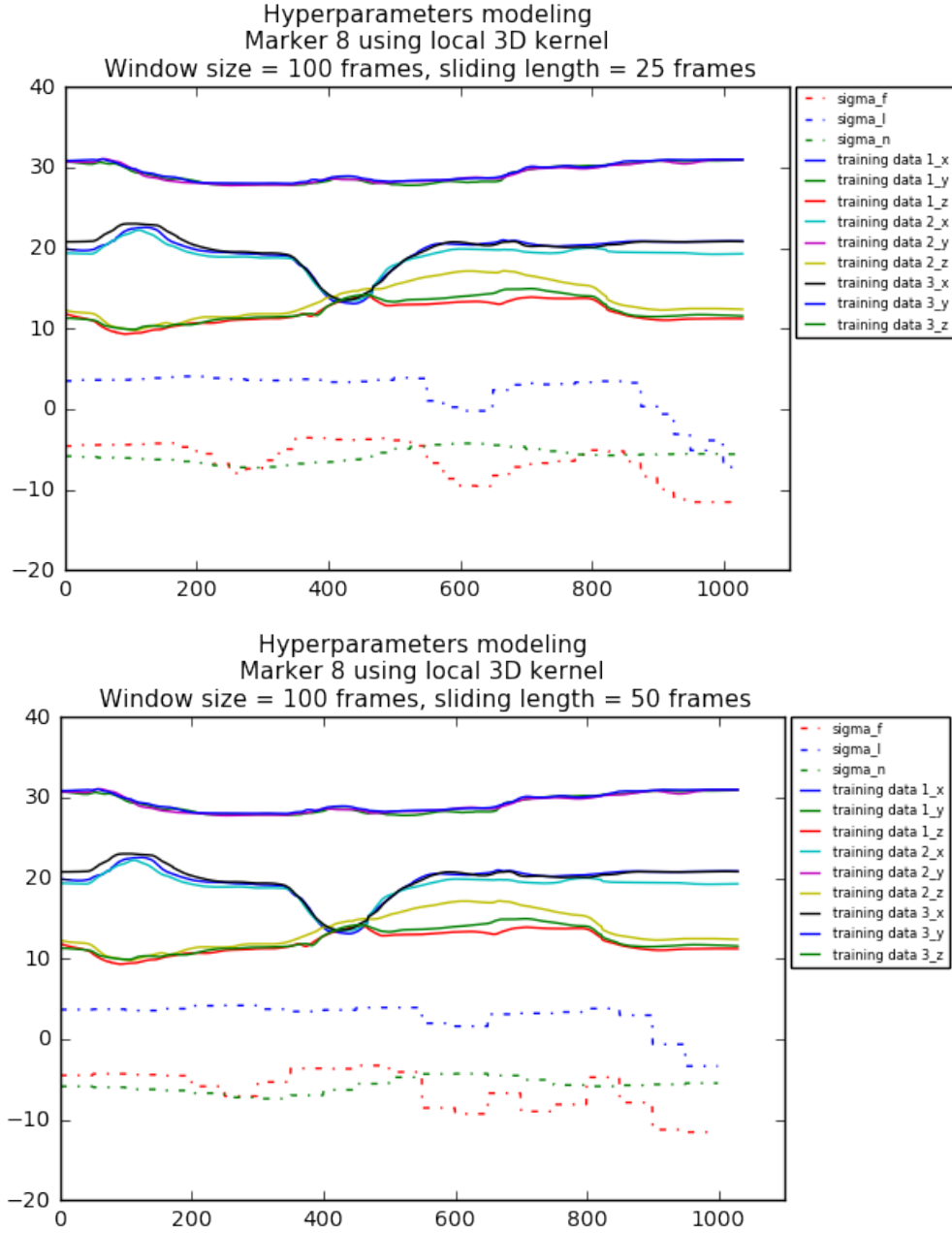


Figure 7.6: Hyperparameters modeling for sliding window Gaussian process with 3D kernel fitting tracing data of marker 8 with different sliding lengths.

Chapter 8

Future Work

This dissertation describes original research in simulating and analyzing whole-body human movements. The central collection has been to explore the hypothesis as to the use of energetic costs as a central objective constraint in the choice of movements. In service of this goal, we took a dynamic model system of human movement and refined it to the point where it could be a trusted tool for interpreting experiments. Specifically, we have shown how virtual reality techniques can be used to design a goal-directed experiment for human motion capture. A robust dynamics human model, built on top of ODE, has been adapted into a more user-friendly and task-specified tool with intuitive parameters for energetic cost calculation. We feel that the significant uses of the model lie ahead. To exhibit the model's additional capability, we conducted several experiments related to different academic areas and provide some possible ideas that could be available for further exploration. Studies of locomotion in nature terrains and simple single-behavior motion synthesis have been described in detail in this chapter. Three other possible avenues for future work have been briefly discussed as well.

8.1 Locomotion in Natural Terrains

8.1.1 Background

As mentioned in section 2.3, a general principle of locomotion is that humans' walking speed, step frequency/length, and step width correspond with the metabolic cost. The minimum energetic cost is always consistent with the self-selected or preferred walking styles. Furthermore, new evidence shows the nervous system can adapt preferred gaits to minimize energetic cost. However, the experiments were mainly conducted indoors on a treadmill. To study the locomotion while walking in natural terrains, a novel system was developed by Matthis [65] for simultaneously recording the humans' eye movements and whole-body kinematics during walking.

The paper [65] was aimed to study the gaze and the control of foot placement. However, its results prove or imply some principles that were consistent with the results of the experiments described in previous chapters. For example, in Matthis's locomotion tasks, the participants received no instructions for completing this task, except for walking from the beginning position to the destination with a comfortable walking speed. A surprising result is that the variability of subjects' gaze behaviors while walking over the same nature terrains is very low. This consistency suggests that subjects tried to adapt their preferred gait cycles to the complexity of the terrain, and subjects' gaze behaviors were mainly subjected to the constraints of the locomotion task [65]. In our virtual tracing experiment, the results also show high consistency in tracing trajectories across different subjects under common goals, which motivated us to study the minimum cost principle further.

Furthermore, the paper [65] also shows evidence that the motion plan

of the motor cortex supports successful movements to the varying demands of the natural world.

1. Humans attempt to minimize the energetic cost of walking by utilizing gait cycles with which they are most comfortable. However, they deviate from energetically optimal movement patterns while over complex terrains.
2. Humans tend to plan two steps ahead before the beginning entails, leading to the cost of deviating from the preferred gait cycle be minimum. Furthermore, when terrains become complex, they will look three steps ahead.
3. Humans use different strategies while walking on different nature terrains.

The paper finally concludes that gaze strategy is intimately linked to locomotion through integrating the conditions of minimizing energetic costs, adapting environmental uncertainty, and meeting the locomotor task's instant demands. This conclusion is based on the principle that human preferred motion sequences are minimum in the energetic cost. Therefore, there is a need to compute the energetic cost of the movements while walking in nature terrains. Ideally, the different energetic costs could indicate different terrains.

8.1.2 Experiment

Motion data The motion capture data collected in Matthis' [65] study are stored in MAT files. We can extract two information from them:

1. Full-body kinematics. Fig. 8.1 (a) illustrates the schematic of the human body skeleton and marker assignments.
2. Foot placement sequences. It records at which frames the feet were on the ground and the corresponding feet position. It is used for simulating the terrains.

Data fitting As the motion capture data uses thirty markers, we first needed to assign markers to appropriate body segments. Fig. 8.2 describes the mapping relationship between markers and body segments. Next, we moved the motion data from MAT files to CSV files and loaded them to the human dynamic system. After that, we adjusted the sizes of the human dynamic model to match the motion data using the "Dimension" functional sub-panel on the user interface. Finally, we set the initial values to zeros and then manually adjust the approximate body-marker relative positions using the "Marker" functional sub-panel on the user interface. Fig. 8.3 illustrates a final fitting of the human dynamic model. The pose of the human dynamic model is, qualitatively, pretty close to the one in Fig. 8.1.

Terrain simulation Recall that the human dynamic model works as follows: 1) simulate motions by following the markers in order to calculate and record the joint angles at each frame (inverse kinematics), 2) apply the record joint angles to let the human dynamic model reproduce the motion and calculated the joint torques at each frame (inverse dynamics). In the second round, the human dynamic model needs to react with the ground to get the upright forces and the horizontal frictions. So the difficulty of this experiment is how to simulate the terrains. As a starting point, we used a method called "boxes

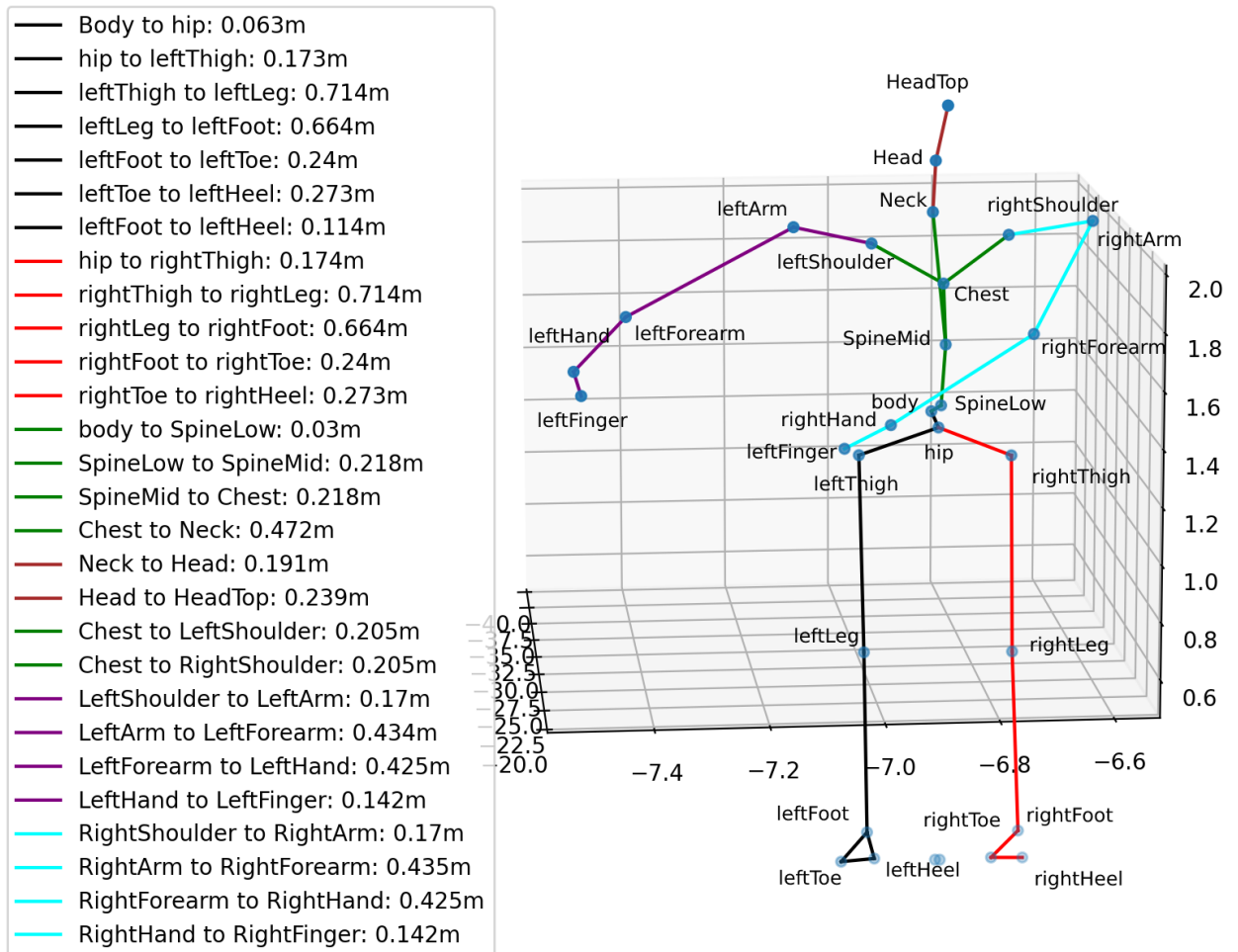


Figure 8.1: An illustration of motion capture data used in the locomotion experiment.

Marker - Body Mappings							
Index	Marker Name	Index	Body Name	Index	Marker Name	Index	Body Name
0	Body	12	WAIST_BODY	15	LeftShoulder	7	L_COLLAR_BODY
1	Hips	12	WAIST_BODY	16	LeftArm	8	LUP_ARM_BODY
2	LeftThigh	17	LUP_LEG_BODY	17	LeftForearm	9	LLO_ARM_BODY
3	LeftLeg	18	LLO_LEG_BODY	18	LeftHand	10	L_HAND_BODY
4	LeftFoot	20	L_TARSAL_BODY	19	LeftFinger	10	L_HAND_BODY
5	LeftToe	20	L_TARSAL_BODY	20	RightShoulder	3	R_COLLAR_BODY
6	LeftHeel	19	L_HEEL_BODY	21	RightArm	4	RUP_ARM_BODY
7	RightThigh	13	RUP_LEG_BODY	22	RightForearm	5	RLO_ARM_BODY
8	RightLeg	14	RLO_LEG_BODY	23	RightHand	6	R_HAND_BODY
9	RightFoot	16	R_TARSAL_BODY	24	RightFinger	6	R_HAND_BODY
10	RightToe	16	R_TARSAL_BODY	25	Neck	1	NECK_BODY
11	RightHeel	15	R_HEEL_BODY	26	Head	0	HEAD_BODY
12	SpineLow	11	LO_TORSO_BODY	27	HeadTop	0	HEAD_BODY
13	SpineMid	11	LO_TORSO_BODY	28	LFP	-	NA
14	Chest	2	UP_TORSO_BODY	29	RFP	-	NA

Figure 8.2: An illustration of mapping markers to appropriate body segments.

simulation” to dynamically generate boxes right below the feet at each step at the first round. The human dynamic model will then react with those boxes to get support forces and frictions when stepping on them at the second round. As the nature terrains could go below the horizontal line, in other words, the heights of the ground could be negative, we shifted the entire motion capture data up 5 meters. Fig. 8.4 illustrated the simulated terrain. A video¹ of the demonstration has been posted online.

Energetic cost Once complete fitting motion capture data to the human dynamic model and simulating the movement environment, we are ready to calculate the energetic cost of walking on terrains. The method is the same as what was described in Chapter 4. Fig. 8.5 shows the preliminary results of simulating a subject named JAC walking in natural terrain. Each time

¹Walking on terrains demo: <https://www.youtube.com/watch?v=b2zdx0GvCJk>



Figure 8.3: An illustration of fitting the human dynamic model to motion capture data.

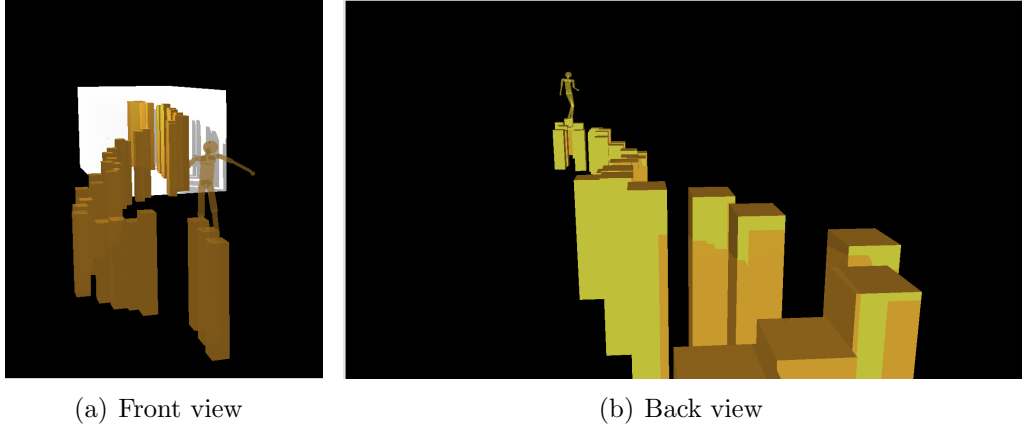


Figure 8.4: Simulation of the human dynamic model walking on rough terrains. The brown boxes were dynamically generated according to the real motions.

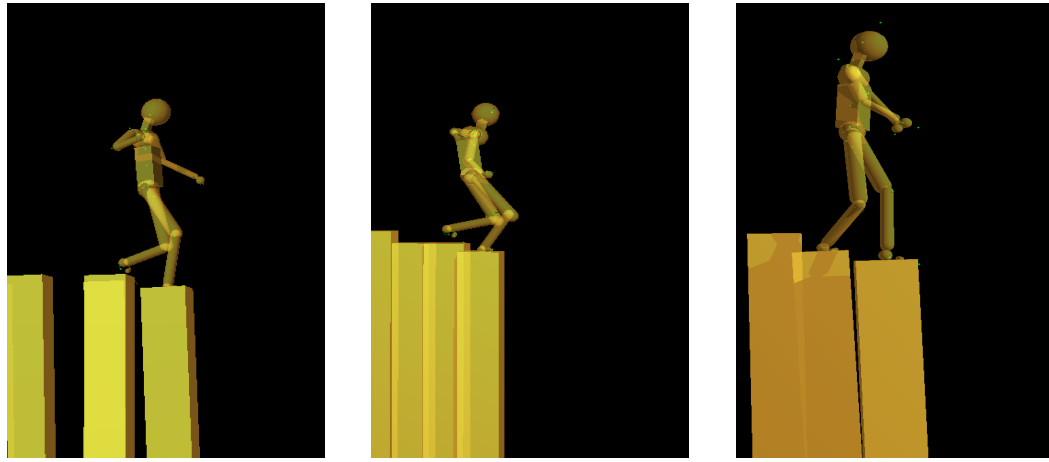
the subject was walking over the same general area, but the path they took changed for each trial. In Fig. 8.5, the paths were indexed with 1, 3, and 5. Fig. 8.5 (a) (b) and (c) demonstrate the poses the subject used during the three walking trails. (d) shows the energetic cost of the subject with three different trails. The results are interesting:

1. The subjects used different walking strategies (poses) over different paths, which is consistent with the conclusion in paper [65]. The pose of path3 indicated that the center of mass (COM) of the subject walking over path3 was much lower than the ones while walking over the other two paths.
2. The hand of God (HOG) cost (residual torques/forces) of path3 is the smallest. As mentioned in section 4.1.4, the HOG does not exist in reality, which is a way to compensate for the discrepancies between the dynamics torques/forces of the model and the kinematics of the real motions. The primary function of HOG is to stabilize the model when

using the inverse dynamics method. As the COM of poses for path3 is lowest, it is reasonable that the needed external forces for balance are the smallest.

3. The internal joint cost path3 is the largest. This result is expected because walking with bending legs leads to more energetic costs on knee joints.
4. The energetic costs of walking on three different paths over the same terrain are different. We expected that the difference in energetic costs would increase as the distinction of the terrains increase.

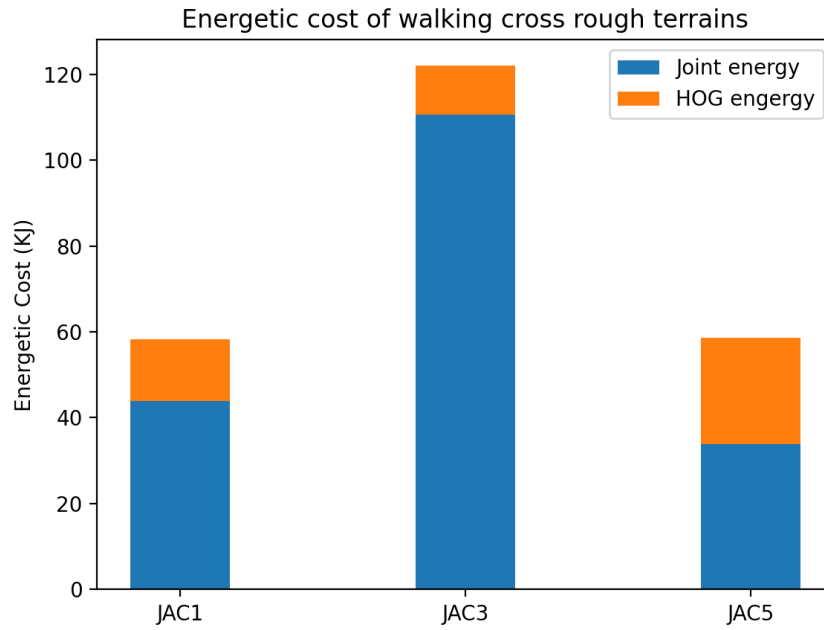
Summary As humans can adapt their gaze and foot placement according to the terrains [65], our hypothesis is that the different energetic costs could imply different terrains. The method is based on the principle that humans prefer trajectories that cost minimum energy. We developed a simple "boxes simulation" method for the terrain simulation, which is straightforward and well functioned. However, the frictions of those boxes' surfaces are arbitrarily defined. Besides, each box's surface is even, which is not the same as the slope of the real terrain. Thus, one of the remaining works is to refine the environment simulation. We can either use different shapes to construct the simulated terrains or integrate the terrain files with the ODE system to produce real landscapes. Another remaining work is to test this method on various terrains.



(a) A pose at path 1

(b) A pose at path 3

(c) A pose at path 5



(d) Energetic cost

Figure 8.5: Simulation of a subject walking on rough terrains over three different paths. JAC is the subject's name, followed by the number 1,2, 3, which indicate different walking paths.

8.2 Simple Single-Behavior Motion Synthesis

8.2.1 Background

Nowadays, virtual character animation is prevalent in the computer graphics industry, such as video games (The Sims) or movies (Avatar). There are three commonly used character animation techniques: keyframing, motion capture, and dynamic modeling.

The best-known animation technique is keyframing, which requires users to position the character at key instances of time. Fig. 8.6 illustrates an example of a captain waving to the outside through a window. It works as follows: 1) the first keyframe defines the starting posture –” captain at the beginning”, 2) the last keyframe defines the final posture –” captain at End”, 3) take another three intermediate keyframes of the captain’s posture between the beginning and the end, 4) the frames played in succession yields a simple, though complete, keyframed animation. Keyframing originates in traditional media and is still widely used today. It is the simplest form of animating an object and allows complete control over every motion detail. However, while using this method, an effort is required in specifying a large amount of information, and considerable skills are required to achieve natural-looking motions.

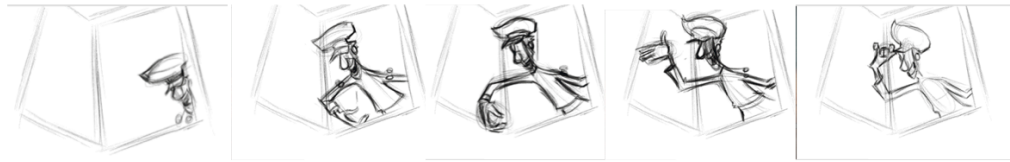


Figure 8.6: An illustration of the keyframing method.

The most popular and most direct kinematic method is motion capture.

It is a way to record human movements digitally: 1) Let subjects wear a suit with visual-markers, 2) record the visual-markers position, 3) map visual-markers to their corresponding markers on a digital human, as we described in Chapter 3. This method is pretty straightforward. However, it is limited to motions that have been previously recorded and motions that are recordable.

The third method, dynamic modeling, is theoretically the best way to model characters. However, as mentioned in section 2.3, it is challenging for large systems due to its complexity. However, combining the dynamic modeling with our human dynamic model could be a much simpler method to generate arbitrary motion sequences. The method includes three components: 1) a low degree of freedom robot to generate motions of key body parts. 2) a learning machine to generate the motions of remaining body parts. Its training data are existing motion capture data sets. 3) A human dynamic model to simulate the motion based on the generated motion capture data on steps 1) and 2).

8.2.2 Experiment

Construct a 2D biped robot. Before modeling, the essential body parts of a specific motion should be defined. For example, in human walking, the key body parts of studying walking motions should be the two legs and the trunk, which decide the walking orientation and velocity. In contrast, the upper bodies, such as shoulders, arms, etc., are less critical. Their movements were depended on how the essential parts move. Therefore, a controllable dynamic five-link robot was needed to simulate two legs and the trunk (shown in Fig. 2.2(b)).

Besides, human walking is a subsequent gait cycle. For each gait cycle, the period starts from the initial contact of one foot with the ground and ends with the following contact of the same foot, which includes the single support phase (SSP) and the double support phase (DSP). The SSP is the main focus of studies in the human walking field as it contributes to a larger share in the walking gait cycle. The assumption is that only the SSP exists in a gait cycle for a complete gait cycle. In other words, When the swing leg contacts the ground, researchers assume an instantaneous swap of the support leg occurs. Therefore, the biped locomotion with single foot support can be considered as a successive open loop of kinematic chain from the support point to the free ends, as robot manipulators.

Generate 3D trajectories To implement the dynamic modeling of walking with a five-link biped robot, the first step is to drive equations of motion in order to describe the SSP. The dynamic equations can be derived using the standard procedure of Lagrangian formulation [71]:

$$\frac{d}{dt} \left(\frac{\partial K}{\partial \dot{q}_i} \right) - \frac{\partial K}{\partial q_i} + \frac{\partial P}{\partial q_i} = Q_i \quad (8.1)$$

The kinematic energy K can be derived as follows:

$$\begin{aligned} K &= \sum_{i=1}^5 K_i \\ &= \sum_{i=1}^5 \left(\frac{1}{2} m_i v_{ci}^2 + \frac{1}{2} I_i \dot{\theta}_i^2 \right) \\ &= \sum_{i=1}^5 \left[\frac{1}{2} m_i (\dot{x}_{ci}^2 + \dot{y}_{ci}^2) + \frac{1}{2} I_i \dot{\theta}_i^2 \right] \end{aligned} \quad (8.2)$$

The potential energy P is:

$$\begin{aligned}
P &= \sum_{i=1}^5 P_i \\
&= \sum_{i=1}^5 m_i g y_{ci} \\
&= \sum_{i=1}^5 \left\{ m_i g \cdot \left[\sum_{j=1}^{i-1} (a_j l_i \cos \theta_j) + d_i \cos \theta_i \right] \right\}
\end{aligned} \tag{8.3}$$

Finally, we can get the equations of motion:

$$D(\theta)\ddot{\theta} + H(\theta, \dot{\theta})\dot{\theta} + G(\theta) = T_\theta \tag{8.4}$$

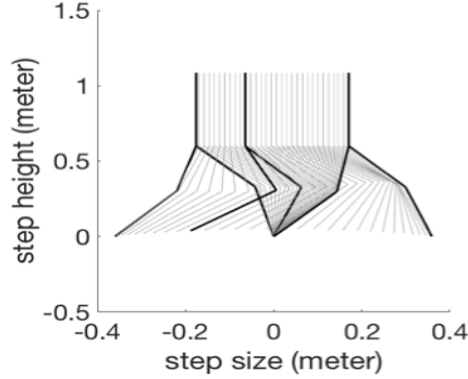
The second step is to design gait cycles, which is also called motion planning. Time polynomial functions are used for approximate one gait cycle. Its coefficients are determined through some constraint equations. The constraint equations are for designing requirements of walking gaits, such as maximum step height, step length, progression speed, etc. The third step is to let the robot walk based on the gait cycle, which is also called motion control. A PD controller, which is commonly used in industrial control systems, controls the robot. The dynamic equations of the PD controller are:

$$u = k_p(q - q_d) + k_d(\dot{q} - \dot{q}_d) \tag{8.5}$$

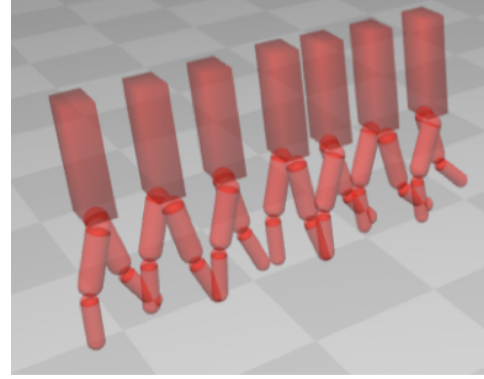
$$D(\theta - u) * \ddot{\theta} + H(\theta, \dot{\theta}) * \dot{\theta} + G(\theta) = T_\theta \tag{8.6}$$

In our example, the 2D robot walks in a 3D environment. In this way, we can calculate the 3D trajectories of the body segments where markers are

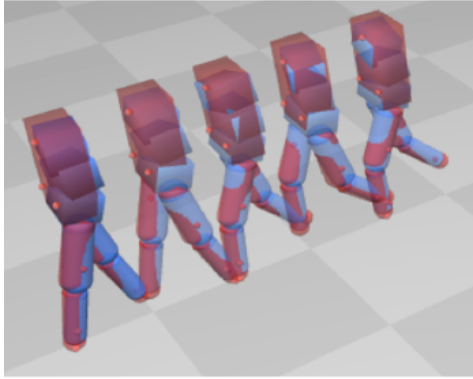
attached. Fig. 8.7 illustrates the implementation of the dynamic modeling for walking.



(a) Motion plan: generate desired gait cycles



(b) Model control: simulate 2D five-link robot in 3D environment.



(c) Marker trajectories generation

Figure 8.7: An implementation of a 2D five-link biped robot in a 3D environment. (c) fits the five-link robot (red model) to the human dynamic model (blue model). The blue model is the previous version of our human dynamic model. The red dots are the desired markers. Their trajectories will be used as the inputs of the PCA learning machine.

Construct a learning machine Once collect a motion data set of key body parts, the next task is to predict the motion trajectories of the remaining body

parts, which is equivalent to solving the problem of missing markers estimation. We used a data-driven, piecewise linear modeling approach to estimate the missing body positions [58]. Fig. 8.8 illustrates an overview of this algorithm, which is as follows:

1. Build a linear model: apply the PCA algorithm to existing motion capture data of walking to get the Mean Vector and Eigenvector Matrix of walking motions.
2. Estimate missing positions: given the motions of key body parts generated by the five-link biped robot, apply PCA on the motion to get its projection on the lower-dimension, then left multiply with the Eigenvector Matrix and add with the Mean Vector to estimate the missing positions of the remaining body parts.

Fig. 8.9 illustrates an experiment using a walking sequence with small steps to construct walking sequences with longer steps. It aims to test the performance of the PCA learning machine. The training data of the machine is the motion data of walking with long steps (Fig. 8.9 (a)). Its inputs are the trajectories of markers located on the legs and the trunk shown in Fig. 8.9 (b). Its outputs are the estimated trajectories of markers attached to the remaining body parts, such as arms, shoulders, etc. Fig. 8.9 (c) demonstrates the reconstructed walking sequences with long steps and Fig. 8.9 (d) shows the average errors of estimated marker positions at each frame.

Fig. 8.10 shows the performance of the marker-estimation machine. Six different walking sequences were provided. One sequence was used as training data to reconstruct the other five walking sequences as well as itself. The black

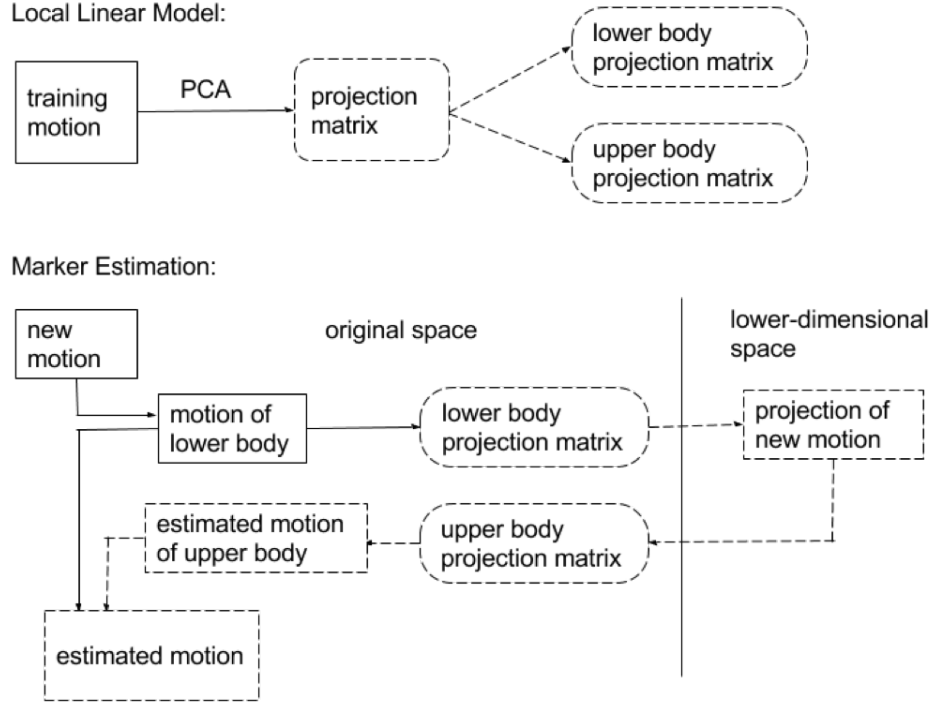
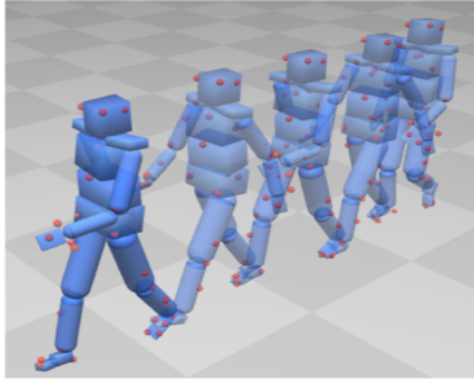


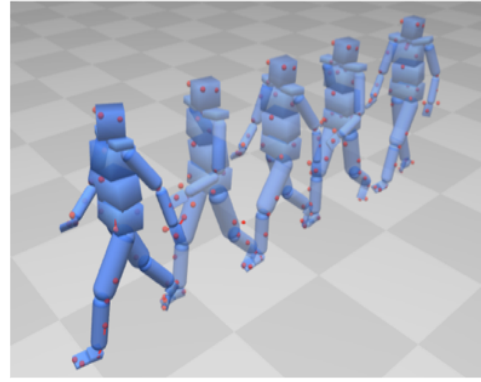
Figure 8.8: The overview of missing body positions estimation algorithm.

curves indicate the errors when using the leg markers of this sequence to reconstruct its self. The average errors are around 1 cm, which is pretty small. For the other five reconstructions, the average errors of estimated marker positions are between 1.5 – 5 cm, which is acceptable.

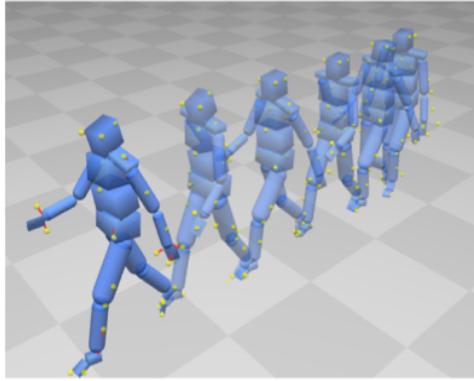
Arbitrary walking sequence construction Given a five-link biped robot and a learning machine, we are able to generate arbitrary walking sequences. Fig. 8.11 demonstrates the process: 1) According to the desired gait cycles, we use the robot to generate the marker positions of legs and torso, which will be



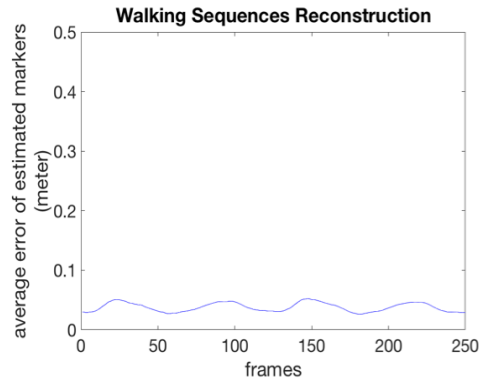
(a) Training data: walk with small steps



(b) Test data: walk with long steps



(c) The reconstruction of walking with long steps



(d) The average error of estimated markers at each frame.

Figure 8.9: A reconstruction experiment using the PCA learning machine.

used as the inputs of the learning machine. 2) We train the learning machine with the existing walking motion capture data. 3) estimate the remaining marker positions and display the synthesized motions using our human dynamic model.

Summary This section describes a possible way to synthesize arbitrary simple single-behavior human motions. First, we built a lower dimension biped robot needs for generating motion capture data of the partial human body.

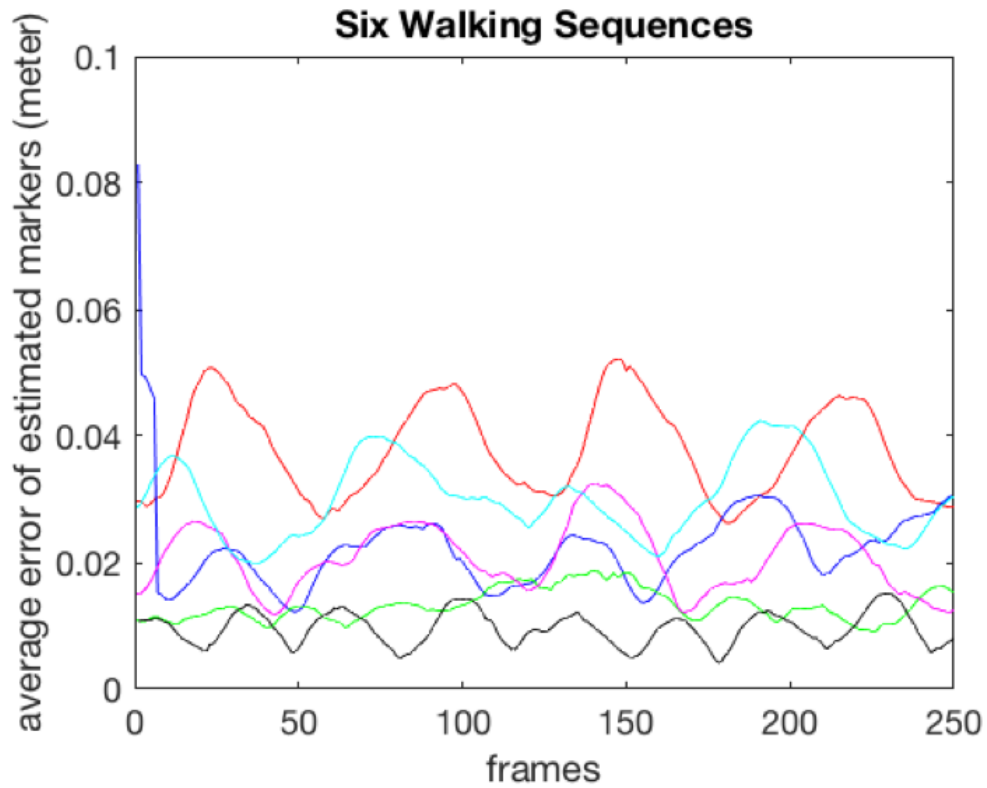


Figure 8.10: The performance test of the PCA learning machine.

Then, we built a learning machine trained with existing motion capture data of the same kind of motions for estimating the motion capture data of the remaining body parts. Finally, display the synthesized motion using our human dynamic model. This method has the following advantages:

1. It drastically simplifies the dynamic modeling process. For example, in the walking synthesis, we used a five-link bipedal robot instead of a 21-link whole body robot.
2. It addresses some limitations of the motion capture method. For example, it is no longer limited to motions that have been previously recorded.

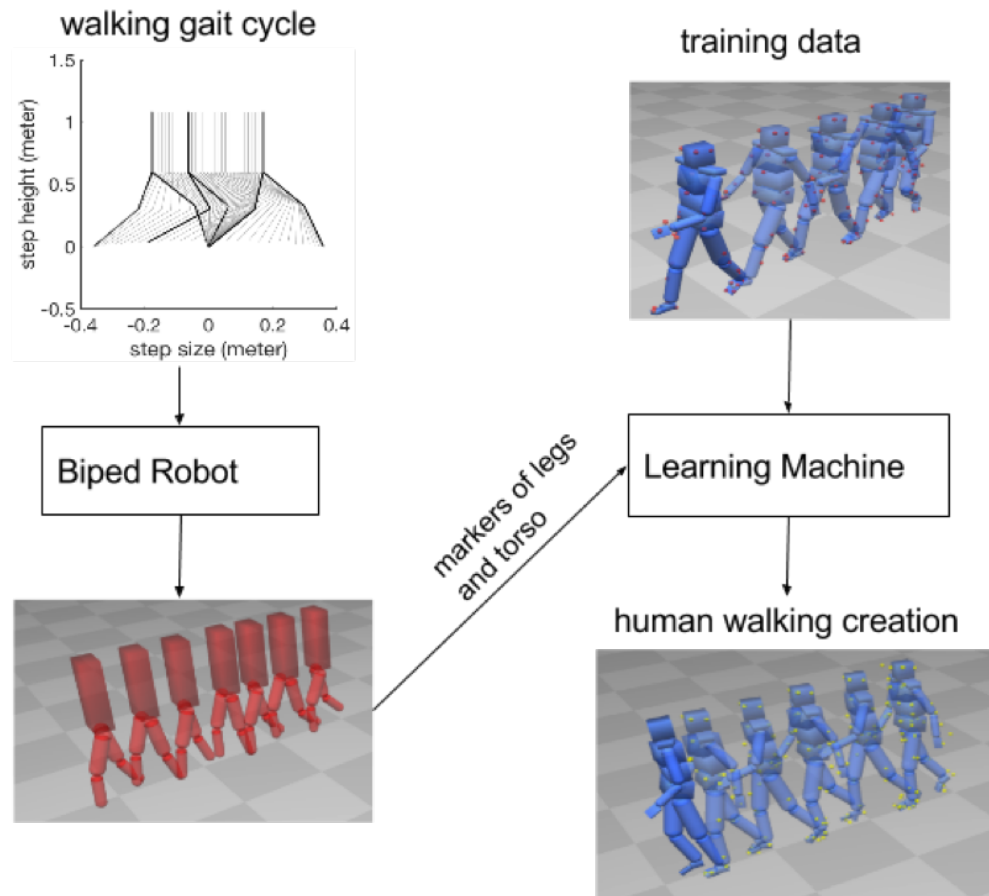


Figure 8.11: Arbitrary walking sequence synthesis. The blue model is a previous version of our human dynamic model.

It can generate novel motions based on existing motion capture data.

3. It makes our human dynamic model less reliant on motion capture data as well.

However, it has some disadvantages as well:

1. The simplified biped robot is in x-z planar, which limits the variety of synthesized motions. For example, it can not construct the movements of turning around or walking in a circle.
2. The walking gait cycle is designed artificially, which is offline. It can not synthesize motions in real-time.

Therefore, the future work can be to build a 3D biped robot according to the desired human motions and make the process of gait cycle generation automate.

8.3 Human movements animation

Animating whole-body human movements in service of goals have widespread impact in different fields such as movies, video games, and the basic science of understanding the mechanisms that direct movement at a fundamental abstract level. Current software capabilities allow the kinematics to be obtained from human subjects, allowing these movements to be reconstructed and used in various settings. However, using such data to create arbitrary goal-directed movements remains a research challenge.

The next step of the research can be to develop a system to generate goal-directed human movement sequences that appear to be smooth and natural. One way is to take advantage of the probability principal component

analysis (PPCA) method [98] to encapsulate complex movement sequences into primitive movement segments automatically. A database of these segments will serve as basis sets from which arbitrary goal-directed motions can be constructed. Second, use a simple motion blending algorithm or our dynamic humanoid model to smoothly stitch two motion segments and display the final synthesized movement sequences. With some improvements, e.g., compressing motion data for fast transmission or compact storage, it will be an excellent approach to animate character motions for computer graphics.

To visualize this idea, we made two simple demonstrations. Fig. 8.12 illustrates a demonstration of motion synthesis given two different sets of motion capture data. We chose the first three-quarter of the trajectories of tracing path 1 and the last quarter of the movement of tracing path3 (Fig. 3.2). We used a simple blending algorithm to stitch these two movement segments and simulate the new tracing movement using our dynamic human model. The videos of synthesized motions with/without using a blending algorithm have been uploaded online.^{2 3}

Fig. 8.13 shows a demonstration of generating new motions of walking through a maze. The given primitive movement segment is a three-second motion capture data of walking. We used our forty-eight degree of freedom dynamic humanoid model to help stitch walking and turning left or right. Given the maze map, we used an LTL motion planning algorithm [20] to get the optimal route.

²With blending algorithm <https://www.youtube.com/watch?v=V374DRI62IO>

³Without blending algorithm https://youtu.be/Pwya_zD9Urc

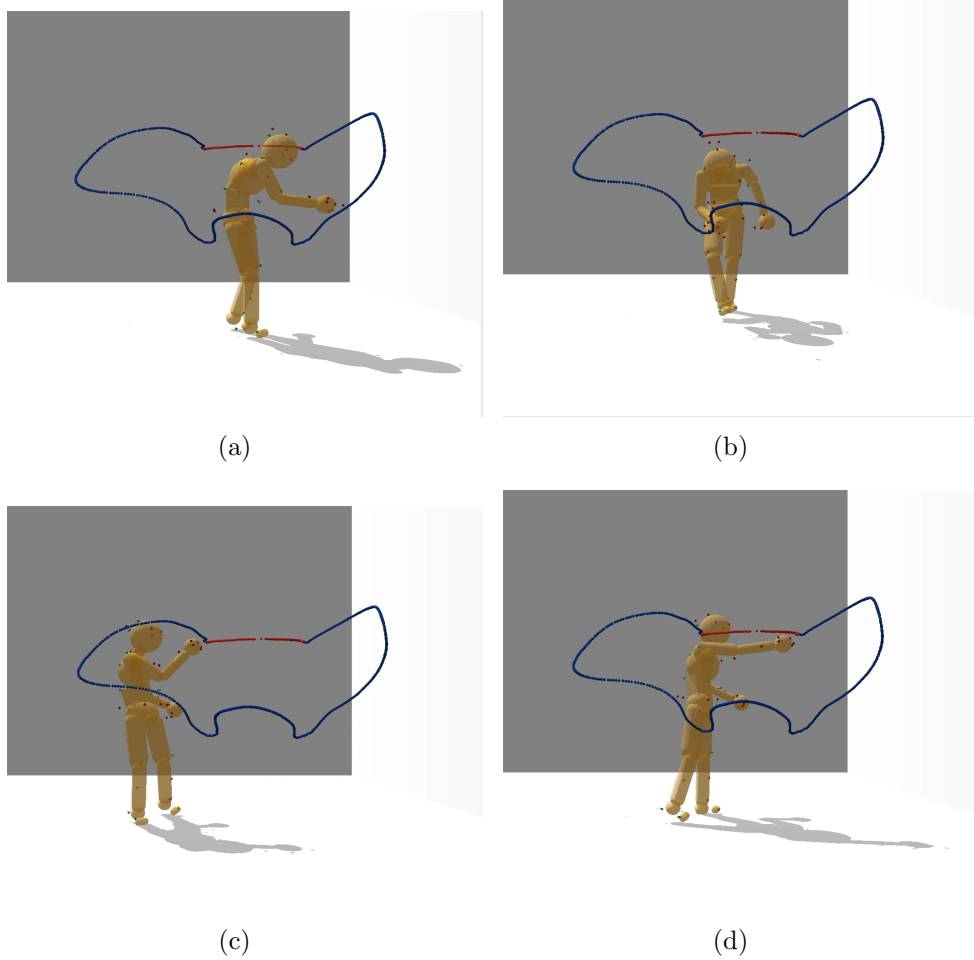
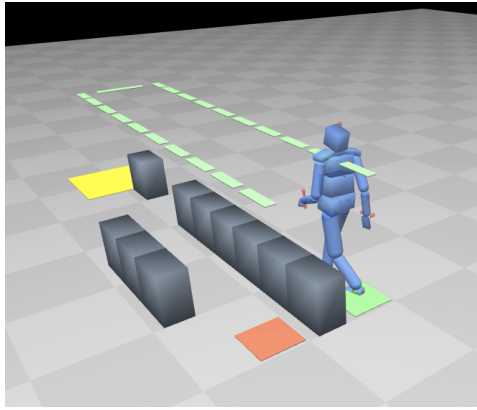
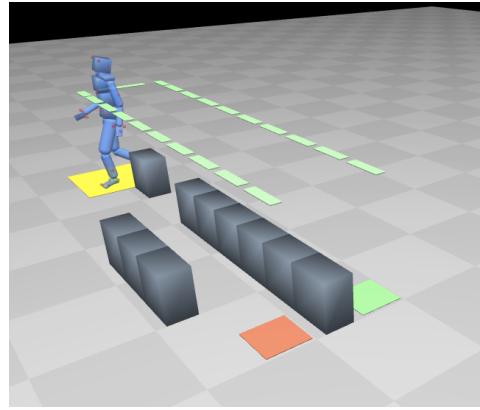


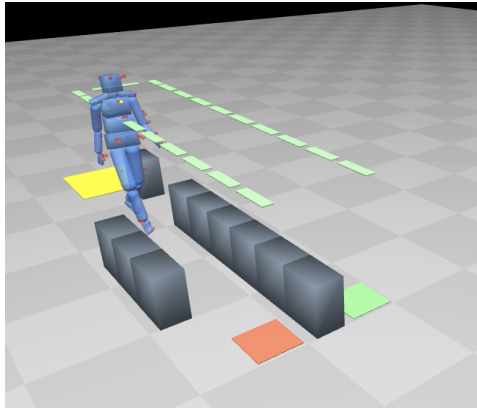
Figure 8.12: Tracing synthesis. The blue line represents the three-quarter of path 1, and the red line represents the last quarter of path3. The dynamic human model was smoothly tracing the new curve given the synthesized motion capture data.



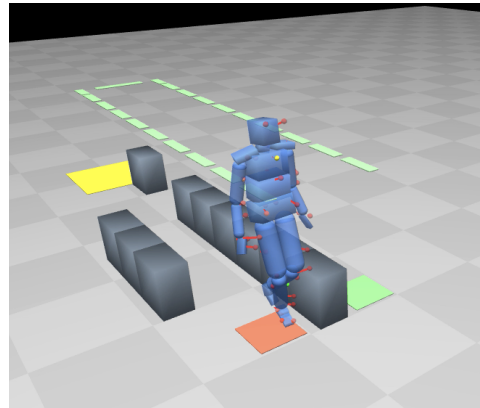
(a)



(b)



(c)



(d)

Figure 8.13: **walking in a maze.** The maze is designed as follows: 1) green grid is the initial position, 2) red grid is the destination, 3) yellow grid is the place that the planned path must be through, 4) the grey cubes are the obstacles. The green line in the air shows the planned optimal route.

8.4 Improvement of the dynamic model

The forty-eight degree of freedom dynamic human model is a fast, robust, intuitive, and inexpensive multi-purpose tool for simulating, analyzing, and synthesizing humanoid movement. However, though we have made it more user-friendly, it still has some disadvantages. For example, to simulate custom motions, users need to manually locate markers to body segments and resize the model to fit a real human skeleton according to the given motion data. Besides, as joints between body segments are considered springs in our human dynamic model, there must exist an optimal spring stiffness set for different motions, leading to minimizing energetic costs. The spring stiffness is indicated by the constraint force mixing parameter (CFM) in ODE. Currently, the CFM values are pre-defined by us based on general motions.

Thus, the next work could be to fit the model to the motion capture data automatically and tuning the parameters. One possible method is to use the "black-box" optimization method [31]. The quality of the fit between motion data and the model can significantly influence the energy computation. Thus the computed energy cost would be significantly higher than the real cost if the model fitting failed. The objective function of the optimization system can be minimizing the energy cost of all joints and the residual torques under physical constraints of joint angles or torques. The overview idea is shown in Fig. 8.14.

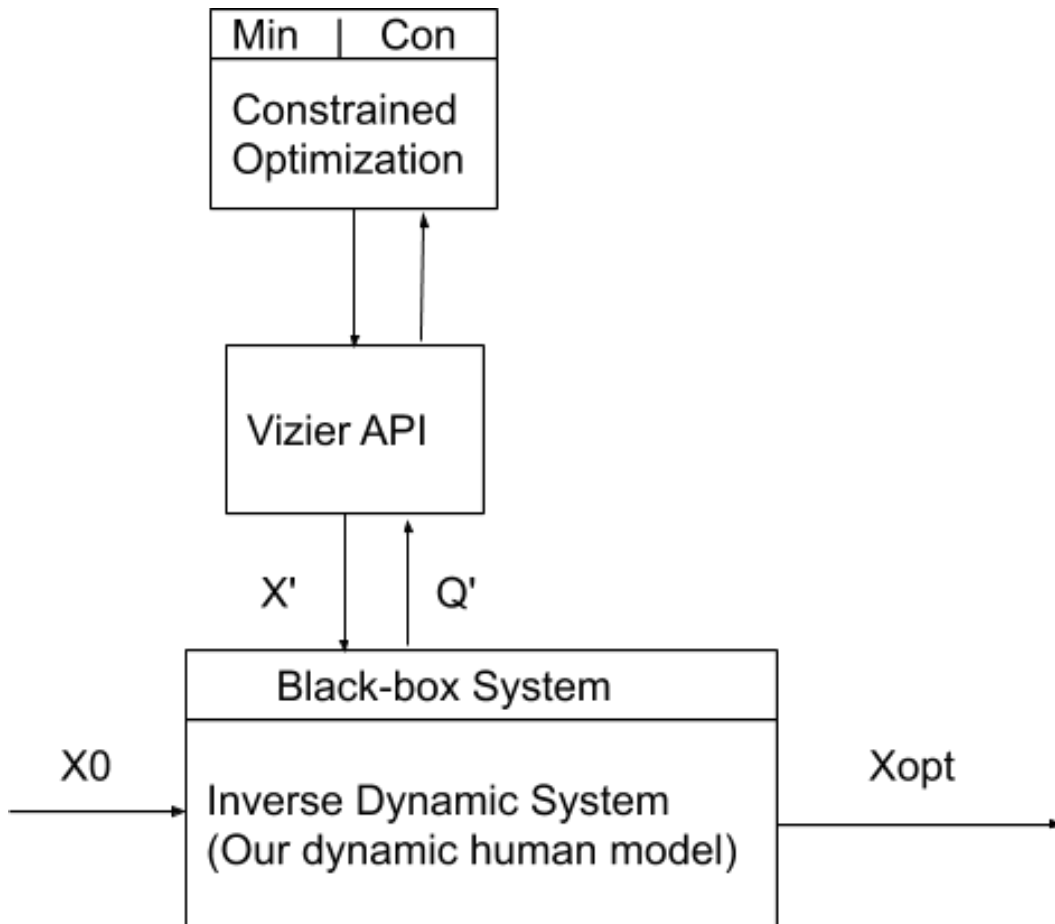


Figure 8.14: Scheme of the optimization algorithm The X_0 represents the system's initial parameters, e.g., X_0 could be the markers' positions relative to body segments. The X' and Q' describe the intermediate results during the process. The X_{opt} represents the optimized parameters.

8.5 Dynamics analysis of human movements

Kinematic analysis of human movements has been vitally studied, such as Sparse coding of human motion trajectories [105], Gaussian process dynamical models for human motion [107], etc. However, due to the difficulty in calculating joints' torques or joints' power given whole-body movements, there is rarely research about the analysis of human movements in dynamics. Using the method described in the document, it becomes easier to gather the motion capture data of desired movements and compute the joints' dynamics properties. Thus, further exploration can be to do various dynamics analyses of the human movements, such as representing the human movements as a sequence of joint torques concerning time instead of the kinematic motion capture data, and then applying Sparse coding or Gaussian process on it.

Bibliography

- [1] Alexander, R. M. [1997], ‘A minimum energy cost hypothesis for human arm trajectories’, *Biological cybernetics* **76**(2), 97–105.
- [2] Arellano, C. J. and Kram, R. [2011], ‘The effects of step width and arm swing on energetic cost and lateral balance during running’, *Journal of biomechanics* **44**(7), 1291–1295.
- [3] Asanuma, H. [1989], *The motor cortex*, Raven Pr.
- [4] Badler, N. I., Phillips, C. B. and Webber, B. L. [1993], *Simulating humans: computer graphics animation and control*, Oxford University Press.
- [5] Bajrami, X. and Murturi, I. [2017], ‘Kinematic model of the seven link biped robot’, *IJMET*. **8**(2), 454–462.
- [6] Barbič, J., Safonova, A., Pan, J.-Y., Faloutsos, C., Hodgins, J. K. and Pollard, N. S. [2004], Segmenting motion capture data into distinct behaviors, in ‘Proceedings of Graphics Interface 2004’, Citeseer, pp. 185–194.
- [7] Bernstein, N. A. [1966], *The Co-ordination and Regulation of Movements*, Pergamon Press.

- [8] Biryukova, E., Roschin, V., Frolov, A., Ioffe, M., Massion, J. and Dufosse, M. [1999], ‘Forearm postural control during unloading: anticipatory changes in elbow stiffness’, *Experimental brain research* **124**(1), 107–117.
- [9] Bongers, R. M., Zaal, F. T. and Jeannerod, M. [2012], ‘Hand aperture patterns in prehension’, *Human movement science* **31**(3), 487–501.
- [10] Burk, D., Ingram, J. N., Franklin, D. W., Shadlen, M. N. and Wolpert, D. M. [2014], ‘Motor effort alters changes of mind in sensorimotor decision making’, *PloS one* **9**(3), e92681.
- [11] Callahan, D. M., Umberger, B. R. and Kent-Braun, J. A. [2013], ‘A computational model of torque generation: neural, contractile, metabolic and musculoskeletal components’, *PloS one* **8**(2), e56013.
- [12] Cavanagh, P. R. and Williams, K. R. [1982], ‘The effect of stride length variation on oxygen uptake during distance running.’, *Medicine and science in sports and exercise* **14**(1), 30.
- [13] Čelikovský, S. and Anderle, M. [2018], ‘Stable walking gaits for a three-link planar biped robot with two actuators based on the collocated virtual holonomic constraints and the cyclic unactuated variable’, *IFAC-PapersOnLine* **51**(22), 378–385.
- [14] Churchland, M. M., Cunningham, J. P., Kaufman, M. T., Foster, J. D., Nuyujukian, P., Ryu, S. I. and Shenoy, K. V. [2012], ‘Neural population dynamics during reaching’, *Nature* **487**(7405), 51–56.
- [15] Churchland, M. M., Cunningham, J. P., Kaufman, M. T., Ryu, S. I. and

- Shenoy, K. V. [2010], ‘Cortical preparatory activity: representation of movement or first cog in a dynamical machine?’, *Neuron* **68**(3), 387–400.
- [16] Collins, S. H., Wisse, M. and Ruina, A. [2001], ‘A three-dimensional passive-dynamic walking robot with two legs and knees’, *The International Journal of Robotics Research* **20**(7), 607–615.
- [17] Cooper, J. L. [2013], ‘Analysis and synthesis of bipedal humanoid movement: a physical simulation approach’.
- [18] Cooper, J. L. and Ballard, D. [2012], Realtime, physics-based marker following, *in* ‘International Conference on Motion in Games’, Springer, pp. 350–361.
- [19] Cotes, J. and Meade, F. [1960], ‘The energy expenditure and mechanical energy demand in walking’, *Ergonomics* **3**(2), 97–119.
- [20] Cowlagi, R. V. and Zhang, Z. [2017], ‘Route guidance for satisfying temporal logic specifications on aircraft motion’, *Journal of Guidance, Control, and Dynamics* **40**(2), 390–401.
- [21] de Grosbois, J., Heath, M. and Tremblay, L. [2015], ‘Augmented feedback influences upper limb reaching movement times but does not explain violations of fitts’ law’, *Frontiers in psychology* **6**, 800.
- [22] Delp, S. L., Anderson, F. C., Arnold, A. S., Loan, P., Habib, A., John, C. T., Guendelman, E. and Thelen, D. G. [2007], ‘Opensim: open-source software to create and analyze dynamic simulations of movement’, *IEEE transactions on biomedical engineering* **54**(11), 1940–1950.

- [23] Diedrichsen, J., Shadmehr, R. and Ivry, R. B. [2010], ‘The coordination of movement: optimal feedback control and beyond’, *Trends in cognitive sciences* **14**(1), 31–39.
- [24] Dietz, V. [2002], ‘Do human bipeds use quadrupedal coordination?’, *Trends in neurosciences* **25**(9), 462–467.
- [25] Donelan, J. M., Kram, R. and Kuo, A. D. [2002], ‘Mechanical work for step-to-step transitions is a major determinant of the metabolic cost of human walking’, *Journal of Experimental Biology* **205**(23), 3717–3727.
- [26] Erez, T., Tassa, Y. and Todorov, E. [2015], Simulation tools for model-based robotics: Comparison of bullet, havok, mujoco, ode and physx, *in* ‘2015 IEEE international conference on robotics and automation (ICRA)’, IEEE, pp. 4397–4404.
- [27] Faber, H., Van Soest, A. J. and Kistemaker, D. A. [2018], ‘Inverse dynamics of mechanical multibody systems: An improved algorithm that ensures consistency between kinematics and external forces’, *PloS one* **13**(9), e0204575.
- [28] Faure, F., Debunne, G., Cani-Gascuel, M.-P. and Multon, F. [1997], Dynamic analysis of human walking, *in* ‘Computer Animation and Simulation’97’, Springer, pp. 53–65.
- [29] Flash, T. and Henis, E. [1991], ‘Arm trajectory modifications during reaching towards visual targets’, *Journal of cognitive Neuroscience* **3**(3), 220–230.

- [30] Flash, T. and Hogan, N. [1985], ‘The coordination of arm movements: an experimentally confirmed mathematical model’, *Journal of neuroscience* **5**(7), 1688–1703.
- [31] Golovin, D., Solnik, B., Moitra, S., Kochanski, G., Karro, J. and Sculley, D. [2017], Google vizier: A service for black-box optimization, *in* ‘Proceedings of the 23rd ACM SIGKDD international conference on knowledge discovery and data mining’, pp. 1487–1495.
- [32] Graziano, M. S. and Aflalo, T. N. [2007], ‘Mapping behavioral repertoire onto the cortex’, *Neuron* **56**(2), 239–251.
- [33] Gribble, P. L., Mullin, L. I., Cothros, N. and Mattar, A. [2003], ‘Role of cocontraction in arm movement accuracy’, *Journal of neurophysiology* **89**(5), 2396–2405.
- [34] Grizzle, J. W., Chevallereau, C., Ames, A. D. and Sinnet, R. W. [2010], ‘3d bipedal robotic walking: models, feedback control, and open problems’, *IFAC Proceedings Volumes* **43**(14), 505–532.
- [35] Harper, N. G., Wilken, J. M. and Neptune, R. R. [2018], ‘Muscle function and coordination of stair ascent’, *Journal of biomechanical engineering* **140**(1), 011001.
- [36] Hogan, N. [1985], ‘The mechanics of multi-joint posture and movement control’, *Biological cybernetics* **52**(5), 315–331.
- [37] Hollerbach, J. and Atkeson, C. [1987], ‘Deducing planning variables from experimental arm trajectories: Pitfalls and possibilities’, *Biological cybernetics* **56**(5-6), 279–292.

- [38] Holt, K. G., Hamill, J. and Andres, R. O. [1991], ‘Predicting the minimal energy costs of human walking.’, *Medicine and science in sports and exercise* **23**(4), 491–498.
- [39] Hoyt, D. F. and Taylor, C. R. [1981], ‘Gait and the energetics of locomotion in horses’, *Nature* **292**(5820), 239–240.
- [40] Huang, H. J., Kram, R. and Ahmed, A. A. [2012], ‘Reduction of metabolic cost during motor learning of arm reaching dynamics’, *Journal of Neuroscience* **32**(6), 2182–2190.
- [41] Ijspeert, A. J., Crespi, A., Ryczko, D. and Cabelguen, J.-M. [2007], ‘From swimming to walking with a salamander robot driven by a spinal cord model’, *science* **315**(5817), 1416–1420.
- [42] Ingram, J. N., Körding, K. P., Howard, I. S. and Wolpert, D. M. [2008], ‘The statistics of natural hand movements’, *Experimental brain research* **188**(2), 223–236.
- [43] Jin, X., Tecuapetla, F. and Costa, R. M. [2014], ‘Basal ganglia subcircuits distinctively encode the parsing and concatenation of action sequences’, *Nature neuroscience* **17**(3), 423.
- [44] Johnson, L. and Ballard, D. [2014], Efficient codes for inverse dynamics during walking, *in* ‘Proceedings of the AAAI Conference on Artificial Intelligence’, Vol. 28.
- [45] Kalaska, J. F. [2009], From intention to action: motor cortex and the control of reaching movements, *in* ‘Progress in Motor Control’, Springer, pp. 139–178.

- [46] Kalaska, J. F., Scott, S. H., Cisek, P. and Sergio, L. E. [1997], ‘Cortical control of reaching movements’, *Current opinion in neurobiology* **7**(6), 849–859.
- [47] Khusainov, R., Shimchik, I., Afanasyev, I. and Magid, E. [2016], 3d modelling of biped robot locomotion with walking primitives approach in simulink environment, *in* ‘Informatics in Control, Automation and Robotics 12th International Conference, ICINCO 2015 Colmar, France, July 21-23, 2015 Revised Selected Papers’, Springer, pp. 287–304.
- [48] Koelewijn, A. D. and van den Bogert, A. J. [2020], ‘A solution method for predictive simulations in a stochastic environment’, *Journal of biomechanics* **104**, 109759.
- [49] Körding, K. [2007], ‘Decision theory: what” should” the nervous system do?’, *Science* **318**(5850), 606–610.
- [50] Krishchenko, A., Tkachev, S. and Fetisov, D. [2007], ‘Planar walking control for a five-link biped robot’, *Computational Mathematics and Modeling* **18**(2), 176–191.
- [51] Kubota, Y., Liu, J., Hu, D., DeCoteau, W. E., Eden, U. T., Smith, A. C. and Graybiel, A. M. [2009], ‘Stable encoding of task structure coexists with flexible coding of task events in sensorimotor striatum’, *Journal of neurophysiology* **102**(4), 2142–2160.
- [52] Kuo, A. D. and Donelan, J. M. [2010], ‘Dynamic principles of gait and their clinical implications’, *Physical therapy* **90**(2), 157–174.

- [53] Lacquaniti, F. [1989], ‘Central representations of human limb movement as revealed by studies of drawing and handwriting’, *Trends in neurosciences* **12**(8), 287–291.
- [54] Land, W. M., Rosenbaum, D. A., Seegelke, C. and Schack, T. [2013], ‘Whole-body posture planning in anticipation of a manual prehension task: Prospective and retrospective effects’, *Acta psychologica* **144**(2), 298–307.
- [55] Latash, M. L., Scholz, J. P. and Schöner, G. [2002], ‘Motor control strategies revealed in the structure of motor variability’, *Exercise and sport sciences reviews* **30**(1), 26–31.
- [56] Lee, T.-T. [1988], Trajectory planning and control of a 3-link biped robot, *in* ‘Proceedings. 1988 IEEE International Conference on Robotics and Automation’, IEEE, pp. 820–823.
- [57] Li, W. and Todorov, E. [2004], Iterative linear quadratic regulator design for nonlinear biological movement systems., *in* ‘ICINCO (1)’, pp. 222–229.
- [58] Liu, G. [2007], ‘A data-driven, piecewise linear approach to modeling human motions’.
- [59] Liu, G., Zhang, J., Wang, W. and McMillan, L. [2006], Human motion estimation from a reduced marker set, *in* ‘Proceedings of the 2006 symposium on Interactive 3D graphics and games’, pp. 35–42.
- [60] Liu, L. and Ballard, D. [2020], ‘Humans use minimum cost movements in a whole-body task’, *bioRxiv* .

- [61] Liu, L., Cooper, J. and Ballard, D. [2020], ‘Computational modeling: Human dynamic model’, *bioRxiv* .
- [62] Liu, L., Johnson, L., Zohar, O. and Ballard, D. H. [2019], ‘Humans use similar posture sequences in a whole-body tracing task’, *Iscience* **19**, 860–871.
- [63] Loeb, G. E. and Tsianos, G. A. [2015], ‘Major remaining gaps in models of sensorimotor systems’, *Frontiers in computational neuroscience* **9**, 70.
- [64] Margaria, R. [1976], *Biomechanics and energetics of muscular exercise*, Oxford University Press, USA.
- [65] Matthis, J. S., Yates, J. L. and Hayhoe, M. M. [2018], ‘Gaze and the control of foot placement when walking in natural terrain’, *Current Biology* **28**(8), 1224–1233.
- [66] Maxwell Donelan, J., Kram, R. and Arthur D, K. [2001], ‘Mechanical and metabolic determinants of the preferred step width in human walking’, *Proceedings of the Royal Society of London. Series B: Biological Sciences* **268**(1480), 1985–1992.
- [67] Melzer, I., Benjuya, N. and Kaplanski, J. [2001], ‘Age-related changes of postural control: effect of cognitive tasks’, *Gerontology* **47**(4), 189–194.
- [68] Minetti, A. E., Capelli, C., Zamparo, P., di Prampero, P. E. and Saibene, F. [1995], ‘Effects of stride frequency on mechanical power and energy expenditure of walking.’, *Medicine and Science in Sports and Exercise* **27**(8), 1194–1202.

- [69] Montepare, J. M., Goldstein, S. B. and Clausen, A. [1987], ‘The identification of emotions from gait information’, *Journal of Nonverbal Behavior* **11**(1), 33–42.
- [70] Mousavi, P. N. and Bagheri, A. [2007], ‘Mathematical simulation of a seven link biped robot on various surfaces and zmp considerations’, *Applied Mathematical Modelling* **31**(1), 18–37.
- [71] Mu, X. [2005], ‘Dynamics and motion regulation of a five-link biped robot walking in the sagittal plane’.
- [72] Mu, X. and Wu, Q. [2003], ‘Synthesis of a complete sagittal gait cycle for a five-link biped robot’, *Robotica* **21**(5), 581–587.
- [73] Mu, X. and Wu, Q. [2004], Sagittal gait synthesis for a five-link biped robot, *in* ‘Proceedings of the 2004 American Control Conference’, Vol. 5, IEEE, pp. 4004–4009.
- [74] Mullick, A. A., Turpin, N. A., Hsu, S.-C., Subramanian, S. K., Feldman, A. G. and Levin, M. F. [2018], ‘Referent control of the orientation of posture and movement in the gravitational field’, *Experimental brain research* **236**(2), 381–398.
- [75] Multon, F., France, L., Cani-Gascuel, M.-P. and Debunne, G. [1999], ‘Computer animation of human walking: a survey’, *The journal of visualization and computer animation* **10**(1), 39–54.
- [76] Nagai, K., Yamada, M., Mori, S., Tanaka, B., Uemura, K., Aoyama, T., Ichihashi, N. and Tsuboyama, T. [2013], ‘Effect of the muscle coactivation

- tion during quiet standing on dynamic postural control in older adults', *Archives of gerontology and geriatrics* **56**(1), 129–133.
- [77] Nagai, K., Yamada, M., Uemura, K., Yamada, Y., Ichihashi, N. and Tsuboyama, T. [2011], 'Differences in muscle coactivation during postural control between healthy older and young adults', *Archives of gerontology and geriatrics* **53**(3), 338–343.
- [78] Nelson, W. L. [1983], 'Physical principles for economies of skilled movements', *Biological cybernetics* **46**(2), 135–147.
- [79] Ortega, J. D., Fehlmann, L. A. and Farley, C. T. [2008], 'Effects of aging and arm swing on the metabolic cost of stability in human walking', *Journal of biomechanics* **41**(16), 3303–3308.
- [80] Patel, H., O'Neill, G. and Artemiadis, P. [2014], 'On the effect of muscular cocontraction on the 3-d human arm impedance', *IEEE Transactions on Biomedical Engineering* **61**(10), 2602–2608.
- [81] Ralston, H. J. [1958], 'Energy-speed relation and optimal speed during level walking', *Internationale Zeitschrift für Angewandte Physiologie Einschliesslich Arbeitsphysiologie* **17**(4), 277–283.
- [82] Remy, C. D. and Thelen, D. G. [2009], 'Optimal estimation of dynamically consistent kinematics and kinetics for forward dynamic simulation of gait', *Journal of biomechanical engineering* **131**(3).
- [83] Roether, C. L., Omlor, L., Christensen, A. and Giese, M. A. [2009], 'Critical features for the perception of emotion from gait', *Journal of vision* **9**(6), 15–15.

- [84] Rosenbaum, D. A., Brach, M. and Semenov, A. [2011], ‘Behavioral ecology meets motor behavior: Choosing between walking and reaching paths’, *Journal of Motor Behavior* **43**(2), 131–136.
- [85] Rosenbaum, D. A., Loukopoulos, L. D., Meulenbroek, R. G., Vaughan, J. and Engelbrecht, S. E. [1995], ‘Planning reaches by evaluating stored postures.’, *Psychological review* **102**(1), 28.
- [86] Said, H. E., Tan, T. N. and Baker, K. D. [2000], ‘Personal identification based on handwriting’, *Pattern Recognition* **33**(1), 149–160.
- [87] Sánchez, N., Park, S. and Finley, J. M. [2017], ‘Evidence of energetic optimization during adaptation differs for metabolic, mechanical, and perceptual estimates of energetic cost’, *Scientific Reports* **7**(1), 1–14.
- [88] Schmitz, A., Silder, A., Heiderscheit, B., Mahoney, J. and Thelen, D. G. [2009], ‘Differences in lower-extremity muscular activation during walking between healthy older and young adults’, *Journal of electromyography and kinesiology* **19**(6), 1085–1091.
- [89] Schulman, J., Ho, J., Lee, C. and Abbeel, P. [2016], Learning from demonstrations through the use of non-rigid registration, *in* ‘Robotics Research’, Springer, pp. 339–354.
- [90] Selinger, J. C., O’Connor, S. M., Wong, J. D. and Donelan, J. M. [2015], ‘Humans can continuously optimize energetic cost during walking’, *Current Biology* **25**(18), 2452–2456.
- [91] Sentis, L., Park, J. and Khatib, O. [2010], ‘Compliant control of multi-

- contact and center-of-mass behaviors in humanoid robots’, *IEEE Transactions on robotics* **26**(3), 483–501.
- [92] Shenoy, K. V., Sahani, M. and Churchland, M. M. [2013], ‘Cortical control of arm movements: a dynamical systems perspective’, *Annual review of neuroscience* **36**.
- [93] Silverman, A. K., Neptune, R. R., Sinitski, E. H. and Wilken, J. M. [2014], ‘Whole-body angular momentum during stair ascent and descent’, *Gait & posture* **39**(4), 1109–1114.
- [94] Smeets, J. B., Martin, J. and Brenner, E. [2010], ‘Similarities between digits’ movements in grasping, touching and pushing’, *Experimental brain research* **203**(2), 339–346.
- [95] Srihari, S. N., Cha, S.-H., Arora, H. and Lee, S. [2002], ‘Individuality of handwriting’, *Journal of forensic science* **47**(4), 1–17.
- [96] Ting, L. H. [2007], ‘Dimensional reduction in sensorimotor systems: a framework for understanding muscle coordination of posture’, *Progress in brain research* **165**, 299–321.
- [97] Ting, L. H. and Macpherson, J. M. [2005], ‘A limited set of muscle synergies for force control during a postural task’, *Journal of neurophysiology* **93**(1), 609–613.
- [98] Tipping, M. E. and Bishop, C. M. [1999], ‘Probabilistic principal component analysis’, *Journal of the Royal Statistical Society: Series B (Statistical Methodology)* **61**(3), 611–622.

- [99] Todorov, E. [2004], ‘Optimality principles in sensorimotor control’, *Nature neuroscience* **7**(9), 907–915.
- [100] Troje, N. F. [2002], ‘Decomposing biological motion: A framework for analysis and synthesis of human gait patterns’, *Journal of vision* **2**(5), 2–2.
- [101] Umberger, B. R. and Martin, P. E. [2007], ‘Mechanical power and efficiency of level walking with different stride rates’, *Journal of Experimental Biology* **210**(18), 3255–3265.
- [102] van Beers, R. J., Brenner, E. and Smeets, J. B. [2012], ‘Random walk of motor planning in task-irrelevant dimensions’, *Journal of neurophysiology* **109**(4), 969–977.
- [103] van der Kooij, H., van Asseldonk, E. and van der Helm, F. C. [2005], ‘Comparison of different methods to identify and quantify balance control’, *Journal of neuroscience methods* **145**(1-2), 175–203.
- [104] Van Dokkum, L. E., Mottet, D., Laffont, I., Bonafé, A., de Champfleur, N. M., Froger, J. and Le Bars, E. [2017], ‘Kinematics in the brain: unmasking motor control strategies?’, *Experimental brain research* **235**(9), 2639–2651.
- [105] Vollmer, C., Hellbach, S., Eggert, J. and Gross, H.-M. [2014], ‘Sparse coding of human motion trajectories with non-negative matrix factorization’, *Neurocomputing* **124**, 22–32.
- [106] Wang, J. [2020], ‘An intuitive tutorial to gaussian processes regression’, *arXiv preprint arXiv:2009.10862*.

- [107] Wang, J. M., Fleet, D. J. and Hertzmann, A. [2007], ‘Gaussian process dynamical models for human motion’, *IEEE transactions on pattern analysis and machine intelligence* **30**(2), 283–298.
- [108] Welch, T. D. and Ting, L. H. [2014], ‘Mechanisms of motor adaptation in reactive balance control’, *PloS one* **9**(5), e96440.
- [109] Williams, C. K. and Rasmussen, C. E. [1996], ‘Gaussian processes for regression’.
- [110] Wolpert, D. M. [1997], ‘Computational approaches to motor control’, *Trends in cognitive sciences* **1**(6), 209–216.
- [111] Wolpert, D. M. and Ghahramani, Z. [2000], ‘Computational principles of movement neuroscience’, *Nature neuroscience* **3**(11s), 1212.
- [112] Wolpert, D. M. and Landy, M. S. [2012], ‘Motor control is decision-making’, *Current opinion in neurobiology* **22**(6), 996–1003.
- [113] Wong, J. D., Selinger, J. C. and Donelan, J. M. [2019], ‘Is natural variability in gait sufficient to initiate spontaneous energy optimization in human walking?’, *Journal of neurophysiology* **121**(5), 1848–1855.
- [114] Zarrugh, M. and Radcliffe, C. [1978], ‘Predicting metabolic cost of level walking’, *European Journal of Applied Physiology and Occupational Physiology* **38**(3), 215–223.
- [115] Zarrugh, M., Todd, F. and Ralston, H. [1974], ‘Optimization of energy expenditure during level walking’, *European journal of applied physiology and occupational physiology* **33**(4), 293–306.

- [116] Zordan, V. B. and Hodgins, J. K. [2002], Motion capture-driven simulations that hit and react, *in* ‘Proceedings of the 2002 ACM SIGGRAPH/Eurographics symposium on Computer animation’, pp. 89–96.